Extreme Rainfall Intensities and Long-term Rainfall Risk from Tropical Cyclones

by

Andreas Langousis

M.Sc. in Civil and Environmental Engineering (2005)
Massachusetts Institute of Technology

Diploma of Civil Engineering (2003)
National Technical University of Athens.

Submitted to the Department of Civil and Environmental Engineering
in partial fulfillment of the requirements for the degree of

DOCTOR OF SCIENCE IN THE FIELD OF CIVIL AND ENVIRONMENTAL

ENGINEERING

at the

MASSACHUSETTS INSTITUTE OF TECHNOLOGY

February 2009

Signature of Author...
Department of Civil and Environmental Engineering
December 16, 2008

Certified by...
Daniele Veneziano
Professor of Civil and Environmental Engineering
Thesis Supervisor

Accepted by...
Daniele Veneziano
Chairman, Departmental Committee for Graduate Students

Extreme Rainfall Intensities and Long-term Rainfall Risk from Tropical Cyclones

by

Andreas Langousis

Submitted to the Department of Civil and Environmental Engineering
on December 16, 2008 in partial fulfillment of the requirements
for the Degree of Doctor of Science in the Field of Civil and Environmental Engineering.

Abstract

We develop a methodology for the frequency of extreme rainfall intensities caused by tropical cyclones (TCs) in coastal areas. The mean rainfall field associated with a TC with maximum tangential wind speed V_{max}, radius of maximum winds R_{max}, and translation speed V_t is obtained using a physically-based model, whereas rainfall variability at both large scales (from storm to storm) and small scales (due to rainbands and local convection) is modeled statistically.

The statistical component is estimated using precipitation radar (PR) data from the TRMM mission. Taylor's hypothesis is used to convert spatial rainfall intensity fluctuations to temporal fluctuations at a given location A. The combined physical-statistical model gives the distribution of the maximum rainfall intensity at A during a period of duration D for a TC with characteristics (V_{max}, R_{max}, V_t) that passes at a given distance from A.

To illustrate the use of the model for long-term rainfall risk analysis, we formulate a recurrence model for tropical cyclones in the Gulf of Mexico that make landfall between longitudes 85^o-95^oW. We then use the rainfall and recurrence models to assess the rainfall risk for New Orleans. For return periods of 100 years or more and long averaging durations (D around 12-24 hours), tropical cyclones dominate over other rainfall event types, whereas the reverse is true for shorter return periods or shorter averaging durations.

Thesis Supervisor: Daniele Veneziano
Title: Professor of Civil and Environmental Engineering

…to my family.

Acknowledgments

Reaching the end effort, I would like to acknowledge all those who contributed and provided the basis for this work.

First of all I would like to thank my professor and friend Daniele Veneziano for mentoring me in the area of stochastic modeling and providing continuous support during my studies at MIT. Daniele Veneziano is not only an outstanding professor and researcher; he is also an excellent mentor and a most understanding and helpful person. If it wasn't for him, I doubt this effort would have been possible.

By no means can I forget the help and support of two other members of my doctoral committee: Professor Elfatih Eltahir contributed many comments and fruitful discussions making my doctoral degree an educative and constructive experience. Thanks are also due to Professor Jim Hansen from the Naval Research Laboratory, who taught me the basis of geophysical fluid dynamics, introduced me to the field of atmospheric sciences and provided me with numerous suggestions and helpful advice.

I also owe a big "thanks" to the administrative staff of MIT and especially to Pat Dixon, Kris Kipp, Jeanette Marchocki, Patricia Glidden, Donna Beaudry, Donna Hudson, Cynthia Stewart and Andre Dixon.

I cannot omit to acknowledge some persons from the National Technical University of Athens (NTUA) that truly marked my life by providing me the basis in hydrology and engineering: Costantinos Moutzouris, President of the National Technical University of Athens; Maria Mimikou, Director of the Laboratory of Hydrology and Water Resources Management; George Christodoulou, Professor of Applied Hydraulics; Demetris Koutsoyiannis, Professor of Hydrology and Analysis of Water Systems; Andreas Andreadakis, Director of the Laboratory of Sanitary Engineering; Costantinos Memos, Professor of Maritime Hydraulics; Charis Gantes, Associate Professor in the Metal Structures Laboratory; and the hydraulic engineers Jack Gabrielidis and Tilemahos Papathanasiadis are the persons that I thank the most for becoming a Civil Engineer.

Special thanks are due to my former supervisor, professor and friend Demetris Koutsoyiannis, who introduced me to the world of hydrologic stochastics. If it wasn't for him, this magic journey wouldn't have ever started.

I am also grateful to my numerous friends from Greece and MIT for standing by me and giving me courage to pursue this long-lasting effort. Each of them holds a particular place in my heart.

Finally, words are not enough to describe my gratitude to my father, my mother, my brother and Helen for supporting all my decisions and efforts. They have always been the motivation for anything I accomplish in life. This thesis is dedicated to them.

Cambridge, December 2008

Andreas Langousis

Special Acknowledgments: This work was supported by the Alexander S. Onassis Public Benefit Foundation under Scholarship No. F-ZA 054/2005-2006. The administrative assistance of Mrs. Evgenia Pavlopoulou with the scholarship is greatly acknowledged. The author is grateful to Melicie Desflots for the MM5 simulations, Shuyi Chen for the PR-TRMM rainfall products, Robert Rogers and Jason Dunion for making available a code for Shapiro's (1983) model, Robert Rogers for providing parametric expressions for the shear-induced rainfall asymmetries, and Mark DeMaria for access to the extended best track record.

Table of contents

Introduction

In this thesis we develop a framework to estimate extreme rainfalls from tropical cyclones at coastal sites. Interest is in the distribution of $I_{D,max}$: the maximum rainfall intensity at a site A over a period D during the passage of a storm.

The distribution of rainfall extremes like $I_{D,max}$ is usually displayed in the form of intensity-duration-frequency (IDF) curves; see e.g. Chow *et al.* (1988) and Singh (1992). These are plots of the rainfall intensity i as a function of the average duration D for different return period values T, where T is defined as the reciprocal of the exceedance rate $\lambda_{I_{D,max}>i} = \lambda P[I_{D,max} > i]$. λ is the annual rate at which TCs "hit" site A.

Knowledge of the distribution of $I_{D,max}$ is important when one assesses flood risk in TC-prone areas as the combination of rainfall, surges and waves (Herbert *et al.*, 1997; Rappaport, 2000). In addition, interesting insight can be produced when comparing theoretical IDF curves for TC rainfall at a site to empirically obtained IDF values for all rainstorms included (TCs and non-TCs). For example, one can conclude on the range of durations D and return periods T for which TCs dominate over other rainfall event types.

The episodic and spatially localized nature of TCs make the distribution of $I_{D,max}$ hard to obtain using standard methods of probabilistic assessment of extreme rainfalls. These include fitting a probability distribution directly to the historical annual maxima observed at the site (e.g. Koutsoyiannis *et al.*, 1998 for a review) or derive the maximum distribution from peak-over-threshold (PoT) information (e.g. Madsen *et al.*, 1997). For example, both annual maximum TC rainfalls and annual PoT statistics at a site depend on whether in any given year the site was "hit" by one or more TCs and therefore are highly erratic.

In this case, the assessment of risk is best done parametrically, using the effects of events with various characteristics and the frequency with which those events occur. For tropical cyclones, the storm characteristics of interest include the intensity, size, location, translation speed and direction at landfall, and possibly other parameters. We list these relevant parameters as components of a vector $\boldsymbol{\theta}$. This parametric approach has been used with tropical cyclones in the context of wind, surge and waves (Myers, 1975; Ho and Myers, 1975; Ho *et al.*, 1987; Powell *et al.*, 2005; IPET, 2006, 2008), but not rain. The objective of this thesis is to fill this gap.

The main problem in a parametric assessment of TC rainfall risk is the evaluation of the extreme rainfalls caused by a TC with given characteristics $\boldsymbol{\theta}$: i.e. the data on TC rainfall are sparse and the potentially important TC parameters too many to directly infer a parametric rainfall model from empirical observations. For example, current parametric approaches (Lonfat *et al.*, 2004, 2007; Tuleya *et al.*, 2007) classify storms into three coarse categories of hurricane intensity, use microwave imager (TMI) data from TRMM (Simpson *et al.* 1988) to calculate the ensemble-average rainrate for each category as a function of distance from the TC center, and interpolate from these results to calculate the 24-hr average rainfall accumulation from the passage of a TC. Limitations of these approaches are: 1) the coarse and incomplete storm parameterization: the size of the vortex R_{max} is only implicitly taken into account through its dependence on V_{max}, while other factors (e.g. the radial wind velocity profile in the main vortex, the surface roughness, and the storm translation velocity) are ignored and 2) the fact that they do not account for rainfall intensifications due to rainbands and local convection.

A more complete approach is to combine physical modeling with data analysis. Here, we use a relatively simple physical model to capture the main effects of $\boldsymbol{\theta}$ on rainfall, and statistical data analysis to assess the storm-to-storm fluctuations due to features like rainbands and convective cells that the physical model does not resolve.

The thesis is organized into three main chapters. Chapter 1 describes a theoretical method to estimate the large-scale horizontal and vertical winds inside TCs (the vertical winds are largely responsible for rain). The model is an extension of Smith's (1968) formulation and is referred to here as the Modified Smith (MS) model. Characteristics of the TC that are explicitly considered by the MS model are the maximum tangential wind speed V_{max}, the radius of maximum winds R_{max}, the parameter B that controls the shape of the radial profile of the tangential wind speed (Holland, 1980), the storm translation velocity V_t, the surface drag coefficient C_D and the vertical diffusion coefficient K. The MS model does not resolve rainbands, local convection and turbulent phenomena and therefore produces smooth wind fields.

Chapter 2 extends the MS model to predict TC rain. This is done under the assumption that water vapor condensation in the main vortex converts all the upward moisture flux at the top of the TC boundary layer to rainfall. The vertical moisture flux itself is evaluated from the vertical winds generated by the MS model and two additional parameters: the average temperature $\bar{T}$ and the average saturation ratio $\bar{Q}$ inside the TC boundary layer. The calculated rainfall field is not simply proportional to the vertical winds at the top of the boundary layer produced by the MS model. This is because (1) the trajectory of moisted air parcels has an outward slant depending on distance from the TC center and (2) the ascending air parcels and descending rain drops are advected into a helical motion by the cyclonic circulation; therefore a parcel of air that leaves the TC boundary layer contributes rainfall to a range of azimuthal locations. We call this the modified-Smith-for-rainfall (MSR) model. The MSR model should prove useful for climatologic studies, but for hazard analysis it has the major limitation of ignoring the small-scale rainfall fluctuations associated with rainbands and local convection.

Chapter 3 adds a stochastic fluctuation component to the MSR predictions to determine the probability distribution of the maximum rainfall intensity at a site A during a period of duration D, $I_{D,max}(y,\boldsymbol{\theta})$, for a TC with characteristics $\boldsymbol{\theta}$ whose center passes at distance y from A. The statistical component is fitted and validated using precipitation radar (PR) data from the TRMM mission. Also, Taylor's hypothesis is used to convert spatial rainfall intensity fluctuations to temporal fluctuations at A. To illustrate the use of the model for long-term rainfall risk analysis, we formulate a recurrence model for tropical cyclones in the Gulf of Mexico. We then use the rainfall and recurrence models to assess the rainfall risk for New Orleans.

Chapters 1, 2 and 3 are written in a stand-alone format and are very similar to published (Langousis *et al.*, 2008; Langousis and Veneziano, 2008) or submitted (Langousis and Veneziano, 2009) papers.

Conclusions and possible future research directions are given in Chapter 4. Supplemental material for the theoretical model in Chapter 1 and alternative methodologies for evaluating the statistical component for the rainfall fluctuations in Chapter 3 are presented in Appendices A and B, respectively.

1. Boundary Layer Model for Moving Tropical Cyclones

1.1 Introduction

Tropical cyclones (TCs) are a particular class of rotating low-pressure systems that develop over tropical and subtropical waters. The systems have a warm-core, a well-organized convection, and cyclonic surface wind circulation (Anthes, 1982; Landsea, 2000).

Empirical observations (La Seur and Hawkins, 1963; Hawkins and Rubsam, 1968; Holland, 1980; Willoughby, 1990, 1991; Vickery *et al.*, 2000; among others) show that in the altitude range from 2-3km to about 10km, the tangential winds are in approximate gradient balance and the radial inflow is negligible. Based on earlier work by Schloemer (1954) and Myers (1957), Holland (1980) used a symmetric pressure distribution to derive the tangential gradient wind V_{gr}, as a function of distance R from the TC center. His result, which we refer to here as Holland's wind profile, is

$$V_{gr}(R) = V_{max} \sqrt{(R_{max}/R)^{B} \exp[1-(R_{max}/R)^{B}]} \tag{1.1}$$

where V_{max}, R_{max}, and B are TC-specific constants. The tangential velocity V_{gr} increases with R to a maximum V_{max} at $R = R_{max}$ (usually referred to as the radius of maximum winds). For $R >> R_{max}$, V_{gr} has an approximately power-law decay with distance, with exponent $-B/2$. According to Willoughby and Rahn (2004), B varies in the range [1, 2] with typical values around 1.4.

Inside the TC boundary layer (BL) (within approximately 1-2km from the surface), frictional stresses are important and result in an inward net force that drives low-level convergence. Consequently, the horizontal and vertical wind fields are strongly coupled and equation (1.1) does not apply. Horizontal convergence drives the vertical winds, which are maximum at the top of the boundary layer near the radius of maximum winds R_{max} (e.g. Kepert, 2001 and Kepert and Wang, 2001).

Since the convergence of moisture inside the BL is of major importance for the maintenance, evolution and destructive potential of TCs (Emanuel, 1986, 1989; Renno and Ingersoll, 1996), a number of studies (Myers and Malkin, 1961; Chow, 1971; Shapiro, 1983; Kepert, 2001) have focused on developing theoretical models for the boundary layer of moving TCs. These models derive the radial and tangential winds inside the boundary layer from an assumed radial profile of the tangential wind velocity under gradient balance, for example the profile in equation (1.1), and from suitable surface boundary conditions.

Section 1.2 reviews these BL models and their limitations. Section 1.3 describes our proposed model by giving the governing equations (an extension of the equations of Smith, 1968) and discussing their numerical solution. In Section 1.4, we compare model results with earlier models and with simulations using the Fifth-Generation Pennsylvania State University/NCAR Mesoscale Model (MM5). Section 1.5 shows how the calculated winds depend on various storm parameters. Conclusions are stated in Section 1.6.

1.2 Review of Boundary Layer Models

The focus of this review is on BL models for moving tropical cyclones, but studies of stationary TCs that are relevant to what follows are also mentioned.

Boundary layer models differ mainly in their treatment of altitude Z and the surface boundary conditions. In one of the earlier studies of moving TCs, Myers and Malkin (1961) used a Lagrangian parcel trajectory approach to study the horizontal winds inside the BL. The authors assume that the frictional drag force is proportional to the square of the wind speed with equal tangential and radial components. Another (implicit) assumption is that the velocity of the background flow is zero rather than equal to the translation velocity of the TC. A finding of the study is that, when a TC in the northern (southern) hemisphere moves, the radial convergence is maximum at the right-front (left-front) quadrant of the vortex and the location of this maximum rotates anticyclonically as the translation velocity V_t increases.

Based on the work of Chow (1971), Shapiro (1983) approximated the boundary layer of a moving TC by a slab of constant depth H =1km. The horizontal momentum equations are formulated in cylindrical coordinates that translate with the vortex and then averaged in the vertical direction. This results in a system of two partial differential equations (PDEs) that are solved numerically for the vertically averaged tangential $\bar{V}(R,\theta)$ and radial $\bar{U}(R,\theta)$ wind velocity as a function of radius R and the azimuth θ relative to the direction of TC motion. Contrary to Myers and Malkin (1961), Shapiro's (1983) formulation assumes that the frictional drag force is parallel to the surface-relative flow and its magnitude is proportional to the square of the composite surface-relative wind velocity. Although the two studies use different formulations for the friction-induced convergence, they both produce maximum convergence at the right-front quadrant of vortices in the northern hemisphere. However, in Shapiro's model the location of the maximum does not depend on the translation velocity, whereas in Myers and Malkin's (1961) analysis it does.

The main limitation of Shapiro's (1983) approach is that it approximates the BL as a slab of constant depth and hence cannot resolve the variation of U and V with height. According to Anthes (1971), this leads to overestimation of the radial and vertical velocities close to the vortex core; see discussion of Figure 1.3 below. Another limitation of Shapiro's analysis is that the numerical stability of the system depends on TC parameters such as the depth of the boundary layer H, the translation velocity V_t, the vertical diffusion coefficient K and the surface drag coefficient C_D. This limitation becomes important when, as for example in risk studies, one needs to calculate the wind field under a wide variety of conditions.

A third BL model for moving tropical cyclones was proposed by Kepert (2001) (see also refinements in Kepert, 2006b). Kepert's formulation neglects vertical advection and linearizes the horizontal advection. This produces a system of linear PDEs that is solved analytically for the radial, tangential and vertical wind velocities (U, V and W, respectively) as a function of R, θ, and Z. Kepert (2001) uses a bulk formulation of the surface stresses similar to those of Rosenthal (1962), Shapiro (1983) and Smith (1968, 2003). However, the surface boundary condition is linearized to allow analytical integration. Linearization produces inaccurate results close to the TC center ($R < 2\text{-}3R_{max}$) where the horizontal gradient of the wind components is high, when the vertical gradient of the horizontal wind velocity is large (this happens for large surface drag coefficient C_D; see discussion on Figure 1.2 below), for high translation velocities ($V_t > 5$m/s), and under inertially neutral conditions ($B > 1.6\text{-}1.8$). Other linearizations of the horizontal momentum equations have been proposed by Haurwitz (1935), Rosenthal (1962), Miller (1965) and Elliassen and Lystad (1977), but these formulations are for stationary vortices ($V_t = 0$).

An order of magnitude analysis by Smith (1968) shows that in the near-core region the nonlinear terms are as important as the linear ones. To include the non-linear terms, Smith (1968) (see also refinements in Leslie and Smith, 1970 and Bode and Smith, 1975) used the Karman and Pohlhausen momentum integral method to calculate the radial $U(R,Z)$ and tangential $V(R,Z)$ wind velocities in a stationary vortex. In the momentum integral method (Schlichting, 1960), one avoids an explicit analysis of altitude Z by assuming vertical profiles for U and V that satisfy the boundary conditions at the surface ($Z = 0$), and tend asymptotically to gradient balance as $Z \to \infty$; see equation (1.3) below. Specifically, Smith (1968) used profiles of the Ekman type, with an amplitude coefficient E and a dimensionless BL scale thickness δ as parameters. The horizontal momentum equations are vertically integrated to produce a system of ordinary differential equations that are solved numerically to obtain E and δ as a function of R.

The main limitation of Smith's (1968) model is that it does not consider storm motion. Also, Smith's (1968) formulation is theoretically correct only for the case of no slip at the surface boundary (i.e. for $C_D \to \infty$); see Section 1.3. In the following section, we extend Smith's (1968) model to include storm motion and correct the formulation for the general case of stress surface boundary conditions.

1.3 Proposed Model

In a cylindrical coordinate system (R, θ, Z) that follows the vortex motion, the boundary layer equations are (see Smith,1968 and Kepert 2001 for a detailed derivation),

$$\begin{aligned}
&U\frac{\partial U}{\partial R}+\frac{V}{R}\frac{\partial U}{\partial \theta}+W\frac{\partial U}{\partial Z}+\frac{V_{gr}^{2}-V^{2}}{R}+f(V_{gr}-V)=K\frac{\partial^{2}U}{\partial Z^{2}} \quad &\text{(a)}\\
&U\frac{\partial V}{\partial R}+\frac{V}{R}\frac{\partial V}{\partial \theta}+W\frac{\partial V}{\partial Z}+\frac{UV}{R}+fU=K\frac{\partial^{2}V}{\partial Z^{2}} \quad &\text{(b)}\\
&\frac{\partial (RU)}{\partial R}+\frac{\partial V}{\partial \theta}+\frac{\partial (RW)}{\partial Z}=0 \quad &\text{(c)}
\end{aligned} \qquad (1.2)$$

where R is distance from the vortex center, θ is azimuth relative to the direction of motion, f is the Coriolis parameter, U, V, and W are the storm-relative radial, tangential and vertical wind velocities, respectively, K is the vertical diffusion coefficient of the horizontal momentum, and V_{gr} is the tangential wind velocity under gradient wind balance; see for example equation (1.1).

As Kepert (2001) and Smith (1968), we solve equations (1.2) for the case of a semi-infinite domain, when gradient wind balance is satisfied asymptotically as $Z \to \infty$,

$$\frac{\partial U}{\partial Z}=\frac{\partial V}{\partial Z}=U=0, \text{ and } V=V_{gr}, \text{ at } Z \to \infty \qquad (1.3)$$

The translation velocity V_t enters through the surface boundary conditions. Suppose that the vortex is translating in the positive x-direction with constant speed V_t. Using a viscous surface stress formulation similar to Smith (1968, 2003) and Kepert (2001), the conditions to be satisfied at the surface boundary ($Z = 0$) are:

$$\begin{aligned} &U+V_t\cos\theta = \frac{K}{C_D V_{gr}}\frac{\partial U}{\partial Z} && \text{(a)} \\ &V\text{-}V_t\sin\theta = \frac{K}{C_D V_{gr}}\frac{\partial V}{\partial Z} && \text{(b)} \\ &W = 0 && \text{(c)} \end{aligned} \qquad (1.4)$$

where C_D is a surface drag coefficient; see for example Rosenthal (1962), Smith (1968, 2003), Kepert (2001), and Kepert and Wang (2001). For $1/C_D = 0$, equation (1.4) corresponds to no slip conditions ($U = -V_t\cos\theta$, $V = V_t\sin\theta$) at the surface boundary.

For $R \to \infty$, the system in equation (1.2) reduces to the classic Ekman BL equations under geostrophic conditions (Kundu and Cohen, 2004):

$$\begin{aligned} &f(V_{gr}\text{-}V) = K\frac{\partial^2 U}{\partial Z^2} && \text{(a)} \\ &fU = K\frac{\partial^2 V}{\partial Z^2} && \text{(b)} \\ &W = \text{const.} && \text{(c)} \end{aligned} \qquad (1.5)$$

Denote by R_g the distance from the TC center beyond which the geostrophic model in equation (1.5) is approximately valid; say $R_g \approx 1000$km (Smith, 1968; Kundu and Cohen, 2004). Also denote by K_M the vertical diffusion coefficient under geostrophic conditions and let $V_g = V_{gr}(R_g)$ be the gradient tangential wind for $R = R_g$ and $Z_g = (K_M/f)^{1/2}$ (Z_g has the meaning of vertical length scale for the depth of the boundary layer; see below). Then one can write equation (1.2) in dimensionless form, as

$$\begin{aligned} &R_o\left[u\frac{\partial u}{\partial r} + \frac{v}{r}\frac{\partial u}{\partial \theta} + w\frac{\partial u}{\partial z} + \frac{{v_{gr}}^2\text{-}v^2}{r}\right] + v_{gr}\text{-}v = k\frac{\partial^2 u}{\partial z^2} && \text{(a)} \\ &R_o\left[u\frac{\partial v}{\partial r} + \frac{v}{r}\frac{\partial v}{\partial \theta} + w\frac{\partial v}{\partial z} + \frac{uv}{r}\right] + u = k\frac{\partial^2 v}{\partial z^2} && \text{(b)} \\ &\frac{\partial (ru)}{\partial r} + \frac{\partial v}{\partial \theta} + \frac{\partial (rw)}{\partial z} = 0 && \text{(c)} \end{aligned} \qquad (1.6)$$

and equations (1.3) and (1.4) become

$$\begin{aligned} &\frac{\partial u}{\partial z} = \frac{\partial v}{\partial z} = u = 0, \text{ and } v = v_{gr}, \text{ at } z \to \infty && \text{(a)} \\ &u+v_t\cos\theta = \frac{\alpha k}{v_{gr}}\frac{\partial u}{\partial z}, \; v\text{-}v_t\sin\theta = \frac{\alpha k}{v_{gr}}\frac{\partial v}{\partial z}, \text{ and } w = 0, \text{ at } z = 0 && \text{(b)} \end{aligned} \qquad (1.7)$$

In equations (1.6) and (1.7), $R_o = V_g/(R_g f)$ is the Rossby number and $r = R/R_g$, $z = Z/Z_g$, $v_t = V_t/V_g$, $u = U/V_g$, $v = V/V_g$, $w = (WR_g)/(V_g Z_g)$, $v_{gr} = V_{gr}/V_g$, $k = K/K_M$, and $\alpha = K_M/(C_D Z_g V_g)$ are dimensionless quantities. In his model for axi-symmetric vortices, Smith (1968) allows K to be different from K_M and to vary radially. In the present extension to moving vortices, we further allow K to vary azimuthally.

Vertical integration of equation (1.6) under boundary conditions (1.7.a) gives

$$R_o\left[\frac{\partial}{\partial r}\int_0^\infty ru^2\,dz + \frac{\partial}{\partial\theta}\int_0^\infty uv\,dz + \int_0^\infty v_{gr}{}^2 - v^2\,dz\right] + r\int_0^\infty v_{gr} - v\,dz = -kr\left.\frac{\partial u}{\partial z}\right|_{z=0} \quad \text{(a)}$$

$$R_o\left[\frac{\partial}{\partial r}\int_0^\infty r^2uv\,dz + r\frac{\partial}{\partial\theta}\int_0^\infty v^2\,dz + r^2 w_\infty v_{gr}\right] + r^2\int_0^\infty u\,dz = -kr^2\left.\frac{\partial v}{\partial z}\right|_{z=0} \quad \text{(b)} \qquad (1.8)$$

$$w_\infty = -\frac{1}{r}\left[\frac{\partial}{\partial r}\left(r\int_0^\infty u\,dz\right) + \int_0^\infty \frac{\partial v}{\partial\theta}\,dz\right] \quad \text{(c)}$$

where w_∞ is the dimensionless vertical wind velocity at $Z \to \infty$. Next we discuss how equation (1.8) is solved under the conditions (1.7.b).

1.3.1 Momentum integral method

Similar to Smith (1968) we take the boundary layer thickness to be proportional to $Z_g = (K_M/f)^{1/2}$, with proportionality coefficient δ. In Smith's (1968) axi-symmetric formulation δ exhibits only radial variation, but in the present case of moving cyclones we allow δ to vary also azimuthally.

Define $\eta = Z/[Z_g\,\delta(r,\theta)] = z/\delta(r,\theta)$ and notice that the geostrophic model in equation (1.5) is satisfied for $\delta = \sqrt{2}$; see e.g. Kundu and Cohen (2004). Following the derivations of Schlichting (1960), Mack (1962) and Smith (1968), but allowing azimuthal dependence of u and v, the solution of equation (1.8) can be approximated as

$$u(r,\theta,\eta) = E(r,\theta)\,\Psi(r,\theta,\eta) \quad \text{(a)}$$
$$v(r,\theta,\eta) = \Omega(r,\theta,\eta) \quad \text{(b)} \qquad (1.9)$$

where $E(r,\theta)$ is an unknown function, usually referred to as the amplitude coefficient, and Ψ and Ω are such that $(u,v) = (\Psi,\Omega)$ satisfy equations (1.6) and (1.7) under geostrophic conditions $(R > R_g)$. After some algebra one obtains

$$\begin{aligned} \Psi(r,\theta,\eta) &= g(r,\theta,\eta)\, v_t \cos\theta + f(r,\theta,\eta)\, (v_{gr} - v_t \sin\theta) - v_t \cos\theta && \text{(a)} \\ \Omega(r,\theta,\eta) &= g(r,\theta,\eta)\, (v_{gr} - v_t \sin\theta) - f(r,\theta,\eta)\, v_t \cos\theta + v_t \sin\theta && \text{(b)} \end{aligned} \qquad (1.10)$$

where

$$\begin{aligned} f(r,\theta,\eta) &= -e^{-\eta}\, [a_1(r,\theta) \sin\eta + a_2(r,\theta) \cos\eta] && \text{(a)} \\ g(r,\theta,\eta) &= 1 - e^{-\eta}\, [a_1(r,\theta) \cos\eta + a_2(r,\theta) \sin\eta] && \text{(b)} \end{aligned} \qquad (1.11)$$

The parameters $a_1(r,\theta)$ and $a_2(r,\theta)$ in equation (1.11) are calculated so that (u,v) in equation (1.9) satisfy condition (1.7.b). This gives

$$a_2(r,\theta) = \frac{L_3 L_4 - L_1 L_6}{L_2 L_4 - L_1 L_5}, \quad a_1(r,\theta) = \frac{L_3 - L_2 a_2}{L_1} \qquad (1.12)$$

where

$$\begin{aligned} L_1 &= v_{gr} - v_t \sin\theta + \left(1 + \frac{2k\alpha}{v_{gr}\delta}\right) v_t \cos\theta, \quad L_2 = v_{gr} - v_t \sin\theta - \left(1 + \frac{2k\alpha}{v_{gr}\delta}\right) v_t \cos\theta \\ L_3 &= v_{gr} - v_t \sin\theta + \frac{v_t \cos\theta}{E}, \quad L_4 = (v_{gr} - v_t \sin\theta) \left(1 + \frac{2k\alpha}{v_{gr}\delta}\right) - v_t \cos\theta \\ L_5 &= (v_t \sin\theta - v_{gr}) \left(1 + \frac{2k\alpha}{v_{gr}\delta}\right) - v_t \cos\theta, \quad L_6 = v_{gr} - v_t \sin\theta - \frac{v_t \cos\theta}{E} \end{aligned} \qquad (1.13)$$

The parameters a_1 and a_2 are constants independent of r and θ ($a_1 = 1$ and $a_2 = 0$) only for a stationary TC and $\alpha = 0$ (i.e. $C_D \rightarrow \infty$, no slip conditions). Hence, Smith's (1968) axi-symmetric formulation, where a_1 and a_2 are assumed constant independent of r, is theoretically correct only in the case of no slip conditions at the surface boundary.

By combining equations (1.8)-(1.11) and after some algebra, one obtains the following system of differential equations in E and δ:

$$\begin{aligned} & B_1(r,\theta) \frac{\partial E}{\partial r} + B_2(r,\theta) \frac{\partial E}{\partial \theta} + B_3(r,\theta) \frac{\partial \delta}{\partial r} + B_4(r,\theta) \frac{\partial \delta}{\partial \theta} = -B_5(r,\theta) && \text{(a)} \\ & C_1(r,\theta) \frac{\partial E}{\partial r} + C_3(r,\theta) \frac{\partial \delta}{\partial r} + C_4(r,\theta) \frac{\partial \delta}{\partial \theta} = C_5(r,\theta) && \text{(b)} \end{aligned} \qquad (1.14)$$

with coefficients

$$\begin{aligned} & B_1 = r\delta R_o A_{10},\ B_2 = \delta R_o A_{12},\ B_3 = r R_o A_1,\ B_4 = R_o A_2 \\ & B_5 = \frac{kr}{\delta} A_6 + \delta R_o (r A_5 / R_o + A_3 + A_{13} + A_1 + r A_{11}),\ C_1 = r^2 R_o \delta (A_{12} - v_{gr} A_{16}) \\ & C_3 = r^2 R_o (A_2 - v_{gr} A_7),\ C_4 = r R_o (A_4 + A_{19} - v_{gr} A_8) \\ & C_5 = -\frac{kr^2}{\delta} A_9 + r R_o \delta [v_{gr} (A_{18} + r A_{17} + A_7 - A_{20}) - r A_7 / R_o - A_{15} - r A_{14} - 2 A_2] \end{aligned} \qquad (1.15)$$

Analytical expressions for the parameters A_1-A_{20} in equation (1.15) are derived in Appendix A.

The nonlinear system in equation (1.14) can be integrated numerically to obtain $E(r,\theta)$ and $\delta(r,\theta)$. For this purpose we use a scheme that is implicit in θ and explicit in r. Integration starts at $r=1$ where we set $E = 1$ and $\delta = \sqrt{2}$ (these are the values under geostrophic conditions) and moves inward using a stepwise integration procedure. At each step i in r, integration with respect to θ is performed simultaneously for all azimuthal locations using a central difference approach; see e.g. Chapra and Canale (2002).

Since the parameters in equation (1.14) depend on E and δ, a first approximation to the solution at step i is obtained by evaluating all parameters using the values of E and δ from step i-1. This procedure is iterated until E and δ at step i converge.

After E and δ (and hence the horizontal wind components U and V) are obtained, the vertical wind velocity W is calculated using mass conservation, as

$$W(R,\theta,Z) = -\frac{1}{R}\left[\int_0^Z \frac{\partial(RU)}{\partial R} dZ + \int_0^Z \frac{\partial V}{\partial \theta} dZ\right] \tag{1.16}$$

In what follows, we refer to equations (1.6) and (1.7) and their solution by the momentum integral method as the Modified Smith (MS) model. In the next section we compare results for a specific storm with wind estimates from the Shapiro (1983) and Kepert (2001) formulations and with MM5 simulations, and in Section 1.5 we examine how the winds generated by the MS model vary with a number of storm parameters.

1.4 Model Comparison

First we illustrate the results from the MS model and then compare the performance of that model with others for stationary and moving tropical cyclones.

Figure 1.1 shows the storm-relative radial and tangential wind velocity fields U and V and the vertical wind velocity W at elevations $Z = 0$, 0.5, 1 and 2km obtained using the MS model. The tropical cyclone translates eastward in the northern hemisphere, with velocity $V_t = 5$m/s. Asymptotically as $Z \rightarrow \infty$, the tangential winds satisfy Holland's profile in equation (1.1) with parameters $V_{max} = 50$m/s, $R_{max} = 40$km and $B = 1.6$. Results are for non-slip conditions at the surface boundary ($1/C_D = 0$) and constant vertical diffusion coefficient $K = K_M = 50\text{m}^2/\text{s}$. This value of K is often quoted in the literature (e.g. Smith, 1968; Shapiro, 1983; Kepert, 2001;

Kepert, 2006b) and is close to values extracted from MM5 simulations (M. Desflots 2006, personal communication). The Coriolis parameter f is set to 5 10^{-5} $\sec^{-1}$, which corresponds to a latitude φ of 20° North.

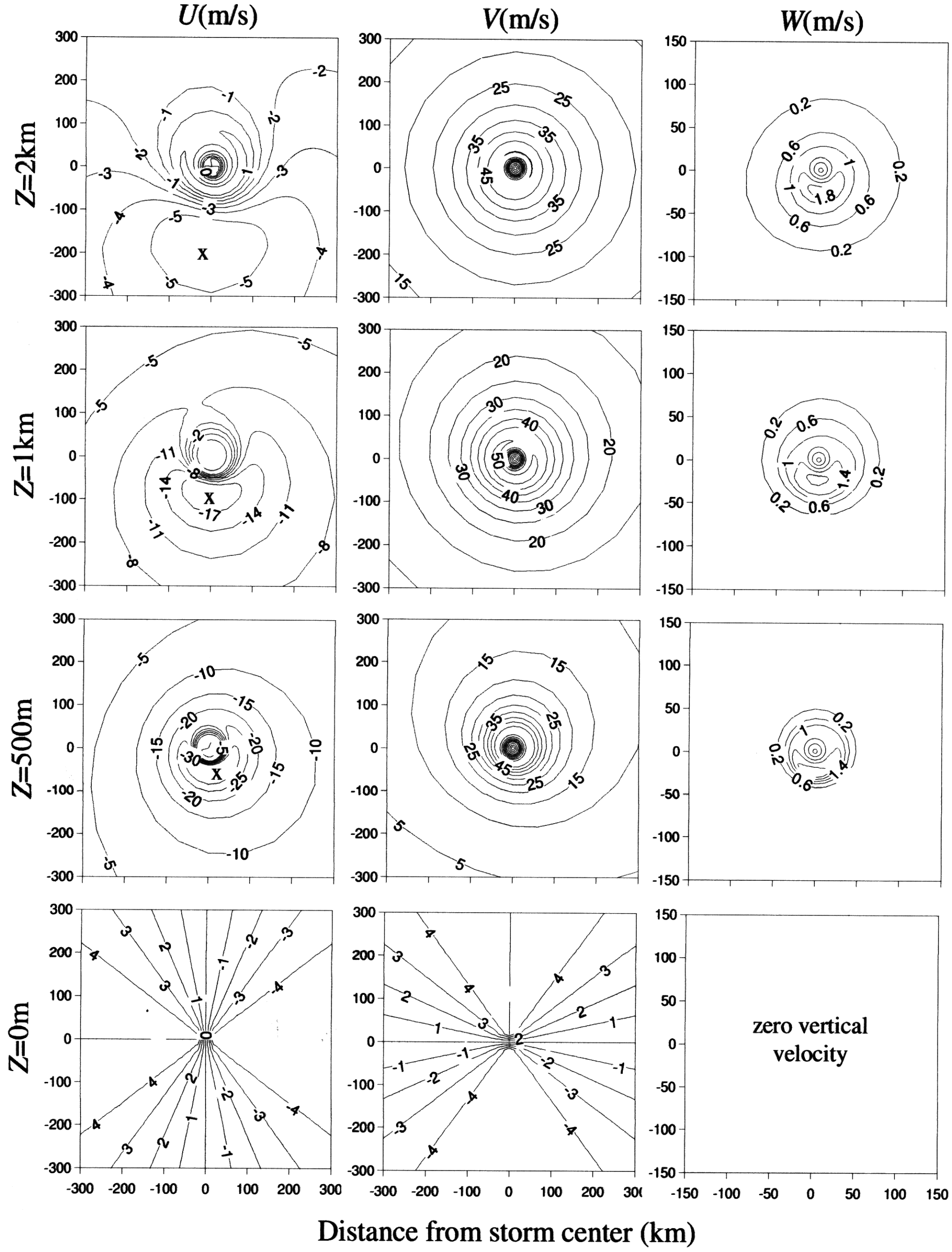

Figure 1.1: MS boundary layer solution for the tangential V, radial U and vertical W wind velocity fields at altitudes Z = 0, 0.5, 1, and 2km. V and U are velocities relative to the moving vortex. The location of the maximum of U is denoted by an x symbol. The tropical cyclone translates eastwards (to the right) with velocity V_t = 5m/s. All figures are generated under non-slip conditions at the surface boundary and using a constant vertical diffusion coefficient $K = 50\text{m}^2/\text{s}$. Other parameters are V_{max} = 50m/s, R_{max} = 40km and B = 1.6.

The model reproduces the conditions $U|_{Z=0} = -V_t \cos\theta$, $V|_{Z=0} = V_t \sin\theta$, and $W|_{Z=0} = 0$ at the surface boundary; see also discussion of Figure 1.2 below. Translation of the tropical cyclone causes intensification of the radial fluxes at the right and right-front of the vortex. Specifically, the maximum of U (x symbol in Figure 1.1) is located at the right/right-front of motion and close to the vortex center for Z = 500m, and moves outward while rotating clockwise as Z increases. Intensification of V is at the left-front of the vortex, with an asymmetry that decreases as one approaches gradient balance. Due to radial convergence at different altitudes, the vertical velocity W increases monotonically with Z. In addition, storm translation causes W to intensify at the right and right-front of the vortex. Similar qualitative findings on U, V and W have been reported by Kepert (2001) and Kepert and Wang (2001).

For the same storm, Figure 1.2 compares the vertical profiles of the azimuthally averaged radial and tangential winds generated by the MS and Kepert (2001) models. Azimuthal averaging produces results that correspond to a stationary, and hence, axi-symmetric TC. The profiles shown in Figure 1.2 are at radial distances $R = R_{max}$ = 40km and $R = 2.5R_{max}$ = 100km from the vortex center.

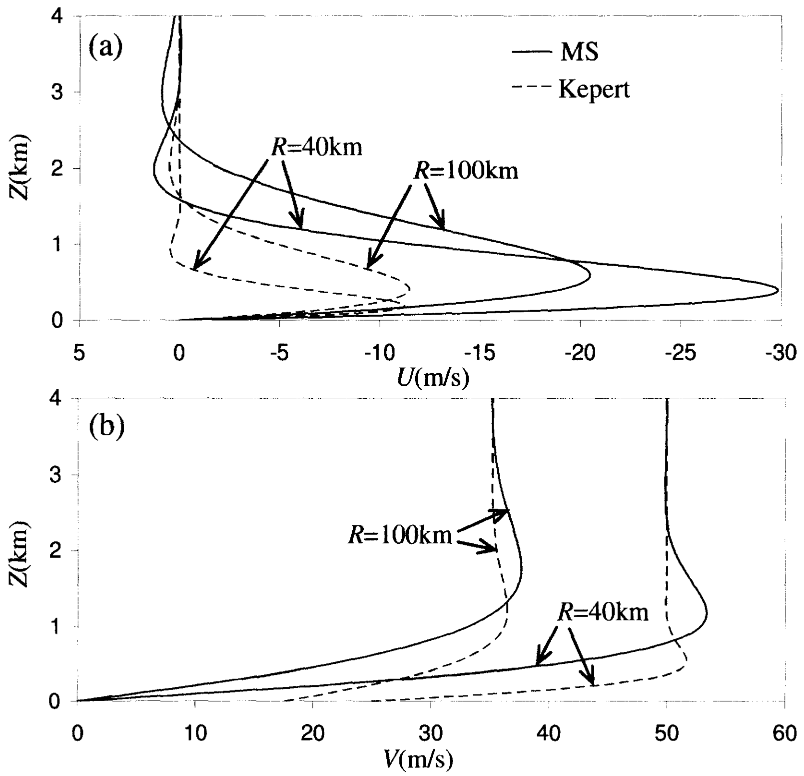

Figure 1.2: Comparison of the axi-symmetric component of the wind field from Kepert's (2001) model and the MS model. Vertical profiles of (a) the radial wind velocity U, and (b) the tangential wind velocity V at 40km and 100km from the vortex center. Same storm as in Figure 1.1.

As was pointed out in Section 1.2, the linearized stress formulation of Kepert (2001) is accurate only for small drag coefficients C_D. In the present case $C_D \rightarrow \infty$ and Kepert's (2001) model correctly reproduces the non-slip condition $U|_{Z=0} = 0$ in the radial direction (see Figure 1.2.a) but fails to reproduce the condition $V|_{Z=0} = 0$ in the tangential direction (Figure 1.2.b). This inconsistency results in underestimation of the frictional stresses at the surface boundary and hence of the radial fluxes relative to the MS formulation; see Figure 1.2.a and discussion of Figure 1.3 below.

Kepert's (2001) model also fails to reproduce the variation of the radial wind U with R. Observations using GPS dropsonde data (Kepert 2006a,b) show that the maximum of U increases as one approaches the center of the TC. While the MS model is consistent with this observation, the maximum values of U at 40 and 100km from Kepert's (2001) approach are about the same.

In both the MS and Kepert (2001) models, the depth of the boundary layer H, defined as the height Z where $U \approx 0$, increases with increasing R. In the MS solution, H is about 2.2km at R = 100km and about 1.5km at R = 40km, whereas the corresponding values from Kepert's (2001) analysis are 1.5 and 0.8km. Both sets of estimates are order-of-magnitude correct, with the MS values been closer to observations (e.g. Frank, 1977 and Kepert, 2006a).

Figures 1.3 and 1.4 compare the vertically averaged radial and tangential winds and the vertical winds obtained using the Shapiro (1983), Kepert (2001) and MS models as well as MM5 simulations. Figure 1.3 shows the radial variation of the axi-symmetric component, whereas Figure 1.4 includes the asymmetry due to motion through contour plots. The reasons for vertically averaging U and V (over a depth of 1km) are to ease model comparison, since Shapiro (1983) treats the BL as a slab of constant depth H = 1km, and to reduce the effect of vertical fluctuations in the MM5 solution. All storm parameters are the same as in Figure 1.1, except for the drag coefficient, which is set to 0.003. This value of C_D is close to values extracted from MM5 simulations for oversea conditions (M. Desflots 2006, personal communication), does not introduce significant distortions in Kepert's (2001) linear formulation, and does not cause numerical oscillations in Shapiro's (1983) approach. Also, values of C_D close to 0.003 are often quoted in the literature for wind speeds in the range encountered in hurricanes (e.g. Large and Pond, 1981; Powell *et al.*, 2003; Donelan *et al.*, 2004).

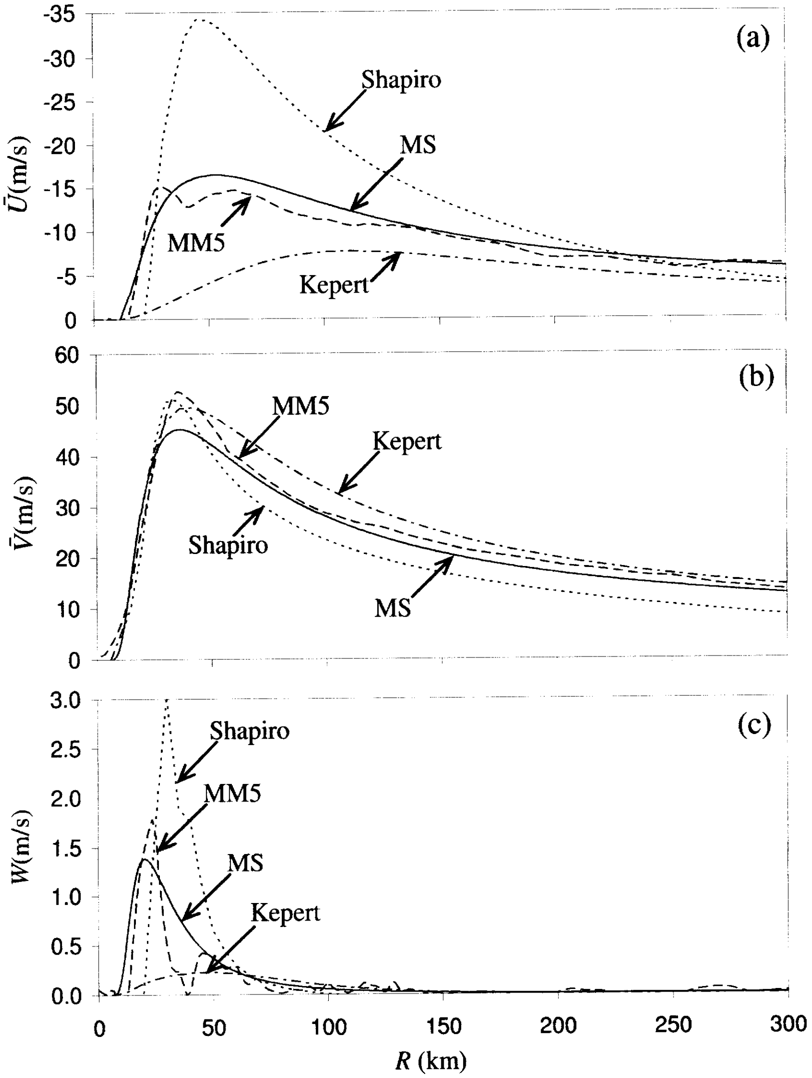

Figure 1.3: Comparison of the Shapiro (1983), Kepert (2001) and MS boundary layer solutions with MM5 simulations for an axi-symmetric (stationary) TC. (a) Vertically averaged radial wind velocity $\bar{U}$, (b) vertically averaged tangential wind velocity $\bar{V}$, and (c) vertical wind velocity W at an altitude of 1km. All figures are generated using a constant vertical diffusion coefficient $K = 50\text{m}^2/\text{s}$ and a surface drag coefficient $C_D = 0.003$ and averaging is over a depth of 1km. Other parameters are $V_{max} = 50$m/s, $R_{max} = 40$km and $B = 1.6$.

In general, the MS model predictions are close to the MM5 simulations, except that in MM5 the vertical velocities are more peaked near R_{max} (mainly due to rainband effects, which the BL models do not resolve) and the contour plots are more erratic due to local fluctuations. Also the Kepert (2001) model reproduces well the vertically averaged tangential winds of MM5, but that model severely underestimates the radial and vertical flows, especially in the near-core region. This is due to inaccuracy of Kepert's linearization at radial distances smaller than 2-3R_{max}; see Section 1.2. For example, flight observations show that, in the vicinity of R_{max}, W is in the range 0.5-3m/s or higher (Willoughby *et al.*, 1982; Jorgensen, 1984a, b; Black *et al.*, 2002), whereas

Kepert's (2001) estimates are around 0.1-0.4 m/s. In the far field ($R > 2.5R_{max}$), Kepert's (2001) model and MM5 produce vertical velocities that are similar and in good agreement with observations (Jorgensen 1984a, b; Black *et al.* 2002).

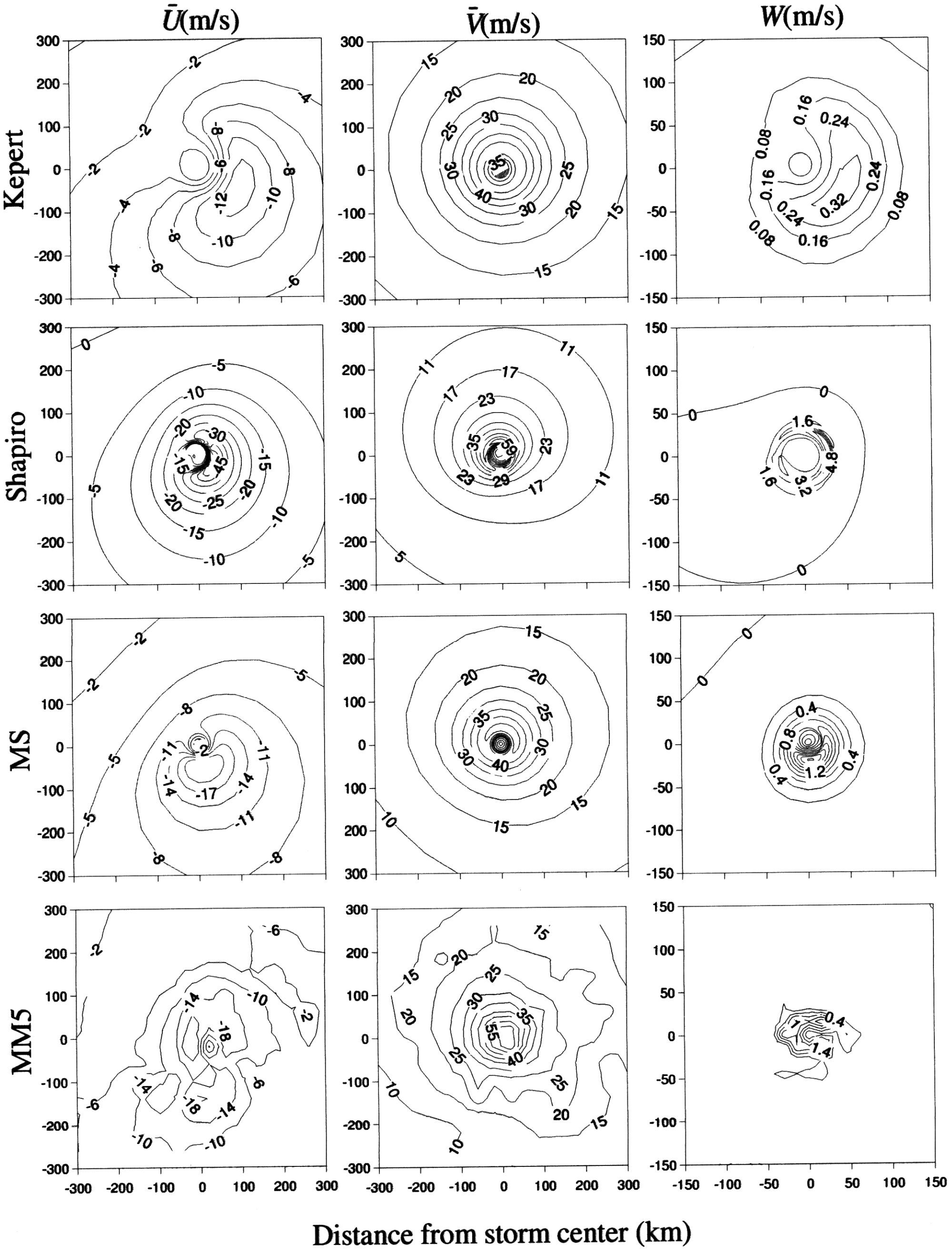

Figure 1.4: Comparison of results form the Kepert (2001), Shapiro (1983) and MS models with MM5 simulations for a TC that translates eastwards (to the right) with velocity $V_t = 5$m/s. Vertically averaged radial wind velocity $\bar{U}$ (left column), vertically averaged tangential wind velocity $\bar{V}$ (middle column) and vertical wind velocity W at an altitude of 1km (right column). $\bar{V}$ and $\bar{U}$ are relative to the moving vortex and averaging is over a depth of 1km. All other parameters are the same as in Figure 1.3.

Shapiro's (1983) model has an opposite behavior in the near-core region, where it overpredicts the radial and vertical flows by a factor of about 2. This is consistent with the finding by Anthes (1971) for slab-layer models; see Section 1.2.

Overall, we find that the MS model produces realistic estimates of the tangential, radial and vertical wind velocities and is numerically more stable and more accurate than the boundary layer models of Kepert (2001) and Shapiro (1983). Next we use the MS model to study the sensitivity of the velocity fields to various storm parameters.

1.5 Sensitivity Analysis

Figures 1.5, 1.6 and 1.7 show the sensitivity of MS model results to tropical cyclone characteristics: the tangential wind speed under gradient balance [parameterized here in terms of V_{max}, R_{max} and B; see equation (1.1)], the vertical diffusion coefficient K, the surface drag coefficient C_D, and the translation velocity V_t.

Figure 1.5 shows the sensitivity of the azimuthally averaged (axi-symmetric) velocities to V_{max}, R_{max}, B, K and C_D. The base case (solid lines in Figure 1.5) corresponds to the storm used in Figure 1.1. Sensitivity is evaluated by varying the parameters one at a time around their base-case values. V_{max} affects only the amplitude of the radial profiles, whereas other parameters affect mainly the shape of the profile (e.g. rate of decay with distance) or both. The effects on the three velocity components are however not uniform. For example, R_{max} has negligible influence on the peak value of the horizontal winds $\bar{U}$ and $\bar{V}$, but affects significantly the peak vertical velocity.

Figure 1.6 shows the effect of C_D on the wind fields for a TC that moves eastward with velocity V_t= 5m/s. Higher values of C_D correspond to increased friction at the surface boundary and stronger asymmetry of the three velocity components.

Finally, Figure 1.7 shows sensitivity to the translation velocity V_t when the other parameters are fixed at $V_{max} = 50$m/s, $R_{max} = 40$km, $B = 1.6$, $K = 50\text{m}^2/\text{s}$ and $C_D = 0.003$. One sees that $\bar{U}$ and W intensify in the NE quadrant relative to the direction of motion, whereas $\bar{V}$ intensifies to the left of the velocity vector. The asymmetry increases with increasing V_t.

Qualitatively similar sensitivity results are obtained when using Kepert's (2001) model (not shown here). This is expected, since Kepert's (2001) model is a linearized variant of the present

MS formulation. However, Kepert's linearization has approximate validity only for large R, C_D $\ll 1$ and small V_t; see Section 1.2.

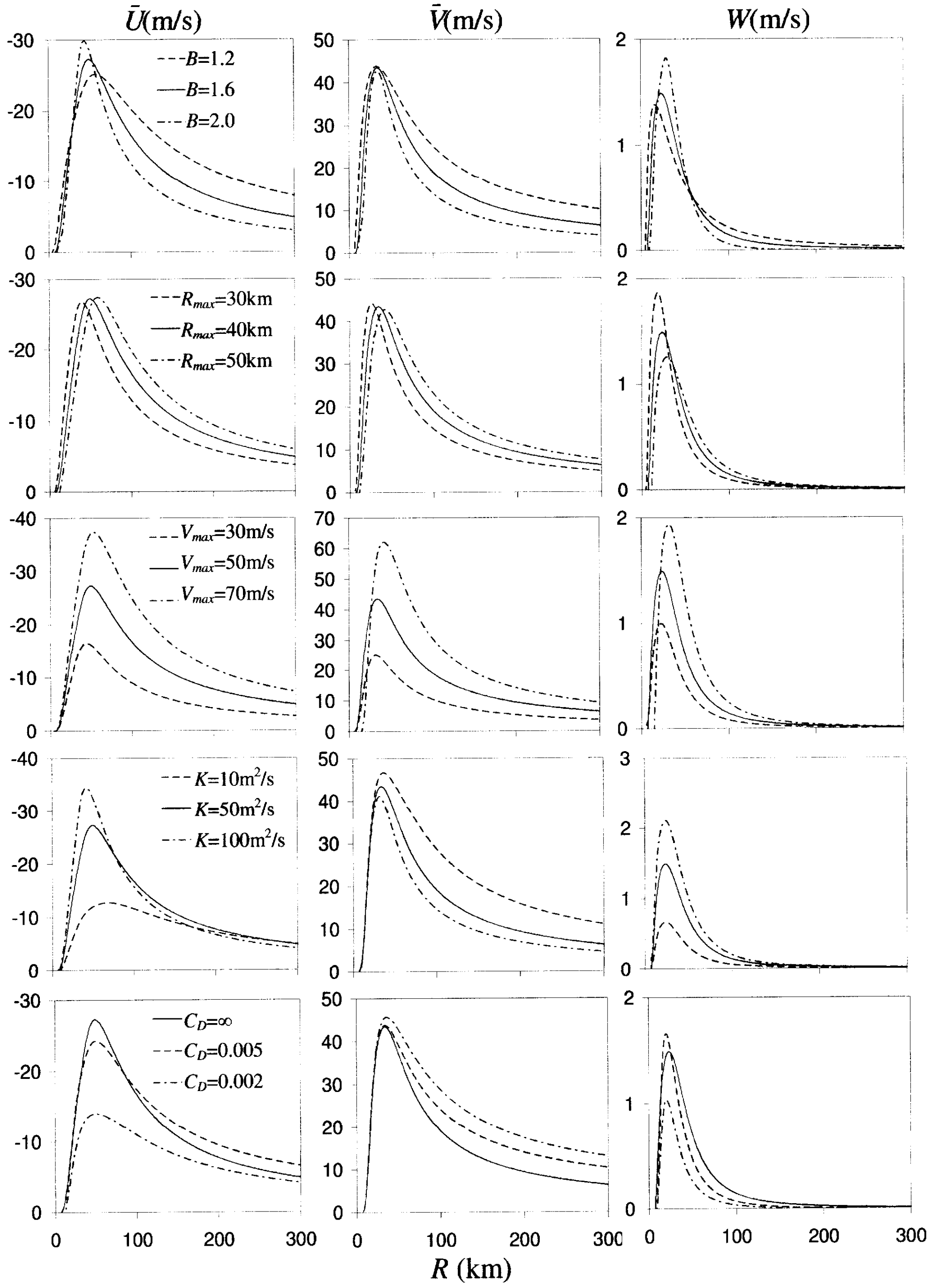

Figure 1.5: Sensitivity analysis of MS model results to storm parameters for a stationary TC. Vertically averaged (over a 1km depth) radial wind velocity $\bar{U}$ (left column) and tangential wind velocity $\bar{V}$ (middle column) and vertical wind velocity W at Z = 1km (right column). Solid lines correspond to V_{max} = 50m/s, R_{max} = 40km, B = 1.6, K = 50m^2/s and non-slip conditions at the surface boundary. Each row shows results under perturbation of one parameter.

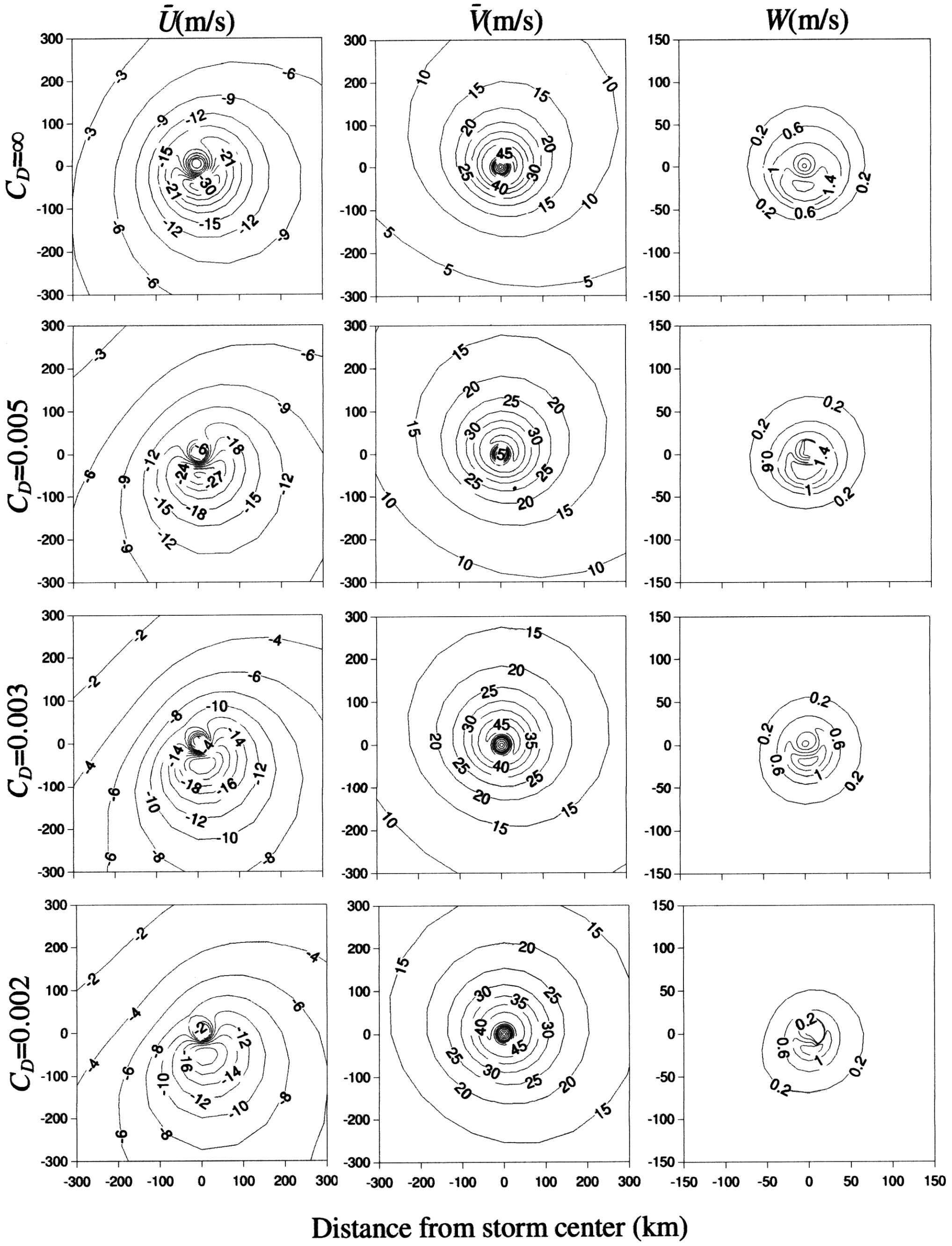

Figure 1.6: Sensitivity of MS results to the drag coefficient C_D for a tropical cyclone that translates eastwards (to the right) with velocity V_t =5m/s. Vertically averaged radial wind velocity $\bar{U}$ (left column), vertically averaged tangential wind velocity $\bar{V}$ (middle column), and vertical wind velocity W at an altitude of 1km (right column). $\bar{V}$ and $\bar{U}$ are relative to the moving vortex and averaging is over a depth of 1km. Other parameters are the same as in Figure 1.4.

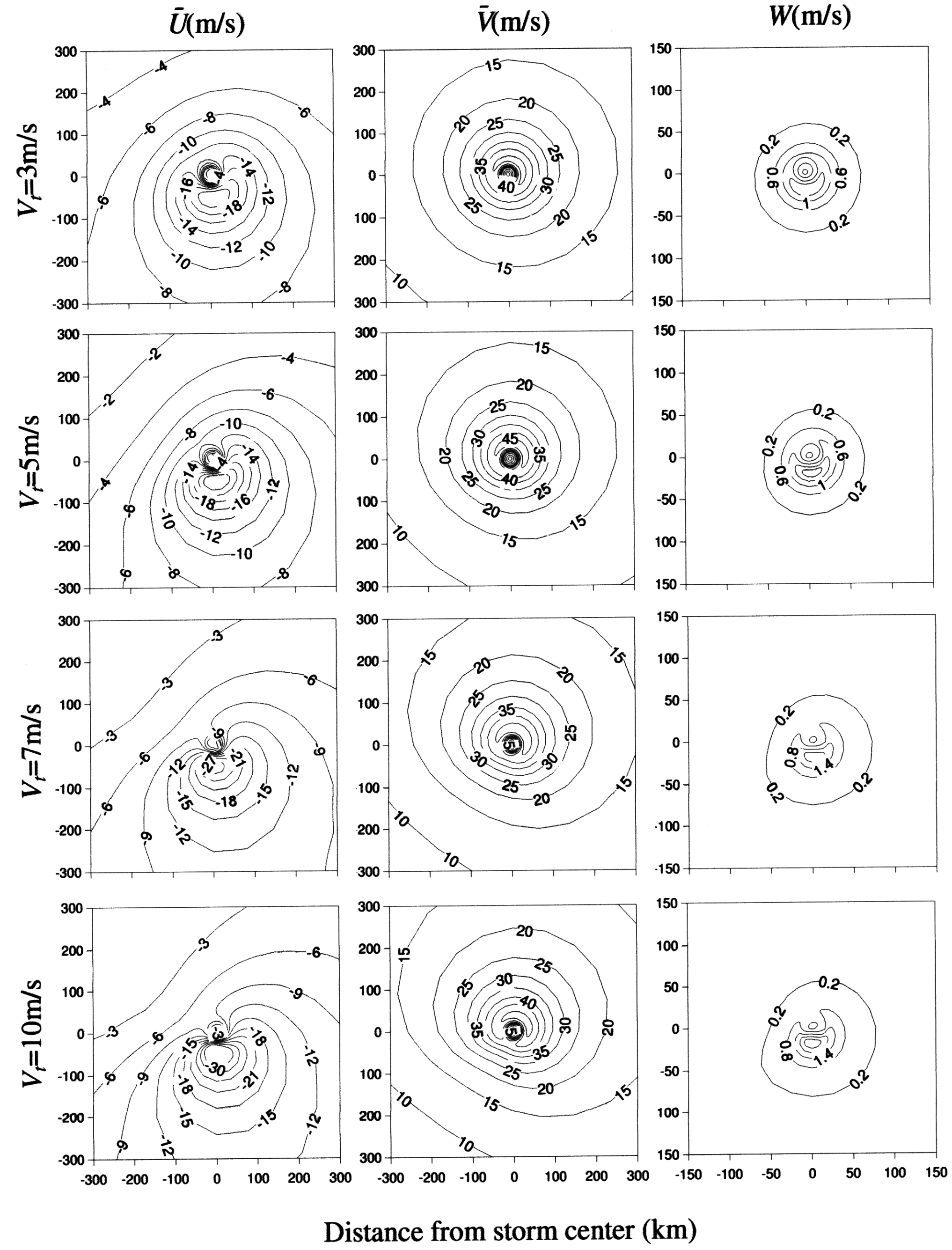

Figure 1.7: Sensitivity of MS model results to the translation velocity V_t. Notation and parameters are the same as in Figure 1.6, except for C_D=0.003.

1.6 Conclusions

We developed a simple theoretical model for the boundary layer (BL) of translating tropical cyclones (TCs). The model estimates the tangential, radial and vertical wind fields from a given radial profile of the tangential wind speed under geostrophic conditions [e.g. Holland's profile in equation (1.1)] and surface stress boundary conditions.

The model is based on Smith's (1968) formulation, which is corrected for the general case of a stress surface boundary (see Section 1.3) and modified to account for motion-induced asymmetries. The governing equations are solved using the momentum integral method, resulting in a very efficient computational scheme (less than a minute to run on a conventional computer). Contrary to the Shapiro (1983) and Kepert (2001) BL formulations, the present modified Smith (MS) model is stable over a wide range of storm parameters and produces results that are in good agreement with MM5 simulations and observations; see Figures 1.5, 1.6 and 1.7.

In a parametric analysis, we have examined how the symmetric wind components and motion-induced asymmetries generated by the MS model depend on various storm characteristics. For TCs that translate in the northern hemisphere, the vertical and storm-relative radial wind velocity fields intensify at the right-front quadrant of the vortex, whereas the storm-relative tangential winds intensify at the left-front of the storm. The asymmetry is higher for faster-moving TCs. These findings are in accordance with field observations; see for example Shapiro (1983).

As the intensity of the TC (expressed through the maximum tangential velocity at gradient balance V_{max}) increases, the horizontal and vertical velocity components also increase. Larger values of Holland's B parameter and lower values of the radius of maximum winds R_{max} produce horizontal and vertical wind profiles that are more picked and concentrated closer to the TC center.

The effect of the frictional drag coefficient C_D is more complex. As C_D increases, the frictional drag force also increases resulting in lower tangential winds and higher radial convergence (stronger vertical winds). Another effect of increasing C_D is higher asymmetry of the velocity field.

2. Theoretical Model of Rainfall in Tropical Cyclones for the Assessment of Long-Term Risk

2.1 Introduction

Tropical cyclones (TCs) are atmospheric disturbances capable of producing extreme rainfall with devastating social and economic impact (Landsea, 2000; Rappaport, 2000). Consequently, there is much interest in the assessment of the rainfall hazards posed by TCs, either in real time (with leads of hours or days) or in the long run; see e.g. Marks *et al.* (1998). For the latter purpose, when interest is in the rate at which different rainfall intensity levels are exceeded, one needs to parameterize the storms and for each set of parameters evaluate rainfall at the site or over the region of interest as a random process in time or a random field in space-time. In principle, the stochastic rainfall model could be directly fitted to data from historical events, but the large number of parameters and the relative lack of historical data make an empirical model identification and fitting approach unfeasible. Moreover, it would be difficult in such an approach to incorporate knowledge of the physics of the phenomenon. A better approach, which we follow here, is to formulate a physically-based rainfall model. The model should be simple enough that it can be run under a very large set of scenario conditions; hence detailed numerical TC models would not be suited for this purpose.

Neither simple nor sophisticated TC models can produce accurate statistical estimates of space-time rainfall for a given set of global TC parameters. Therefore, any deterministic rainfall model must be complemented by a statistical representation of the rainfall "residuals", defined as the difference between observed rainfall and model prediction. For example, the model developed here ignores the rainfall fluctuations due to rainbands and local convection. The statistical characterization of these fluctuations (residuals) is discussed in Chapter 3.

The third and final component of a long-term TC rainfall risk analysis method is the recurrence model, which specifies the frequency with which different TC parameter combinations occur in the region of interest. This component has been the subject of numerous studies, as the recurrence relation is common to the assessment of any TC-related risk, such as wind, waves and surges; see for example Vickery and Twisdale (1995), Vickery *et al.* (2000), Willoughby and Rahn (2004) and Powell *et al.* (2005).

In the late 1950s, R.H. Kraft (as referenced by Pfost, 2000, and Kidder *et al.*, 2005) used raingauge rainfall depths to estimate the maximum 24-hr rainfall accumulation due to the passage of a TC. According to Kraft, this maximum is 100 inches (254cm) divided by the storm translation speed in knots (1knot = 0.514m/s). Limitations of Kraft's analysis are that it does not provide information on the spatial distribution of rainfall and does not account for TC characteristics such as size and intensity.

Riehl and Malkus (1961), Goodyear (1968) and more recently Simpson and Riehl (1981) have addressed some of these limitations. From the examination of 46 TCs making landfall along the Gulf Coast of the United States, Goodyear (1968) concluded that the 48-hr maximum rainfall depth is about 150mm and occurs 40-80km inland and 40-80km to the right of the storm. Using a similar approach, Riehl and Malkus (1961) and Simpson and Riehl (1981) found that for hurricane-strength cyclones rainfall intensity averages about 33mm/h within 37km from the cyclone center and for larger distances decays almost exponentially. While these studies extend and improve upon Kraft's rule, they too fail to resolve the dependence of rainfall on storm characteristics.

NASA's Tropical Rainfall Measuring Mission (TRMM) (Simpson *et al.*, 1988) produced vast amounts of TC rainfall data, making it possible to conduct more systematic statistical analyses. Lonfat *et al.* (2004) extracted 2121 tropical cyclone microwave images from the TMI TRMM data set to find how the azimuthally averaged rainfall intensity varies with distance R from the TC center in three storm intensity ranges: tropical storms (TSs) with maximum tangential wind speed V_{max} in the range 18-33m/s; CAT12 cyclones with $V_{max} =$ 34-48m/s and CAT35 cyclones with $V_{max} >$ 49m/s. The study concluded that TC rainfall intensifies with increasing V_{max} and the symmetric component of the rainfall intensity reaches its maximum at a distance from the hurricane center close to the radius of maximum winds R_{max}. For larger distances, rainfall intensity decays approximately as a power law; see their Figure 11. Due mainly to storm translation and vertical wind shear, rainfall intensity lacks circular symmetry and varies also with the azimuth relative to the directions of shear and motion.

Chen *et al.* (2006) used the same TRMM storms to further assess the dependence of rainfall on vertical wind shear S, defined as the difference between the 200 and 850-hPa horizontal wind velocities in the annular region between 200 and 800km from the TC center. The study calculated the average rainfall asymmetry, defined as the ratio of the wavenumber-1 Fourier amplitude to the azimuthal average of the rainfall intensity, for the nine combinations of the 3 intensity categories in Lonfat *et al.* (2004) and three shear magnitude ranges ($S < 5$m/s, $5 \leq S \leq 7.5$m/s, and $S > 7.5$m/s). Chen *et al.* (2006) found that, in storms in the Northern (Southern) hemisphere with high wind shear ($S > 5$m/s), rainfall intensifies downshear and downshear-left (-right) of the storm.

Parametric rainfall models have also been developed. Using the radial rainfall profiles of Lonfat *et al.* (2004), Tuleya *et al.* (2007) suggested one such model for 24-hr rainfall totals (R-CLIPER) based on climatological and persistence information. The model assumes that storms are symmetric and therefore ignores vertical wind shear and storm motion. Lonfat *et al.* (2007) built on the R-CLIPER algorithm to construct a parametric rainfall model (PHRaM) that includes shear-related asymmetries according to the results of Chen *et al.* (2006).

Due to data limitations, R-CLIPER and PHRaM use a coarse and incomplete storm parameterization: the effects of storm intensity and vertical wind shear are modeled by interpolating from 3 classes of each variable, the size of the vortex R_{max} is only implicitly taken into account by allowing the location of the maximum rainrate depend on the intensity of the storm according to the results of Lonfat *et al.* (2004), while other factors (e.g. the radial wind velocity profile in the main vortex, the surface roughness, and the storm translation velocity) are ignored. Another limitation is that the Lonfat *et al.* (2004) profiles on which R-CLIPER and PHRaM are based use ensemble averages of storms with significantly different R_{max} values. Since rainfall intensity has a sharp peak near R_{max}, this averaging operation depresses the maximum rainfall estimate. For example, for CAT35 storms Lonfat *et al.* (2004) find maximum rainfall intensities around 12mm/h, which is 2.5-3 times lower than the values most often reported in the literature; see for example Riehl and Malkus (1961), Jiang *et al.* (2006), Trenberth *et al.* (2007) and the rainfall intensities implied by the radar reflectivities in Marks (1985) and Kepert (2006a,b). Finally, the Lonfat *et al.* (2004) profiles are based on TMI rainfall products, which are known to be biased towards low values for high rainfall intensities and towards high values for low rainfall intensities (Viltard *et al.*, 2006).

Here we develop a simple theoretical model of TC rainfall based on the vertical outflow of water vapor from the TC boundary layer (BL). This water vapor flux originates from the low-level convergence of the horizontal flow. The analysis combines a user-specified tangential wind profile at gradient level, an Ekman-type solution for the horizontal and vertical winds inside the boundary layer (BL), and basic thermodynamics. Evaluation of the BL winds is based on Smith's (1968) axi-symmetric formulation, modified in Chapter 1 to account for storm motion. The resulting models of wind and rainfall are referred to as the modified-Smith (MS) BL model and the modified-Smith-for-rainfall (MSR) model, respectively.

The MSR model produces asymmetric rainfall fields that explicitly depend on: the maximum tangential wind velocity at gradient level V_{max}, the radius of maximum winds R_{max}, Holland's B parameter (Holland, 1980), the surface drag coefficient C_D, the storm translation velocity V_t, the vertical diffusion coefficient of the horizontal momentum K, and the average temperature $\bar{T}$ and saturation ratio $\bar{Q}$ inside the TC boundary layer.

An important departure from previous studies is that we parameterize asymmetries in terms of storm motion not vertical wind shear. The degree to which TC motion and shear contribute to wind, lightning, and rainfall asymmetries has been intensely discussed in the literature; see for example Black *et al.* (2002), Corbosiero and Molinari (2002, 2003), Rogers *et al.* (2003), Lonfat *et al.* (2004) and Chen *et al.* (2006). Separation of the two effects through data analysis is made difficult by the high correlation between the directions and magnitudes of motion and shear in any given geographical region (Corbosiero and Molinari, 2003; Lonfat *et al.*, 2004; Chen *et al.*, 2006). As a consequence, the calculated rainfall asymmetry is almost the same when storms are aligned in the direction of motion or shear, except for a region-specific rotation; see e.g. Corbosiero and Molinari (2003) and Section 2.5 below. Another consequence is that, in risk analysis, one may equivalently use shear or motion as conditioning parameter. Since it is easier to include motion than shear when modeling rainfall and the historical records readily provide storm motion information (e.g. Vickery and Twisdale, 1995, and Vickery *et al.*, 2000), we have chosen to develop a motion-based rather than shear-based parameterization of rainfall asymmetry.

Section 2.2 summarizes the boundary layer model developed In Chapter 1 and Section 2.3 uses the vertical fluxes from that model to estimate surface rainrates in the case of stationary (i.e. symmetric) cyclones. Model predictions are compared to MM5 simulations and R-CLIPER rainrate estimates. The choice of MM5 is based on the fact that this code has been successfully used to simulate a number of TCs, including Hurricanes Bonnie (1998) (Rogers *et al.* 2003, 2007), Floyd (1998) (Tenerelli and Chen, 2001, Rogers *et al.* 2007) and Frances (2004) (Chen *et al.*, 2007). Section 2.4 validates the symmetric MSR predictions using precipitation radar (PR) rainfall products from 38 TRMM frames. The PR rainfall products are less biased than the microwave imager (TMI) data used in previous studies, especially in the core region where rainfall intensities are high (Viltard *et al.*, 2006). Section 2.5 extends the analysis to translating TCs, which generate asymmetric rainfall fields, assesses the effect of motion on the spatial variation of TC rainfall, and suggests a motion-based parameterization of rainfall asymmetry. Section 2.6 assesses the sensitivity of the symmetric and asymmetric rainfall components to various TC parameters and Section 2.7 summarizes the main conclusions.

2.2 Modified Smith Boundary Layer Model for Moving Tropical Cyclones

A number of studies (Myers and Malkin 1961; Shapiro 1983; Kepert 2001) have developed theoretical boundary layer (BL) models for moving tropical cyclones. These models derive the radial, tangential and vertical winds inside the boundary layer from an assumed radial profile of the tangential wind velocity under gradient balance, $V_{gr}(R)$, and suitable surface boundary conditions. For example, a widely used gradient wind profile is (Holland, 1980)

$$V_{gr}(R) = V_{max}\sqrt{(R_{max}/R)^B \exp[1-(R_{max}/R)^B]} \tag{2.1}$$

where V_{max}, R_{max}, and B are TC-specific parameters. According to equation (2.1), the tangential velocity V_{gr} increases radially to a maximum V_{max} at $R = R_{max}$ and for $R >> R_{max}$ decays approximately as a power-law of distance with exponent $-B/2$. The shape parameter B varies in the range [1, 2], with typical values around 1.4 (Willoughby and Rahn, 2004). Next we briefly describe the boundary layer model developed in Chapter 1 and in Sections 2.3-2.5 use this model to calculate water vapor fluxes that are responsible for rainfall.

The model in Chapter 1 corrects Smith's (1968) BL formulation for the case of stress surface boundary conditions and accounts for storm motion. Like in Smith (1968), vertical diffusion of the horizontal momentum is parameterized through a vertical diffusion coefficient K. The horizontal momentum equations are written in cylindrical coordinates that move with the storm and solved using the Karman and Pohlhausen momentum integral method. In this method, one specifies vertical profiles for the radial U and tangential V wind velocity components, which satisfy the boundary conditions at the surface (elevation $Z = 0$) and for $Z \rightarrow \infty$ tend to the gradient winds, for example the profile in equation (2.1). The boundary conditions are modeled using a surface stress formulation with drag coefficient C_D.

For U and V, we use functions of the Ekman type with parameters E (amplitude coefficient) and δ (dimensionless BL scale thickness) that vary both radially and azimuthally. The horizontal momentum equations are vertically integrated through the BL to produce a system of two partial differential equations, which are solved numerically to obtain E and δ as functions of radius R and azimuth θ relative to the direction of storm motion. Once the horizontal wind components U and V are obtained, the vertical wind velocity W is calculated using mass conservation, as

$$W(R,\theta,Z)=-\frac{1}{R}\left[\int_0^Z \frac{\partial(RU)}{\partial R}dZ+\int_0^Z \frac{\partial V}{\partial \theta}dZ\right] \tag{2.2}$$

For stationary cyclones ($V_t = 0$), there is no azimuthal variation of V and U and equation (2.2) reduces to

$$W(R,Z)=-\frac{1}{R}\frac{d}{dR}\left(R\int_0^Z U\,dZ\right) \tag{2.3}$$

$W(R,Z)$ in equation (2.3) is also the symmetric component of the vertical wind speed for a storm that translates with velocity $V_t \neq 0$.

The above modified Smith (MS) scheme is computationally very efficient and stable over a wide range of parameter values. Model predictions are close to MM5 simulations and to observed wind speeds; see Chapter 1 for details.

2.3 Estimation of the Symmetric Component of Rainfall

Estimates of rainfall intensity are obtained assuming that, with corrections to be made later, the surface rain rate i is proportional to the water vapor up-flux at a reference height H. Similar approaches have been used in the past to evaluate the rainfall potential of extra-tropical storms (Palmen, 1958), orographic precipitation (Alpert, 1986) and latent heat (Magaki and Barros, 2004), as well as to predict rainfall extremes (Abbs, 1999; Wilson and Toumi, 2005).

To verify how strongly rainfall intensity is related to the vertical velocity $W_H(R,\theta)= W(R,\theta,Z=H)$ from equation (2.2) at different elevations H, we used MM5 simulations. Figure 2.1 shows the correlation between the two quantities using 12 frames of Hurricane Frances, simulated at 6 hr intervals for the period Aug. 29-Sep. 01, 2004. The correlation is maximum around 0.85 at an elevation of 2-3km, which can be taken as the reference height H. The inset of

Figure 2.1 compares the MM5 radial profiles of the simulated rainfall intensity and vertical wind velocity at 3km elevation for the 06:00UTC Aug. 29, 2004 frame. Both profiles are normalized to have unit maximum value. This detailed comparison shows that the correlation coefficient is below 1 due mainly to fluctuations of the rainfall intensity caused by rainbands and other local convective phenomena. If these fluctuations in the MM5 profiles are smoothed out, which is what the present MSR model effectively does, the surface rainfall intensity and vertical wind speed are in even better agreement.

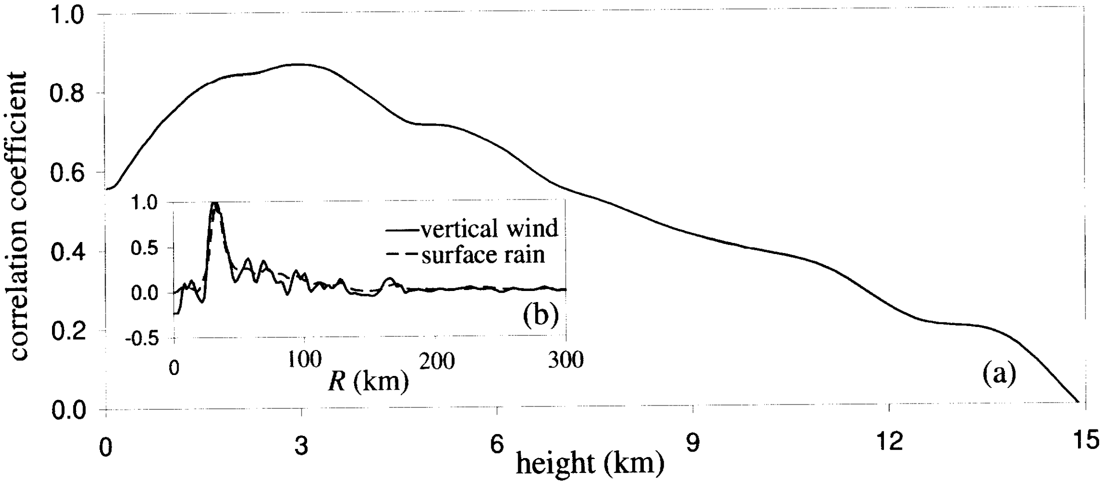

Figure 2.1: (a) Ensemble correlation function of the vertical wind velocity at different elevations and the surface rainfall intensity from MM5 simulations of Hurricane Frances. Ensemble averaging is over 12 frames (at 6 hr intervals) during the period Aug. 29-Sep. 01, 2004. (b) Normalized radial profiles of surface rainfall intensity and vertical wind velocity on Aug. 29, 2004 at 06:00UTC at 3km elevation.

To complete the symmetric rainfall model one needs the proportionality constant between rainfall intensity and vertical wind speed. From simple calculations using a lapse-rate of about 6-7 °C/km (Rogers and Yau, 1996), one obtains that at elevations in excess of 6-8km the water vapor mixing ratio is close to zero. Consequently, one may accurately assume that the upward water vapor flux from the TC boundary layer equals the downward flux of rainwater. To keep the rainfall model simple, we assume that below the reference height H the temperature T and saturation ratio Q are constant and equal to the depth-averaged values $\bar{T}$ and $\bar{Q}$. For cyclones over tropical and sub-tropical waters, $\bar{T}$ ranges between 20-24°C and $\bar{Q}$ is between 75-85%; see Gray *et al.* (1975), Frank (1977) and Smith (2003). Under these conditions, the symmetric rainfall intensity i_{sym} is given by

$$i_{sym}(R) = \begin{cases} \alpha(\bar{T})\ \bar{Q}\ W_H(R) & , \quad W_H(R) > 0 \\ 0 & , \quad W_H(R) \leq 0 \end{cases} \tag{2.4}$$

where $\alpha(\bar{T})$ is the volume of liquid water per unit volume of saturated air after complete condensation (see below), and $W_H(R) = W(R,Z{=}H)$ is the vertical wind velocity in equation (2.3) for $Z = H$. The function $\alpha(\bar{T})$ is obtained by combining the ideal gas law with the Clausius-Clapeyron equation. Using a liquid water density $\rho_w = 1000\text{kgr/m}^3$, this gives

$$\alpha(\bar{T}) = \frac{1.324\ 10^{-3}}{\bar{T}+273} \exp\left(\frac{17.67\ \bar{T}}{\bar{T}+243.5}\right) \tag{2.5}$$

where $\bar{T}$ is in °C. Notice that in downdraft regions where W_H is negative, equation (2.4) sets the rainfall intensity to zero. This means that rainfall generation is limited to regions where moist air updrafts. However, due to the slant of the wall updrafts and the cyclonic advection, rainfall may be nonzero also in downdraft regions. This effect is modeled below through a rainfall redistribution scheme.

2.3.1 Correction for the sloping angle of the wall

Flight observations (e.g. Jorgensen, 1984b; Marks and Houze, 1984) show that the wall updraft of a tropical cyclone slopes outward to altitudes $H_0 \approx$ 5-7km, with an angle ψ_0 from the vertical in the 45°-60° range. The MS model in Chapter 1 assumes fixed vertical profiles of the radial and tangential wind velocities and therefore does not account for such sloping angle. Consequently, equation (2.4) tends to underpredict the radius of maximum rainfall.

To include radial advection of the rainwater by the wall updraft while avoiding discontinuities in the radial distribution of rainfall, we assume that the angle of the updrafts decreases exponentially with distance R from the storm center, as

$$\psi(R) = \psi_0 \exp\left(-\frac{|R-R_m|}{R_m}\right) \tag{2.6}$$

where R_m is the location where i_{sym} and W_H in equation (2.4) are maximum. The outward radial displacement ΔR of the rainwater due to the sloping updrafs is then

$$\Delta R = H_0 \tan\psi \tag{2.7}$$

Notice that estimating rainfall intensities at distance R from the cyclone center as $i_{sym}(R-\Delta R)$ is technically incorrect because the model does not satisfy mass conservation. However, we have verified that the error is very small and negligible in practice.

2.3.2 Comparison with MM5 and R-CLIPER

Figure 2.2 compares the azimuthally averaged rainfall intensities i_{sym} for Hurricane Frances (2004) estimated by MM5, R-CLIPER (see Introduction), and the present modified-Smith-for-rainfall (MSR) model. The MM5 and MSR curves are the ensemble averages of 12 rainfields simulated at 6 hr intervals during the period Aug. 29-Sep. 01, 2004, using the two models.

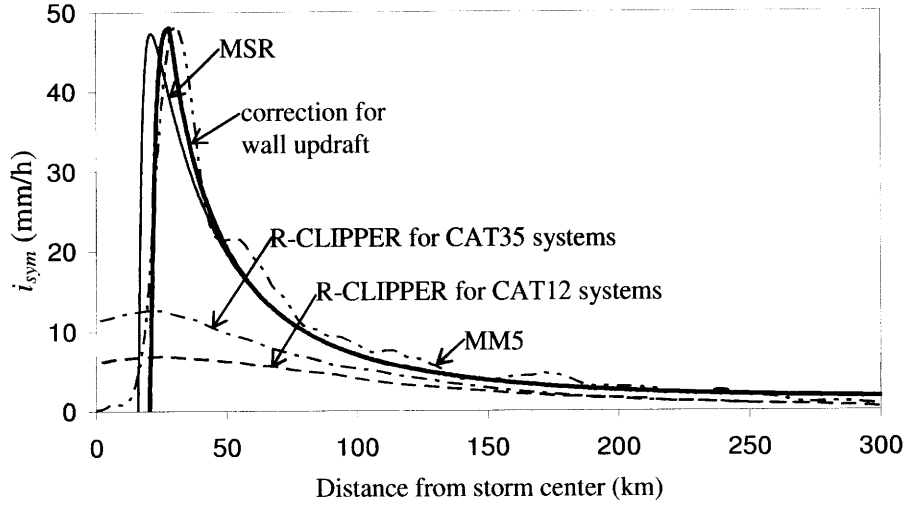

Figure 2.2: Comparison of the ensemble average rainrates for Hurricane Frances 2004 during the period Aug. 29-Sep. 01, produced by the MSR, MM5 and R-CLIPER rainfall models.

The MM5 simulations where conducted at 1.67km resolution using the nested grid capability at the University of Miami (Houze *et al.*, 2006; 2007), whereas the MSR estimates were obtained as follows:

1) For each frame, the parameters V_{max} and R_{max} in equation (2.1) were extracted from the azimuthally averaged tangential winds simulated by MM5 at 5km elevation;
2) Holland's (1980) gradient wind profile with $B = 1$ was used in the MS model in Chapter 1 to calculate the vertical wind profile $W_H(R)$ at elevation $H = 3$km;
3) Equations (2.4) and (2.5) were used to estimate how the azimuthally averaged rainfall intensity i_{sym} varies with distance R from the TC center;
4) Finally, the results were corrected for sloping-updrafts using equations (2.6) and (2.7) and averaged over the 12 frames.

Setting Holland's B to 1 reproduces well the MM5 rainfall fields, as well as the PR rainfall estimates from TRMM; see Section 2.4.

The MS model in Chapter 1 requires also specification of the Coriolis parameter f, the vertical diffusion coefficient K, and the surface drag coefficient C_D. In our simulations we have set $f = 4.7\ 10^{-5}\ \text{sec}^{-1}$, which corresponds to latitude 19° North (the approximate latitude of TC Frances during the period considered), $K = 50\text{m}^2/\text{s}$, and $C_D = 0.002$. Values of K near $50\text{m}^2/\text{s}$ are often quoted in the literature (e.g. Smith, 1968; Shapiro, 1983; Kepert, 2001; Kepert 2006b) and are consistent with back-calculations from MM5 simulations (Melicie Desflots, 2007, personal communication). The value 0.002 is representative of drag coefficients extracted from oversea MM5 simulations and to values in the literature for winds in the hurricane range (e.g. Kepert, 2001; Powell *et al.*, 2003; Donelan *et al.*, 2004). The vertically averaged temperature $\bar{T}$ (over a depth of 3km) and saturation ratio $\bar{Q}$ in equation (2.4) have been set to 22°C and 80%, respectively. These values correspond to a depth-averaged mixing ratio of approximately 13gr/kg, which is slightly lower than the ensemble average value of 15gr/Kg extracted from MM5 simulations for Hurricane Frances (Melicie Desflots, 2007, personal communication). For the wall updraft correction in equations (2.6) and (2.7), we have assumed an outwards slope of $\psi_0 = 50°$ from the vertical to an altitude $H_0 = 6\text{km}$.

The solid lines in Figure 2.2 are the profiles of i_{sym} before the correction for sloping updrafts (thin lines) and after that correction (thick lines). The rainfall estimates from the MSR model are close in shape and magnitude to the MM5 profiles. This is especially true after the correction for out-sloping updrafts. Differences are mostly due to local rainfall intensifications in MM5 caused by rainbands. By contrast, the rain rates of Lonfat *et al.* (2004), which form the basis of the R-CLIPER algorithm, agree with MM5 in the far field but severely underestimate rainfall in the near-core region. As discussed in the Introduction, reasons for the much-reduced rain rate maximum in R-CLIPER are the smoothing effect of ensemble averaging and the bias of the TMI rainfall retrievals used by Lonfat *et al.* (2004).

2.4 Validation of Symmetric MSR Predictions

Figure 2.3 compares PR and MM5 rainfall estimates with rainfall intensities generated by the present MSR model using the procedure described in Section 2.3. Figure 2.3.a shows a scatterplot of the ratio between the PR and MSR rainfall estimates as a function of the normalized distance R/R_{max} from the storm center, using a 5km × 5km grid of spatial locations and the 38 TRMM frames in Table 2.1 (a total number of 48483 points). The number of points in different ranges of R/R_{max} is shown in Table 2.2.

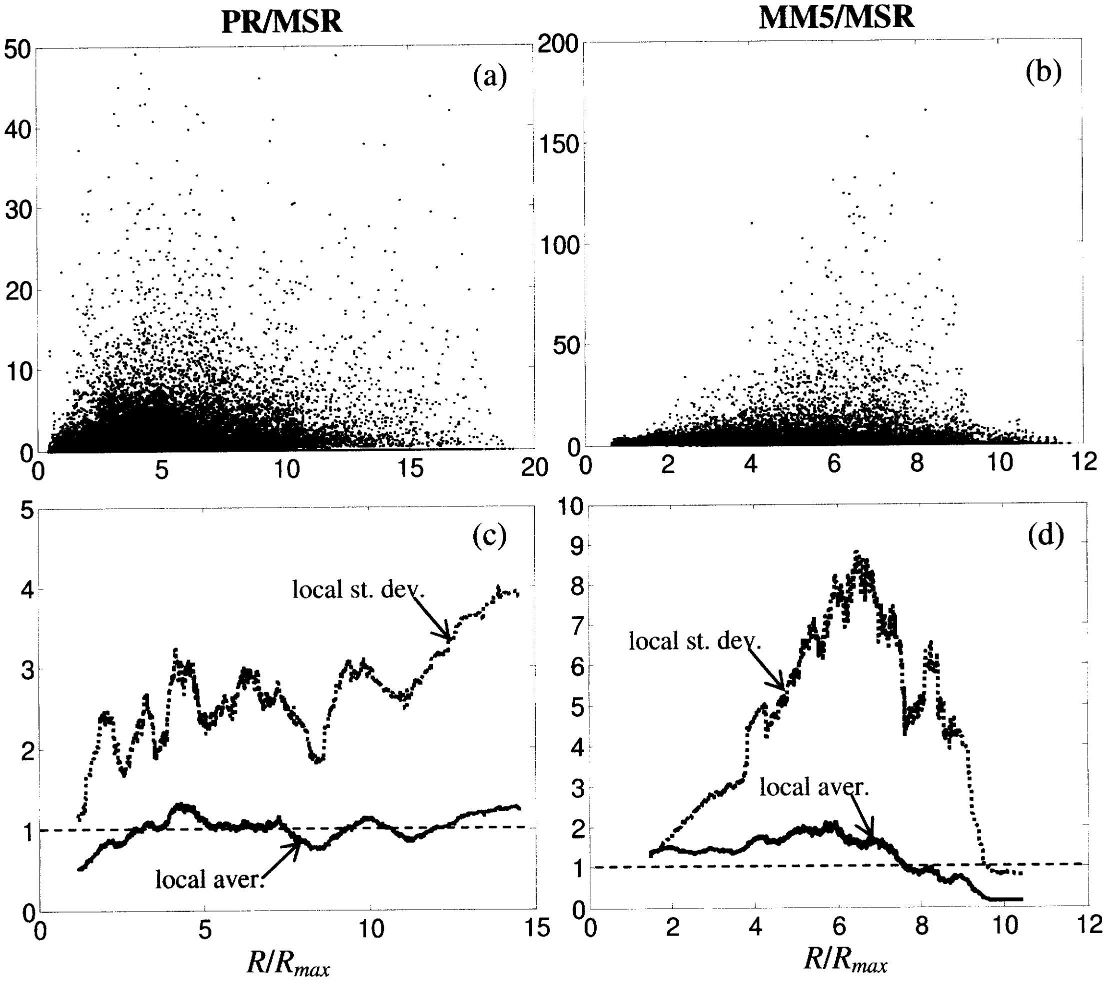

Figure 2.3: Comparison of PR, MM5 and MSR point rainfall intensity estimates. (a) Scatterplot of the ratio between PR and MSR rainfall estimates as a function of the normalized distance R/R_{max} from the storm center, for 38 TRMM frames; see Table 2.1. The number of data points in different ranges of R/R_{max} is shown in Table 2.2. (b) Scatterplot of the ratio between MM5 and MSR rainfall estimates as a function of R/R_{max}, for hurricane Frances 2004 during the period Aug. 29-Sep. 01. (c) Local averages and standard deviation of the ratios in (a) using a moving window of 2000 points. (d) Same as (c) but for the ratios in (b).

The MSR estimates where generated using the V_{max}, R_{max} and latitude information in the extended best track record (Demuth *et al.*, 2006; M. DeMaria, 2008; personal communication). Figure 2.3.b shows a similar scatterplot of the ratio between the MM5 and MSR rainfall estimates. In this case the comparison is based on the 12 simulated rainfields of Hurricane Frances, for a total of 43919 points. All MSR simulations were performed using $B = 1$, $K = 50\text{m}^2/\text{s}$ and $C_D = 0.002$. Both Figures 2.3.a and 2.3.b show a large dispersion, which reflects the significant small-scale variability of rainfall intensity due to rainbands and local convection. Those fluctuations are not resolved by the MSR model.

Table 2.1: Storm characteristics for the PR-TRMM rainfields used in Figure 2.3. The estimates of V_{max} and R_{max} are obtained from the extended best track record (M. DeMaria, 2008; personal communication).

	Storm center		**V_{max} (m/s)**	**R_{max} (km)**	**Intensity category**
	Lat. (deg)	**Lon. (deg)**			
Floyd '99	21.7	-61.6	48.8	41	CAT2
	23.5	-68.7	64.0	37	CAT4
	23.7	-70.6	69.3	37	CAT4
Frances '04	12.6	-43.7	23.1	37	TS
	15.7	-49.8	51.4	19	CAT3
	17	-51.3	54.0	28	CAT3
	17.9	-52.6	59.1	28	CAT4
	19	-57.3	51.4	28	CAT3
	21.2	-68.5	61.7	28	CAT4
Ivan '04	8.9	-38.9	25.7	37	TS
	10.7	-50.6	57.5	28	CAT4
	11.2	-53.4	51.4	28	CAT3
	12.3	-64.1	61.7	19	CAT4
	12.7	-66.2	61.7	20	CAT4
	17.4	-77.3	66.8	28	CAT4
	17.7	-78.4	64.3	28	CAT4
	25.6	-87.4	61.7	46	CAT4
Jeanne '04	27.4	-70.6	38.6	42	CAT1
	25.5	-69.5	41.1	37	CAT2
	26.5	-74.3	43.7	60	CAT2
	26.5	-75.6	46.3	46	CAT2
Karl '04	11.5	-35.3	26.7	37	TS
	17.3	-45.5	57.8	32	CAT3
	19.1	-47.4	64.0	32	CAT4
	22.9	-48.6	54.0	28	CAT3
	25.7	-49.5	48.8	28	CAT3
Katrina '05	24.6	-85.6	51.5	56	CAT3
	25	-86.2	56.5	50	CAT3
	26.9	-89	75.0	38	CAT5
Lilli '02	23.6	-87.2	51.5	20	CAT2
	24.4	-88.4	56.5	20	CAT2
	28.4	-91.4	54.0	20	CAT4
	29	-91.9	41.1	20	CAT2
Rita '05	24.3	-85.9	61.7	28	CAT4
	24.9	-88	77.1	19	CAT5
	25.4	-88.7	72.0	19	CAT5
	26.8	-91	59.1	37	CAT4
	27.4	-91.9	59.1	37	CAT4

Table 2.2.: Number of data shown in Figure 2.3.a that fall into different ranges of R/R_{max}.

***R/R_{max}* range**	***No. of data points***
0-1.5	3586
1.5-3	8772
3-4.5	11025
4.5-6	9250
6-7.5	6626
7.5-9	4027
9-10.5	2272
10.5-12	1273
12-19	1652

Figures 2.3.c and 2.3.d show the moving average and standard deviation of the ratios in Figures 2.3.a and 2.3.b, using a window of 2000 points. Except for a small region close to the core ($R < 1.5R_{max}$), the local average in Figure 2.3.c fluctuates around 1. This means that on average the MSR model generates unbiased rainfall profiles for radial distances up to $15R_{max}$ from the TC center. For distances $R < 1.5\ R_{max}$ the MSR model tends to overpredict the PR rainrates.

As noted above, the large local standard deviations in Figure 2.3.c reflect the significant small-scale variability of TC rainfall. It is interesting that the standard deviation tends to increase as the distance from the TC center increases. This is in accordance with the findings of other studies (Jorgensen, 1984a; Powell, 1990, and Molinari *et al.*, 1994) that the outer TC environment exhibits more cellular structure and higher small-scale variability relative to the inner region.

Figure 2.3.d shows that for radial distances up to $8R_{max}$ the MSR model tends to underpredict the MM5 rainfall intensities by about 50%, whereas for larger distances the opposite is true. Since the MSR model displays good skills in reproducing the PR rain rates, it is possible that these differences reflect MM5 biases. This is consistent with what other studies have found when comparing MM5 rainfall estimates to empirical and radar observations; see e.g. Fall *et al.* (2007), Juneng *et al.* (2007), Chen *et al.* (2007) and Rogers *et al.* (2007). The higher standard deviations in Figure 2.3.d compared to Figure 2.3.c further suggest that MM5 may enhance local convective activity. One should however caution that these observations are based on just one simulated hurricane and should be validated through a more extensive comparison.

2.5 Asymmetry of the Rainfall Field

In the case of a moving TC, equation (2.4) becomes

$$i(R,\theta) = \begin{cases} \alpha(\bar{T})\, \bar{Q}\, W_H(R,\theta) \;, & W_H(R,\theta) > 0 \\ 0 \;, & W_H(R,\theta) \leq 0 \end{cases} \tag{2.8}$$

where the vertical wind speed W_H depends on both R and θ and is given by equation (2.2) for $Z = H$. In this asymmetric case the rainfall intensities from equation (2.8) must be corrected both radially using equations (2.6) and (2.7) and azimuthally to account for the redistribution of rainwater due to cyclonic circulation; on the latter, see Corbosiero and Molinari (2002), Black *et al.* (2002) and Rogers *et al.* (2003).

To keep the correction simple, we perform the azimuthal redistribution uniformly within an angular interval $[\theta, \theta+\Delta\theta]$ where $\Delta\theta$ is given by

$$\Delta\theta = \frac{V_{gr}(R)}{R}\,(t_f + t_r) \tag{2.9}$$

The angle $\Delta\theta$ is in radians (positive clockwise in the Northern hemisphere), V_{gr} is the tangential wind velocity at gradient level [equation (2.1)], $t_f \approx 30$min is the time needed for rain generating features like convective cells to develop (Weisman and Klemp, 1986; Rogers and Yau, 1996) and t_r is the time needed for a raindrop at height H to reach the ground. A rough estimate of t_r comes from assuming an average raindrop velocity of 2-3m/s and a boundary layer depth $H \approx$ 2.5-3km. This gives $t_r \approx 25$min.

Next we use equations (2.8) and (2.9) for $t_f + t_r = 60$min to assess the effect of motion on the spatial variation of TC rainfall and propose a motion-based, rather than shear-based, parameterization of rainfall asymmetry.

2.5.1 Motion-based versus shear-based parameterization of rainfall asymmetry

MSR is a boundary layer model that generates spatial rainfall without explicitly considering vertical shear S. Rather, rainfall asymmetries are linked to storm motion. Since most of the rainfall originates at low altitudes relative to those that define wind shear, one may expect this to be a suitable approach.

To verify this assertion, Figure 2.4 compares the shear-aligned rainfall asymmetry from TRMM with the motion-aligned rainfall asymmetry from MSR. In both cases, asymmetry is defined as

$$A(R,\theta) = \frac{i(R,\theta) - i_{sym}(R)}{i_{sym}(R)} \tag{2.10}$$

where $i(R,\theta)$ is rainfall intensity at (R,θ) and $i_{sym}(R)$ is the azimuthal average. More specifically, Figure 2.4.a shows the average of the rainfall asymmetries in Figure 7 of Chen *et al.* (2006) over all TC-intensities and shear magnitudes after aligning the shear vector to point North. For shear we have used the distribution in Figure 6 of the same study, whereas for TC intensity we have used the discrete distribution in Table 1 of Lonfat *et al.* (2004).

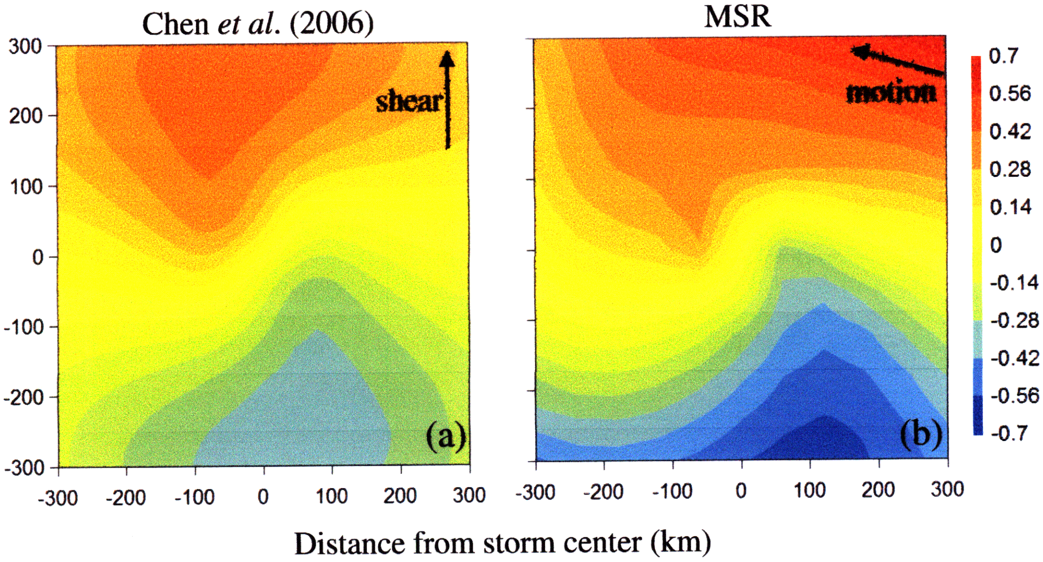

Figure 2.4: Comparison of rainfall asymmetry from TRMM and the MSR model. (a) Ensemble average of rainfall asymmetries in Figure 7 of Chen *et al.* (2006) over all TC intensities and shear magnitudes. (b) Ensemble average of rainfall asymmetries from MSR over all TC intensities and translation velocities. In (b), the TC moves in the Northern hemisphere at an angle 75° to the west of the shear vector in (a).

Similarly, Figure 2.4.b was generated by averaging rainfall asymmetries from the MSR model over a range of TC intensities and translation velocities. Storms are assumed to move in the Northern hemisphere at an angle of 75° west of the shear-direction in Figure 2.4.a. This is the average angle between shear and motion from Figures 3 and 12 of Chen *et al.* (2006) and is in the range reported by Corbosiero and Molinari (2003). For storm intensity we have used the same discrete distribution as in Figure 2.4.a, setting V_{max} = 30m/s for tropical storms, V_{max} = 42m/s for CAT12 and V_{max} = 60m/s for CAT35 systems. The distribution of the translation velocity was taken from Figure 11 of Chen *et al.* (2006). All other storm parameters have been kept constant, with values $f = 4.7\ 10^{-5}$ sec^{-1}, $R_{max} = 40$km, $B = 1$, $\bar{T} = 22^{\circ}$C, $\bar{Q} = 0.8$, $K = 50$m^2/s, and $C_D = 0.002$.

One sees that the two asymmetries are very similar in both pattern and magnitude, validating the contention that for rainfall risk one can use the MSR model with motion as the driver of asymmetry. Differences between Figures 2.4.a and 2.4.b occur mainly far away from the core ($R > 250$km), but these differences are statistically not significant and inconsequential for risk analysis.

2.6 Sensitivity Analysis

Figures 2.5 and 2.6 show the sensitivity of the MSR model results to various tropical cyclone characteristics: the tangential wind speed under gradient balance [parameterized by V_{max}, R_{max} and B; see equation (2.1)], the vertical diffusion coefficient K, the surface drag coefficient C_D, the depth-averaged temperature $\bar{T}$ inside the BL and the translation velocity V_t of the storm. Since rainfall intensity is proportional to the depth-averaged saturation ratio $\bar{Q}$ [see equations (2.4) and (2.8)], dependence on $\bar{Q}$ is not illustrated.

Figure 2.5 shows the sensitivity of the azimuthally averaged rainfall intensity i_{sym} to V_{max}, R_{max}, B, K, C_D and $\bar{T}$. Parameters are varied one at a time around the base-case values $V_{max} = 50$m/s, $R_{max} = 40$km, $B = 1$, $K = 50$m^2/s, $C_D = 0.002$, $\bar{T} = 22^{\circ}$C and $\bar{Q} = 0.8$ (solid lines). The figure shows that the maximum tangential velocity V_{max} and the roughness of the surface boundary (expressed through C_D) have significant effects on rainfall intensity and that lower values of R_{max} produce rain rates that are more peaked and more concentrated near the TC center.

Dependence of the azimuthally averaged rainrate i_{sym} on V_{max} of the type produced by the model has been observed in TC rainfall data (Lonfat *et al.*, 2004, Tuleya *et al.*, 2007; see Introduction). For example, the expressions used by the R-CLIPER parameterization (Tuleya *et al.*, 2007) indicate that when V_{max} increases from 50 to 70m/s, the maximum rainrate increases by a factor of about 1.5. This is also what the MSR model predicts. However, to our knowledge the effect of C_D and R_{max} on i_{sym} have not been isolated from data. The effect of surface roughness can be qualitatively assessed using the finding in Trenberth *et al.* (2007) that low-level horizontal wind convergence is by far the dominant factor for TC rainfall. Hence, if one considers that low-level convergence increases with increasing surface drag (see Chapter 1), one concludes that higher surface drag coefficients should cause TC rainfall to intensify.

The B parameter has a small effect on the peak rainfall intensity, but influences significantly the rate at which rainfall decays with radial distance (higher values of B resulting in faster decay). The azimuthally averaged rainfall intensity i_{sym} has small sensitivity to temperature $\bar{T}$ and the vertical diffusion coefficient K. Consequently, setting those parameters to constant values (e.g. to $\bar{T} = 22°C$ and $K = 50m^2/s$, as was done in Sections 2.3-2.5) does not induce large errors.

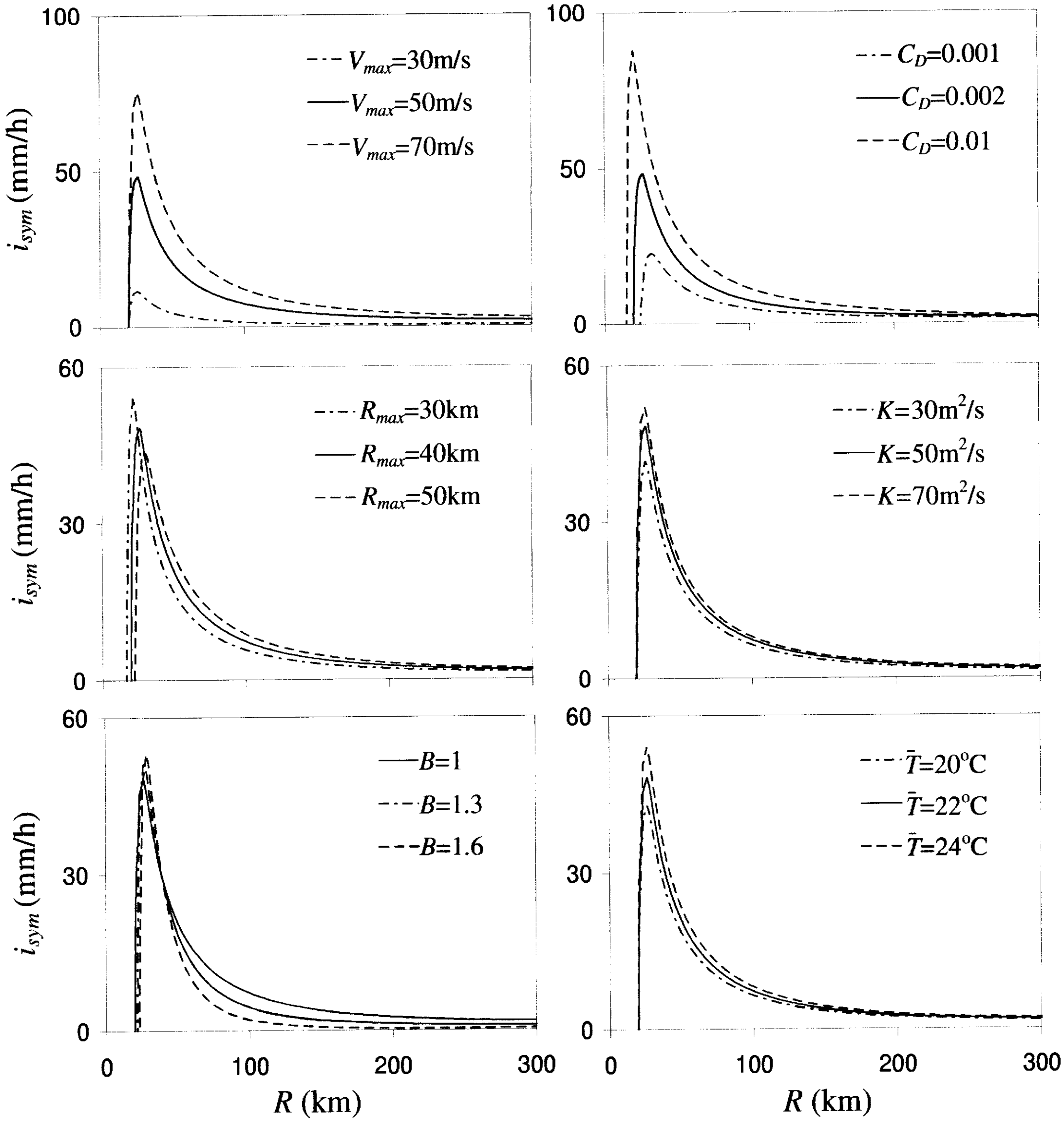

Figure 2.5: Sensitivity of the azimuthally averaged MSR rainfall profiles. Solid lines correspond to $V_{max} = 50m/s$, $R_{max} = 40km$, $B = 1$, $C_D = 0.002$, $K = 50m^2/s$, $\bar{T} = 22°C$ and $\bar{Q} = 0.8$. Each panel shows results under perturbation of one parameter.

Figure 2.6 shows the effect of the drag coefficient C_D and translation velocity V_t on rainfall asymmetry for a TC that translates northward in the Northern hemisphere. All other parameters are the same as for the base case in Figure 2.5. As expected and in accordance with findings in Lonfat *et al.* (2004), the asymmetry increases as V_t increases. The effect of C_D is more complex: at the front of the storm, rainfall asymmetry is insensitive to C_D, whereas at the rear-right the rainfall asymmetry increases with decreasing C_D.

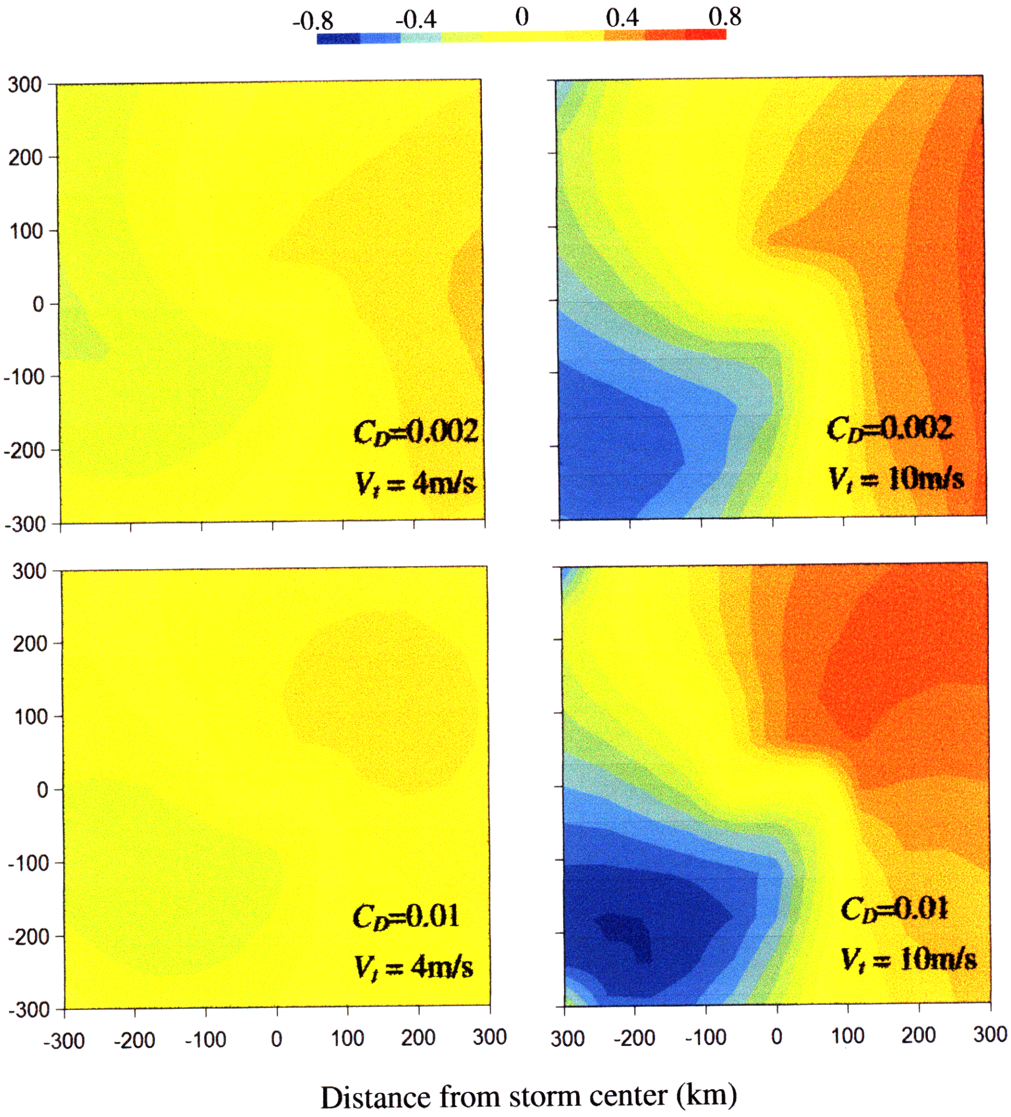

Figure 2.6: Sensitivity of MSR rainfall asymmetry to the drag coefficient C_D and the storm translation velocity V_t for a tropical cyclone that moves northward. All other parameters are the same as for the base case in Figure 2.5.

2.7 Conclusions

We have developed a simple theoretical model for the large-scale rainfall intensity field generated by translating tropical cyclones (TCs). The model assumes that, with corrections for sloping updrafts and azimuthal redistribution, the upward water vapor flux originated from the boundary layer is a good predictor of rainfall intensity. Vertical moisture fluxes are calculated using elementary thermodynamic principles in combination with a boundary layer model that extends Smith's (1968) analysis to moving storms.

The proposed modified-Smith-for-rainfall (MSR) model estimates the rainfall field from a given radial profile of the tangential wind speed at gradient level, the translation velocity V_t of the storm, the surface drag coefficient C_D, and the average temperature $\bar{T}$ and saturation ratio $\bar{Q}$ inside the TC boundary layer. Model predictions are compared to MM5 simulations and R-CLIPER estimates and validated through precipitation radar (PR) rainfall products from TRMM. The MSR model displays good skills in reproducing the shape and magnitude of PR rainfall fields. We have also verified that the asymmetries produced by storm motion are close to those observed and often parameterized in terms of vertical wind shear. In a parametric analysis, we have studied how the model predictions depend on various storm characteristics.

The combination of a rich parameterization and computational efficiency makes the present model an attractive instrument for risk applications, where one must assess tropical cyclone rainfall under many storm and environmental scenarios. For the latter purpose one needs tools with computational times on the order of minutes. This constraint effectively rules out the use of full-physics high-resolution numerical weather prediction models. An important limitation of the MSR model relative to high-resolution schemes is that it does not account for local rainfall intensifications due to rainbands and local convection. In Chapter 3 we model those intensifications by adding a stochastic component to the MSR model predictions. Another limitation of the MSR model is that it does not account for after-landfall conditions and therefore is applicable only to open-water or near-water sites. Extension of the model to inland conditions should be pursued in the future.

3. Long-Term Rainfall Risk from Tropical Cyclones in Coastal Areas

3.1 Introduction

The quantification of long-term rainfall risk is a basic problem of stochastic hydrology (e.g. Chow *et al.*, 1988; Singh, 1992). Our specific interest is in the risk of extreme rainfall posed at coastal sites by tropical cyclones (TCs). These events are relatively rare, but in combination with wind, surge and waves, high rainfall intensities may have devastating consequences (Herbert *et al.*, 1997; Rappaport, 2000).

For ordinary rainfall, standard risk analysis techniques use historical annual-maximum data (e.g. Koutsoyiannis *et al.*, 1998) or peak-over-threshold (PoT) information (e.g. Madsen *et al.*, 1997). The episodic and spatially localized nature of tropical cyclones prevents one from using these standard techniques. For example, the annual maximum and PoT rainfall statistics due to tropical cyclones depend on whether the site is "hit" by one or more TCs in any one year and therefore are highly erratic. For this reason, the risk is best assessed parametrically, by combining a probabilistic model of the maximum rainfall due to a TC with given characteristics $\boldsymbol{\theta} = [\theta_1,\ldots,\theta_r]$ with the rate at which those events occur. For coastal sites, the vector $\boldsymbol{\theta}$ might include the intensity and size of the storm, the location and translational velocity at landfall, and possibly other parameters related to atmospheric conditions, the radial profile of the tangential winds, etc. Parametric approaches of this type have been used to assess the risk posed by tropical cyclones for wind, surge and waves (Myers, 1975; Ho and Myers, 1975; Ho *et al.*, 1987; Powell *et al.*, 2005; IPET, 2006, 2008), but not rain. Our objective is to fill this gap.

The main problem for rainfall is to evaluate the extreme precipitation intensities caused by a TC with given characteristics $\boldsymbol{\theta}$. The historical data are too sparse and the potentially important TC parameters are too many to infer such extreme rainfalls from empirical observations alone. For example, current empirical approaches (Lonfat *et al.*, 2004, 2007; Tuleya *et al.*, 2007) classify storms into three coarse intensity categories and use microwave imager (TMI) data from TRMM (Simpson *et al.* 1988) to calculate the ensemble-average rainrate for each category as a function of distance from the TC center.

The alternative we pursue here is to use a physical model to assess the dependence of the mean rainfall field on $\boldsymbol{\theta}$ and statistical analysis to quantify the fluctuations of rainfall intensity around this mean field. The physical model is that developed in Chapters 1 and 2. In Chapter 1 we proposed a theoretical method to estimate the large-scale horizontal and vertical winds inside TCs (the vertical winds are largely responsible for rain). The model is an extension of Smith's (1968) formulation and is referred to here as the Modified Smith (MS) model. Characteristics of the TC that are explicitly considered by the model are the maximum tangential wind speed V_{max}, the radius of maximum winds R_{max}, the parameter B that controls the shape of the radial profile of the tangential wind speed (Holland, 1980), the storm translation velocity V_t, the surface drag coefficient C_D, and the vertical diffusion coefficient K. When $V_t = 0$, the wind field is symmetric around the storm center, whereas when the TC translates in the Northern (Southern) hemisphere the field is asymmetric, with stronger horizontal and vertical winds right-front (left-front) of the storm. The model does not resolve rainbands, local convection and turbulent phenomena and therefore produces smooth wind fields.

In Chapter 2 we extended the MS model to predict TC rain, assuming that the upward moisture flux at the top of the TC boundary layer is all converted into rainfall. The vertical moisture flux is evaluated from the vertical winds generated by the MS model and two additional parameters: the average temperature $\bar{T}$ and average saturation ratio $\bar{Q}$ inside the TC boundary layer. We call this the modified-Smith-for-rainfall (MSR) model. The MSR model should prove useful for climatologic studies, but for hazard analysis it has the limitation of ignoring the inter-storm and intra-storm variations of rainfall intensity. These variations are highly significant for the assessment of risk. For example, Lonfat *et al.* (2004) found that, also within a given TC strength category, the average of the positive rainfall intensity inside annular regions of 10km width may deviate from the median value by more than one order of magnitude.

Our main objectives are: (1) Extend the MSR model to obtain the probability distribution of the maximum rainfall intensity in a time interval of given duration D at a fixed geographical location during the passage of a tropical cyclone with given characteristics $\boldsymbol{\theta}$ and (2) Combine this maximum rainfall model with a TC recurrence model to quantify rainfall risk in the form of intensity-duration-frequency (IDF) curves. For the first objective, we consider a site A at some distance y to the right ($y < 0$) or left ($y > 0$) of the TC center, as shown in Figure 3.1. As the storm passes, the rainfall intensity at A fluctuates as a random process $I(t)$. Our interest is in $I_D(t)$, the moving average of $I(t)$ for an averaging duration D, and more specifically in the distribution of $I_{D,max}(y,\boldsymbol{\theta})$, the maximum of $I_D(t)$ during the storm.

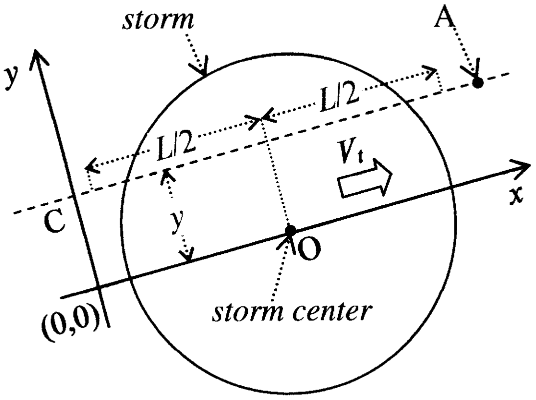

Figure 3.1: Schematic representation of a moving storm. Point O translates with the storm at speed V_t. Point A is the geographical location of interest.

Section 3.2 presents our general approach to calculate the distribution of $I_{D,max}(y,\boldsymbol{\theta})$. This distribution is obtained in Section 3.3 and validated in Section 3.4. Section 3.4 also shows how the distribution depends on various storm characteristics, the normalized distance y/R_{max} from the center of the storm, and the averaging duration D. Section 3.5 uses the model of $I_{D,max}(y,\boldsymbol{\theta})$ and a recurrence relation for hurricanes in the Gulf of Mexico to obtain IDF curves for New Orleans and compares these curves with published IDF values for all rainstorms (TCs and non-TCs) combined. Conclusions are stated in Section 3.6.

3.2 Framework for the Estimation of Extreme TC Rainfall

Our first objective is to relate the distribution of the maximum rainfall intensity $I_{D,max}(y,\boldsymbol{\theta})$ to the smooth rainfall intensities produced by the MSR model in Chapter 2. The storm parameters are $\boldsymbol{\theta} = [V_{max}, R_{max}, V_t]$. The analysis uses a Cartesian reference frame (x,y), translated and rotated such that the center of the storm O moves to the right along the x axis; see Figure 3.1. In this reference, the ordinate y of A is also the closest (signed) distance of A from the storm center.

To estimate this relationship, we use precipitation radar (PR) data from the TRMM mission (Simpson *et al.* 1988; Kummerow *et al.*, 1998; Lee *et al.*, 2002). These data are in the form of swaths about 200km wide with a spatial resolution of approximately 5 km and have been validated against ground-based radar and rain gauge measurements (Bolen and Chandrasekar, 2000; Liao *et al.*, 2001; Wolff *et al.*, 2005). Due to their long inter-frame time (about 12 hours), the PR snapshots cannot be interpolated to produce the rainfall intensities in continuous time that are needed to estimate rainfall maxima. A common way to overcome this limitation is to use Taylor's frozen turbulence hypothesis (Taylor, 1921, 1938). Under this hypothesis, the temporal variability of rainfall at a fixed location A is statistically the same as the variability that results from translating the frozen-in-time rainfield over A with the storm velocity V_t. For example, Vicente *et al.* (1998), Scofield and Kuligowski (2003), Kidder *et al.* (2005) and Ferraro *et al.* (2005) used Taylor's hypothesis to obtain rainfall totals at fixed locations from satellite and radar rainfall snapshots.

It follows from Taylor's hypothesis that $I_{D,max}(y,\boldsymbol{\theta})$ has the same distribution as $I_{l,max}(y,\boldsymbol{\theta})$, the maximum of the rainfall intensity averaged in a spatial window of length l along cross-section C in Figure 3.1, for $l = DV_t$. As an example, Figure 3.2 shows moving-average rainfall intensities from Hurricane Katrina (2005) along a cross-section at distance y = 100km from the storm center, for averaging lengths l = 6km (dashed line) and l = 24 km (solid line). The cross-section extends over L = 384 kilometers and is symmetrical relative to the storm center.

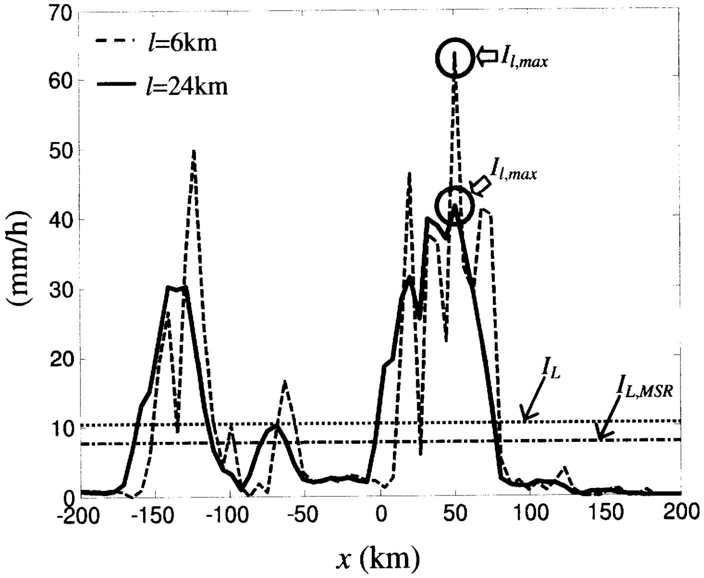

Figure 3.2: Rainfall intensities from Hurricane Katrina (Aug. 28, 2005, at 03:00UTC; TRMM frame 44361) along a cross-section C at distance y = 100km from the storm center, for spatial averaging scales l = 6 and 24 km. The maximum values $I_{l,max}$ are indicated by circles. I_L is the average value for the entire cross-section and $I_{L,MSR}$ is the estimate of I_L produced by the MSR model.

The intensity labeled I_L in Figure 3.2 is the average PR rainrate in L, whereas $I_{L,MSR}$ is the estimate of that average rainrate produced by the MSR model. These average intensities play an important role in our analysis. For any given $(y,\boldsymbol{\theta})$ combination, $I_{L,MSR}$ is a deterministic quantity, whereas I_L is regarded as a random variable with different values for different tropical cyclones. We model this storm-to-storm variability by expressing $I_L(y,\boldsymbol{\theta})$ as

$$I_L(y,\boldsymbol{\theta}) = I_{L,MSR}(y,\boldsymbol{\theta})\,\beta_L(y,\boldsymbol{\theta}) \tag{3.1}$$

where β_L is a random variable.

Figure 3.2 also shows significant amplification of the rainfall intensity when one considers the maximum over lengths $l < L$. One may express the maximum in l, $I_{l,max}$, as

$$I_{l,max}(y,\boldsymbol{\theta}) = I_{L,MSR}(y,\boldsymbol{\theta})\,\beta_{l,max}(y,\boldsymbol{\theta}) = I_{L,MSR}(y,\boldsymbol{\theta})\,\beta_L(y,\boldsymbol{\theta})\,\gamma_{l,max}(y,\boldsymbol{\theta}) \tag{3.2}$$

where the total factor relative to $I_{L,MSR}$, $\beta_{l,max}$, is the product of β_L in equation (3.1) and a random amplification factor $\gamma_{l,max}$ for the change of scale from L to l. The next section uses PR/TRMM data from 8 tropical cyclones (a total of 38 frames) to derive the distributions of β_L and $\gamma_{l,max}$. The selected frames (see Table 3.1) cover a wide range of TC intensities, from tropical storms to CAT5 systems, under pre-landfall conditions. This makes our model best suited for use in coastal areas. Due to the limited lateral coverage of the PR instrument, an additional requirement for selecting the frames was to cover regions close to the hurricane core (with radial distance less than 300km from the storm center), as these are the regions that are most critical for rainfall.

3.3 Distribution of β_L and $\gamma_{l,max}$

Equation (3.2) relates the maximum rainfall intensity in l to the average intensity in L produced by the MSR model using two random correction factors: a factor β_L to obtain the average rainfall in L, and a factor $\gamma_{l,max}$ to obtain the maximum average intensity at a smaller scale l. Sections 3.3.1 and 3.3.2 obtain the distribution of these factors using the rainfall information in Table 3.1 and MSR model simulations.

3.3.1 Distribution of β_L

The factor β_L is given by

$$\beta_L(y,\boldsymbol{\theta}) = \frac{I_L(y,\boldsymbol{\theta})}{I_{L,MSR}(y,\boldsymbol{\theta})} \tag{3.3}$$

Its distribution generally depends on the distance y from the TC center and the vector $\boldsymbol{\theta} = [V_{max}, R_{max}, V_t]$ of storm characteristics, but as we show next, a simple parameterization in terms of the normalized distance $y' = |y/R_{max}|$ and the large-scale MSR rainfall intensity $I_{L,MSR}$ suffices. Of course, $I_{L,MSR}$ is itself a function of $\boldsymbol{\theta}$.

Table 3.1: Characteristics of the PR/TRMM rain frames used in the analysis. The direction of storm translation is relative to the East and is positive counter-clockwise. The estimates of V_{max} and R_{max} are from the extended best track record (M. DeMaria, 2008; personal communication).

	Storm center		**Storm speed (m/s)**	**storm direction (deg)**	**V_{max} (m/s)**	**R_{max} (km)**	**TRMM frame number**	**Storm intensity**
	Lat. (deg)	**Lon. (deg)**						
Floyd '99	21.7	-61.6	4.9	143	48.8	41	10290	CAT2
	23.5	-68.7	4.8	169	64.0	37	10317	CAT4
	23.7	-70.6	5.8	171	69.3	37	10321	CAT4
Frances '04	12.6	-43.7	10.9	158	23.1	37	38646	TS
	15.7	-49.8	5.4	139	51.4	19	38667	CAT3
	17	-51.3	5.3	139	54.0	28	38677	CAT3
	17.9	-52.6	4.3	144	59.1	28	38682	CAT4
	19	-57.3	4.9	180	51.4	28	38708	CAT3
	21.2	-68.5	6.1	162	61.7	28	38739	CAT4
Ivan '04	8.9	-38.9	7.6	184	25.7	37	38789	TS
	10.7	-50.6	12.2	185	57.5	28	38814	CAT4
	11.2	-53.4	8.1	173	51.4	28	38820	CAT3
	12.3	-64.1	8.3	166	61.7	19	38845	CAT4
	12.7	-66.2	7.3	164	61.7	20	38851	CAT4
	17.4	-77.3	4.1	194	66.8	28	38892	CAT4
	17.7	-78.4	4.4	153	64.3	28	38897	CAT4
	25.6	-87.4	5.5	112	61.7	46	38954	CAT4
Jeanne '04	27.4	-70.6	5.5	0	38.6	42	39045	CAT1
	25.5	-69.5	1.1	207	41.1	37	39079	CAT2
	26.5	-74.3	7.4	173	43.7	60	39106	CAT2
	26.5	-75.6	6.5	180	46.3	46	39110	CAT2
Karl '04	11.5	-35.3	7.1	176	26.7	37	38987	TS
	17.3	-45.5	2.0	166	57.8	32	39033	CAT3
	19.1	-47.4	5.9	121	64.0	32	39048	CAT4
	22.9	-48.6	8.2	112	54.0	28	39059	CAT3
	25.7	-49.5	6.8	117	48.8	28	39063	CAT3
Katrina '05	24.6	-85.6	2.1	153	51.5	56	44357	CAT3
	25	-86.2	3.5	146	56.5	50	44361	CAT3
	26.9	-89	5.5	135	75.0	38	44373	CAT5
Lilli '02	23.6	-87.2	9.0	162	51.5	20	27826	CAT2
	24.4	-88.4	6.2	141	56.5	20	27830	CAT2
	28.4	-91.4	10.1	117	54.0	20	27842	CAT4
	29	-91.9	5.4	124	41.1	20	27845	CAT2
Rita '05	24.3	-85.9	5.7	189	61.7	28	44743	CAT4
	24.9	-88	3.9	166	77.1	19	44754	CAT5
	25.4	-88.7	4.3	153	72.0	19	44758	CAT5
	26.8	-91	5.5	135	59.1	37	44770	CAT4
	27.4	-91.9	4.8	143	59.1	37	44773	CAT4

Figure 3.3 shows statistics of β_L as a function of y' and $I_{L,MSR}$ for the TRMM frames in Table 3.1. The MSR intensities $I_{L,MSR}$ where obtained using the values of V_{max}, R_{max}, and V_t in the

extended best track record (M. DeMaria, 2008; personal communication; Demuth *et al.*, 2006). In addition, the MSR model requires the vertical diffusion coefficient K, the surface drag coefficient C_D, the vertically averaged temperature $\bar{T}$ and saturation ratio $\bar{Q}$ inside the boundary layer (BL), Holland's B parameter for the profile of gradient winds, the sloping angle ψ_0 and height H_0 of the wall updraft, and the temporal scale t_r for azimuthal re-distribution of rainfall by the cyclonic circulation; see Chapter 2 for details. In our simulations we have set $K = 50\text{m}^2/\text{s}$, $C_D = 0.002$, $\bar{T} = 22^\circ\text{C}$, $\bar{Q} = 0.8$, $B = 1$, $\psi_0 = 50^\circ$, $H_0 = 6\text{km}$ and $t_r = 60\text{min}$. In Chapter 2 we recommend these settings as representative of tropical cyclones in the North Atlantic and as values that reproduce well the TRMM/PR rainfall fields in an ensemble-average sense.

Figures 3.3.a and 3.3.b show smooth contour plots of the log-mean $m_{\ln\beta_L}$ and log-standard deviation $\sigma_{\ln\beta_L}$ of β_L as a function of the normalized distance $y' = |y/R_{max}|$ and the rainfall intensity $I_{L,MSR}$ for the 38 frames in Table 3.1. For each frame, a regular spacing $\Delta y = 10\text{km}$ was maintained between adjacent transects, producing a total of 789 points; see Figure 3.3.a. In all cases, averaging is over segments of length $L = 384\text{km}$, symmetric relative to the storm center. This value of L encompasses more than 95% of the total rainfall volume along each transect; see for example Figure 3.2. Smooth estimates of the mean value and variance of $\ln\beta_L$ were obtained using an isotropic Gaussian kernel with standard deviation 0.5 in the $[\ln(I_{L,MSR}), \ln(y')]$-plane. Hence, if $g(\mathbf{x})$ denotes this kernel, local estimates of $m_{\ln\beta_L}(\mathbf{x}_0)$ and $\sigma^2_{\ln\beta_L}(\mathbf{x}_0)$ around a given point $\mathbf{x}_0 = [\ln(I_{L,MSR}), \ln(y')]$ are given by

$$m_{\ln\beta_L}(\mathbf{x}_0) = \frac{\sum_i \ln\beta_L(\mathbf{x}_i)\, g(\mathbf{x}_i-\mathbf{x}_0)}{\sum_i g(\mathbf{x}_i-\mathbf{x}_0)}\,, \qquad \sigma^2_{\ln\beta_L}(\mathbf{x}_0) = \frac{\sum_i [\ln\beta_L(\mathbf{x}_i) - m_{\ln\beta_L}(\mathbf{x}_i)]^2\, g(\mathbf{x}_i-\mathbf{x}_0)}{\sum_i g(\mathbf{x}_i-\mathbf{x}_0)} \tag{3.4}$$

where $\mathbf{x}_i$ is the generic $[\ln(I_{L,MSR}), \ln(y')]$ combination for which a value of β_L is available. To use values of β_L at locations close to the center of the storm where $\ln(y')$ diverges, 59 points with $|y| < 0.5R_{max}$ where moved to $y = 0.5R_{max}$.

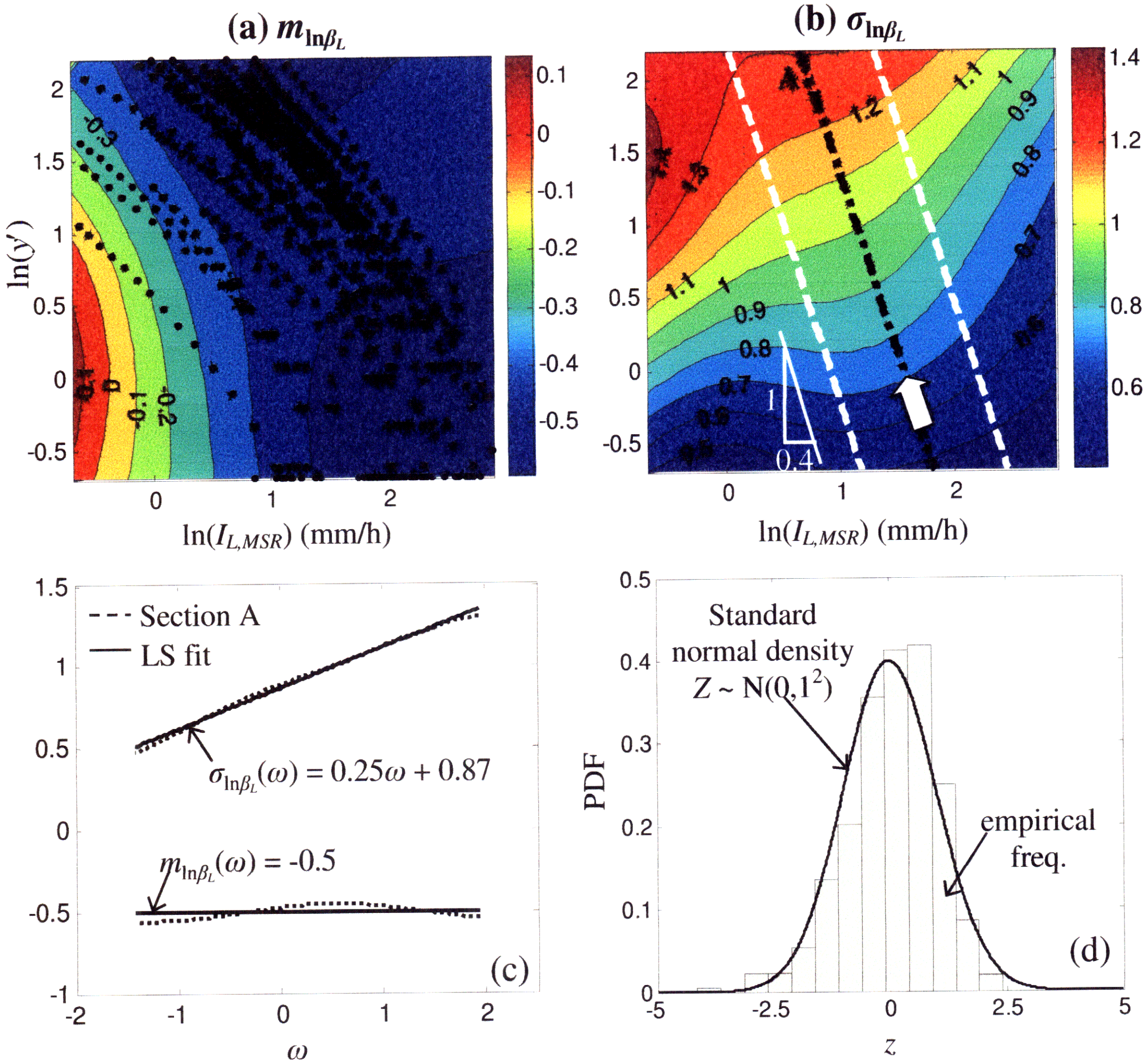

Figure 3.3: (a,b) Mean value and standard deviation of $\ln\beta_L$ as a function of the model rainfall intensity $I_{L,MSR}$ and the normalized distance $y' = |y/R_{max}|$ from the TC center using 789 cross-sections of the 38 frames in Table 3.1. The contour plots are obtained using a smoothing Gaussian kernel with standard deviation 0.5. The dashed lines delimit the region of high data density along the direction of the gradient of $\sigma_{\ln\beta_L}$ (white arrow). (c) Plots of $m_{\ln\beta_L}$ and $\sigma_{\ln\beta_L}$ as a function of $\omega = \ln(y') - 0.4\ln(I_{L,MSR})$ along cross-section A. (d) Comparison between the standard normal density and the empirical PDF of $\ln(\beta_L)$, normalized to have zero mean and unit variance.

The overall mean value of β_L is 1.02, indicating that on average the MSR model produces unbiased large-scale estimates of the PR rainrates. The dashed lines in Figure 3.3.b delimit the region of high data density and are generally oriented along the gradient of $\sigma_{\ln\beta_L}$. Figure 3.3.c shows plots of $m_{\ln\beta_L}$ and $\sigma_{\ln\beta_L}$ as a function of the transformed variable $\omega = \ln(y') - 0.4\ln(I_{L,MSR})$ along the dashed-dotted line in Figure 3.3.b. The log-mean $m_{\ln\beta_L}$ is approximately constant and equal to -0.5, whereas $\sigma_{\ln\beta_L}$ increases as the normalized distance y' increases or the large-scale mean rainfall intensity $I_{L,MSR}$ decreases. This higher log variability in regions of lower intensity is expected due to the more episodic nature of rainfall in those regions. This is also in qualitative agreement with the findings of Lonfat *et al.* (2004) and Molinari *et al.* (1994). The solid lines in Figure 3.3.c are least-squares fits for the mean and standard deviation of $\ln\beta_L$. For y close to zero, the fitted standard deviation becomes very small or negative. To avoid this inconsistency, we have imposed a lower bound of 0.5 to the fitted standard deviation.

To investigate the distribution type, we standardize the empirical values of $\ln\beta_L$ by removing the parametrically fitted mean -0.5 and dividing by the parametrically fitted standard deviation $0.25\omega + 0.87$. Figure 3.3.d shows a histogram of these normalized quantities and suggests that $\ln\beta_L$ has near-normal distribution. To check for possible lack of fit and possible dependence of $\ln\beta_L$ on other parameters, we generated histograms of the type in Figure 3.3.d separately for different ranges of y, y', $I_{L,MSR}$, R_{max} and V_{max}; see Figures 3.4 - 3.6.

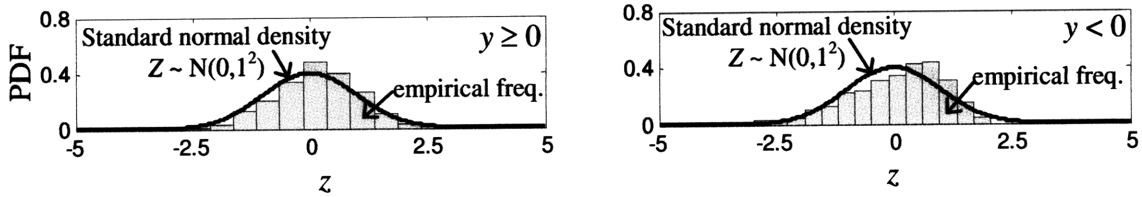

Figure 3.4: Comparison between a standard normal density (solid lines) and histograms of the normalized quantities in Figure 3.3.d when classified into two categories of positive and negative distances y from the center of the storm.

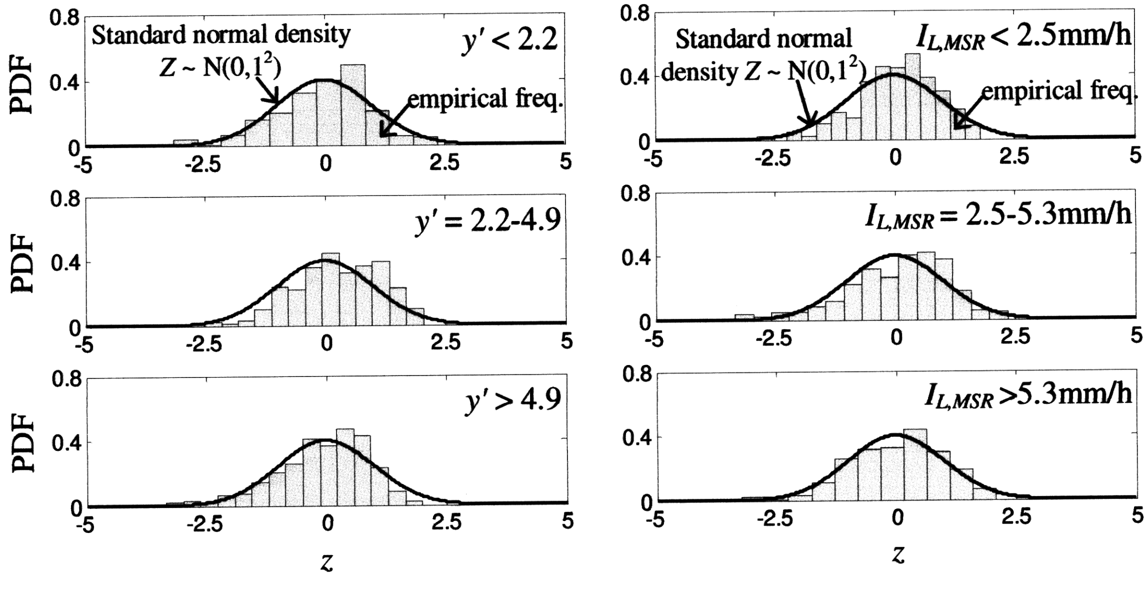

Figure 3.5: Comparison between a standard normal density (solid lines) and histograms of the quantities in Figure 3.3.d when classified into three equally sized bins of the normalized distance $y' = |y/R_{max}|$ (left column) and the theoretical large-scale rainfall intensity $I_{L,MSR}$ (right column).

As none of these analyses reveals significant dependence, we use the fits in Figure 3.3.c and model $\ln\beta_L$ as a normal variable with parameters

$$\begin{aligned} m_{\ln\beta_L}(\omega) &= -0.5 \\ \sigma_{\ln\beta_L}(\omega) &= \max\{0.5,\, 0.25\omega + 0.87\} \end{aligned} \tag{3.5}$$

where $\omega = \ln(y') - 0.4\ln(I_{L,MSR})$.

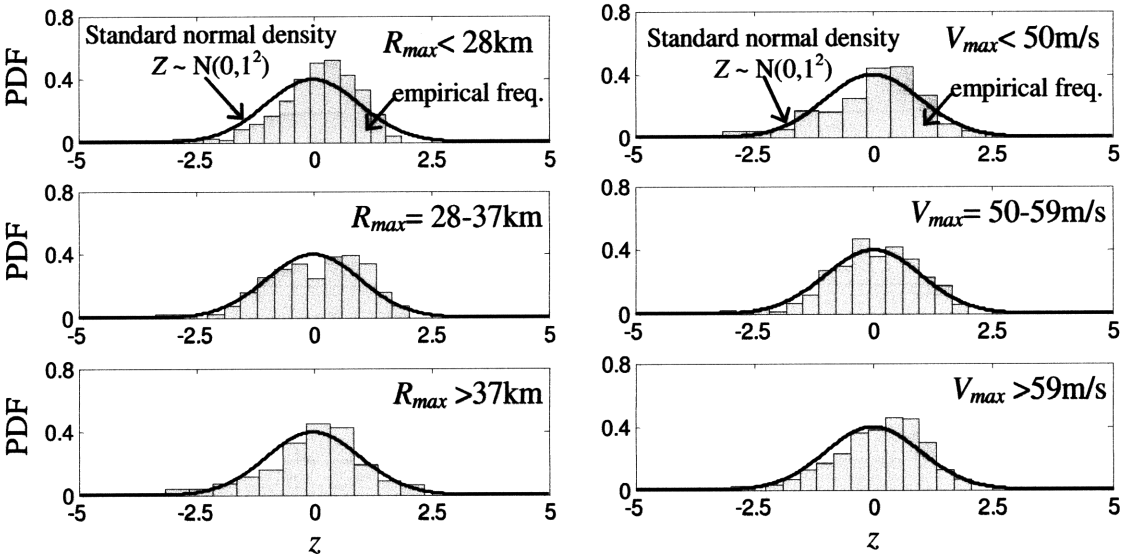

Figure 3.6: Same as Figure 3.5 but for different ranges of the radius of maximum winds R_{max} (left column) and the intensity V_{max} of the storm (right column).

3.3.2 Distribution of $\gamma_{l,max}$

Next we consider the amplification factor $\gamma_{l,max}$ in equation (3.2). The distribution of this factor can be found by a variety of methods, from the direct use of data on $\gamma_{l,max}$ from the frames in Table 3.1 to theoretical analysis of the maximum of the moving-average processes $I_l(x)$ illustrated in Figure 3.2. In Appendix B we compare several such approaches and find similar results. Here we follow the empirical approach, which is the simpler and more transparent method. We start by calculating the empirical ratio

$$\gamma_{l,max} = \frac{I_{l,max}}{I_L} \quad , \; l \le L \tag{3.6}$$

where I_L is the average PR rainrate along a cross section C of fixed length L = 384km and $I_{l,max}$ is the maximum rainfall intensity when the same cross section is continuously scanned using an averaging window of length l; see Figures 3.1 and 3.2 and Section 3.2. Ideally, the cross section

C should be in the direction of the storm motion, but since the TRMM swaths are not always aligned with that direction, we calculate the factor $\gamma_{l,max}$ using cross-sections parallel to the swath track. Hence, the resulting factor $\gamma_{l,max}$ does not depend on the orientation of C relative to the storm motion. We verified that $\gamma_{l,max}$ is insensitive to this orientation by dividing the swaths into two groups: those that are generally aligned with the storm trajectory and those that are not. The distribution of $\gamma_{l,max}$ is similar in the two cases.

We also studied the dependence of the distribution of $\gamma_{l,max}$ on R_{max}. Dependence is expected because smaller values of R_{max} produce more picked radial rainfall profiles and hence higher rainfall maxima. Figure 3.7 shows histograms of $\gamma_{l,max}$ as a function of the scale of spatial averaging l when classified into three equally sized bins of the radius of maximum winds R_{max}. One sees that for small spatial scales ($l \leq 12$km) the mean value and standard deviation of $\gamma_{l,max}$ increase somewhat with decreasing R_{max}, whereas at larger spatial scales the increase is modest. Based on these results, we ignore the dependence of $\gamma_{l,max}$ on R_{max} and use a simple parameterization in terms of the averaging length l and the large-scale average intensity I_L. The latter quantity depends significantly on both the storm intensity V_{max} and the distance y from the storm center; see Chapter 2.

Figure 3.8 shows log-log plots of $E[\gamma_{l,max}]$ and $\mathrm{Var}[\gamma_{l,max}]$ against l after classifying the 789 cross-sections in Figure 3.3.a into 12 equally-sized I_L bins. As expected, $\mathrm{Var}[\gamma_{l,max}]$ increases with decreasing spatial scale l. A less obvious finding is that the variability of $\gamma_{l,max}$ increases as the large-scale intensity I_L decreases. Considering that lower values of I_L are generally found at larger distances y from the storm center, Figure 3.8 shows that the outer TC environment exhibits higher (multiplicative) variability relative to the inner region. The higher variability inside low-I_L regions is due for the most part to an increase in the dry area fraction (see Appendix B) and has been noted also in other studies (Molinari *et al.*, 1994; Lonfat *et al.*, 2004). This feature is also commonly observed in extra-tropical rainfall (e.g. Over and Gupta, 1996; Deidda *et al.*, 2006; Veneziano *et al.*, 2006a; Gebremichael *et al.*, 2006).

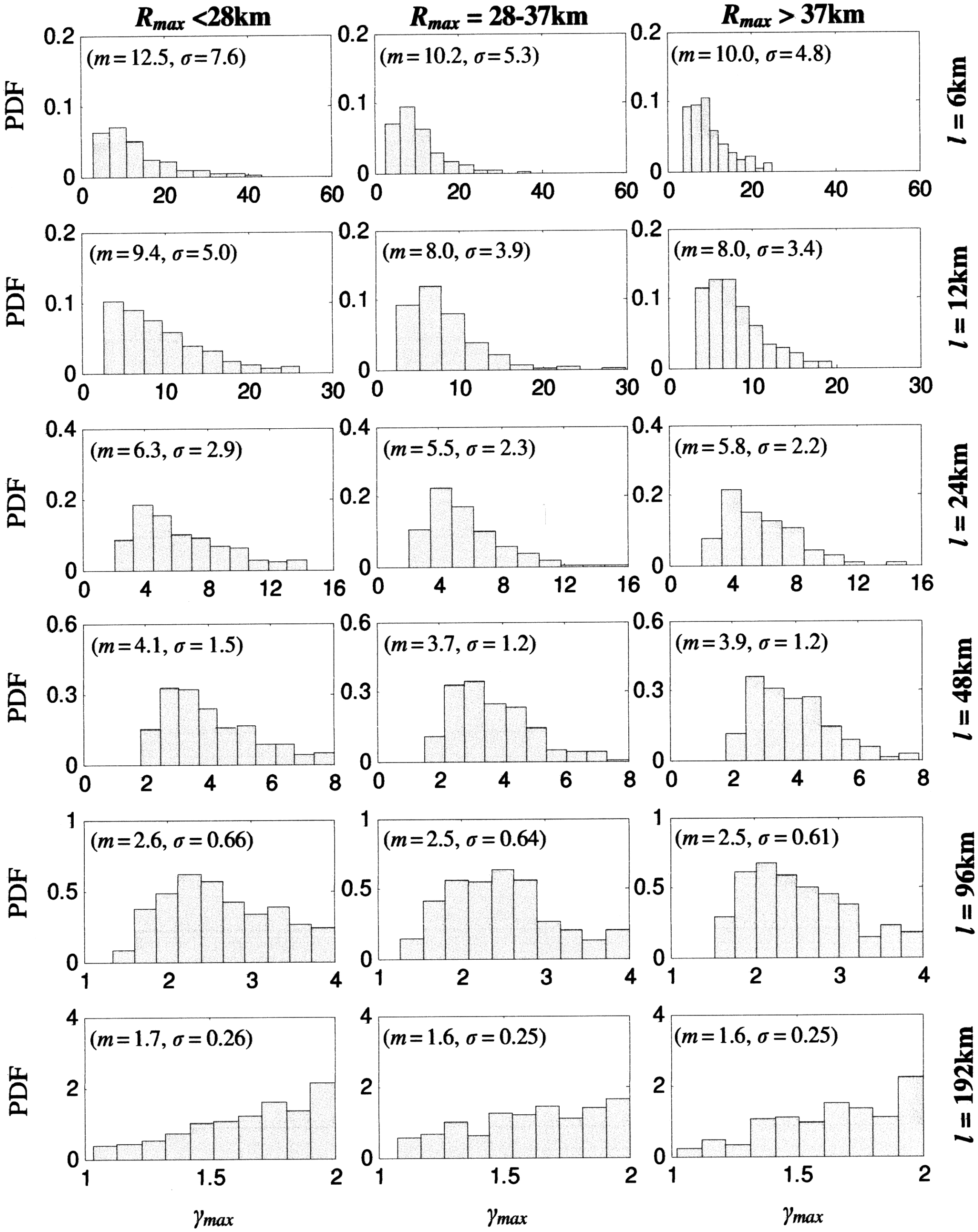

Figure 3.7: Empirical PDFs of $\gamma_{l,max}$ as a function of the scale of spatial averaging l when classified into three equally sized bins of the radius of maximum winds R_{max}. m and σ are the mean value and standard deviation of the empirical distributions.

For each intensity category I_L, we use least squares to fit linear and quadratic expressions for the log-mean and log-variance of $\gamma_{l,max}$,

$$\begin{aligned} \ln E[\gamma_{l,max}] &= a_1 \ln l + a_2 && \text{(a)} \\ \ln \mathrm{Var}[\gamma_{l,max}] &= a_3 (\ln l)^2 + a_4 \ln l + a_5 && \text{(b)} \end{aligned} \tag{3.7}$$

where $l \le L$ is in km and a_1-a_5 are parameters. Figure 3.9 shows how the parameters a_1-a_5 in equation (3.7) vary with the large-scale rainfall intensity I_L. The solid lines in Figure 3.9 are smooth least-squares estimates of a_i (i=1,...5). Use of the smooth estimates reproduces well the empirical moments of $\gamma_{l,max}$; see solid lines in Figure 3.8.

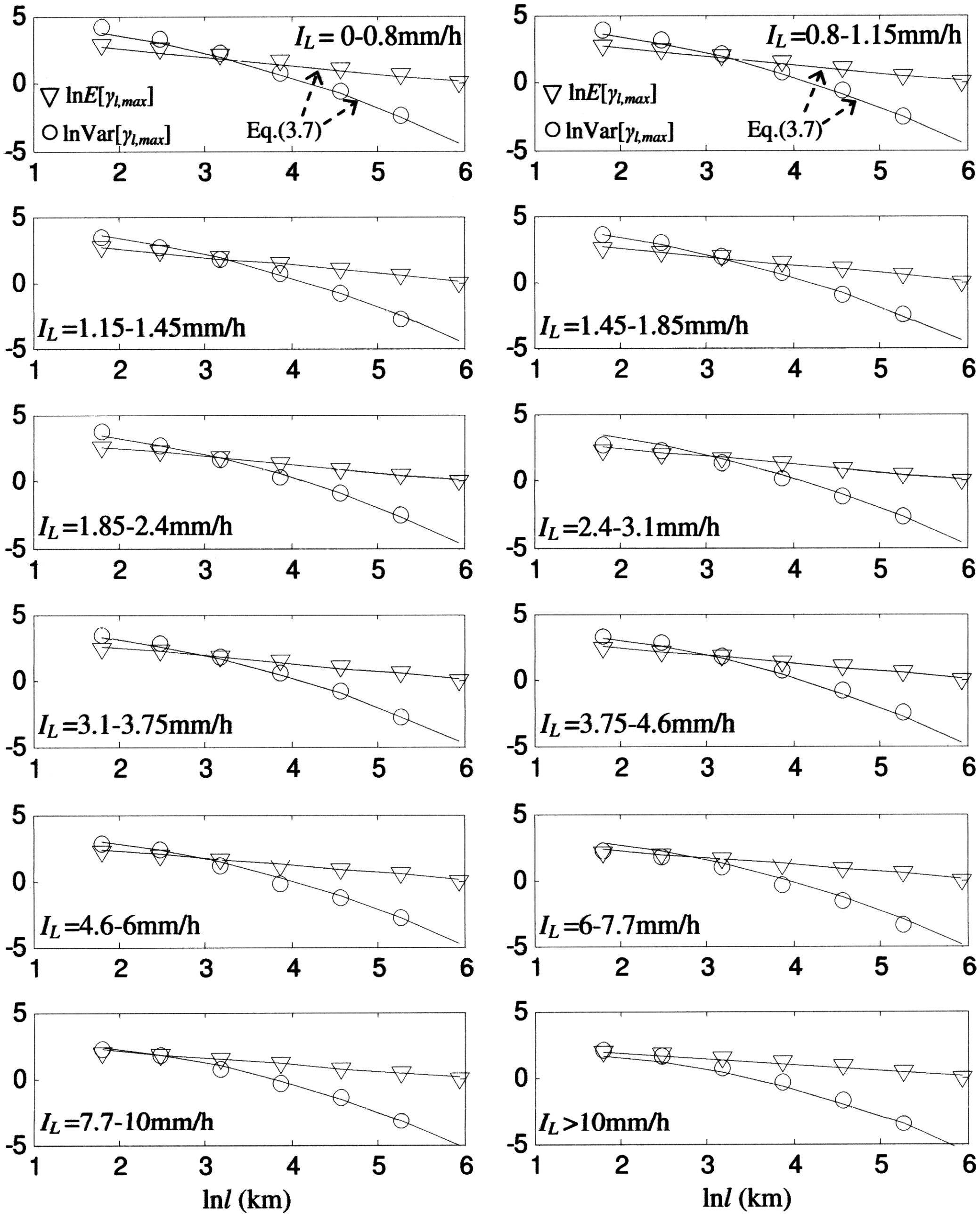

Figure 3.8: Log-log plots of $E[\gamma_{l,max}]$ and $\mathrm{Var}[\gamma_{l,max}]$ against l for different ranges of I_L. Triangles and circles indicate empirical values. The solid lines are from equation (3.7).

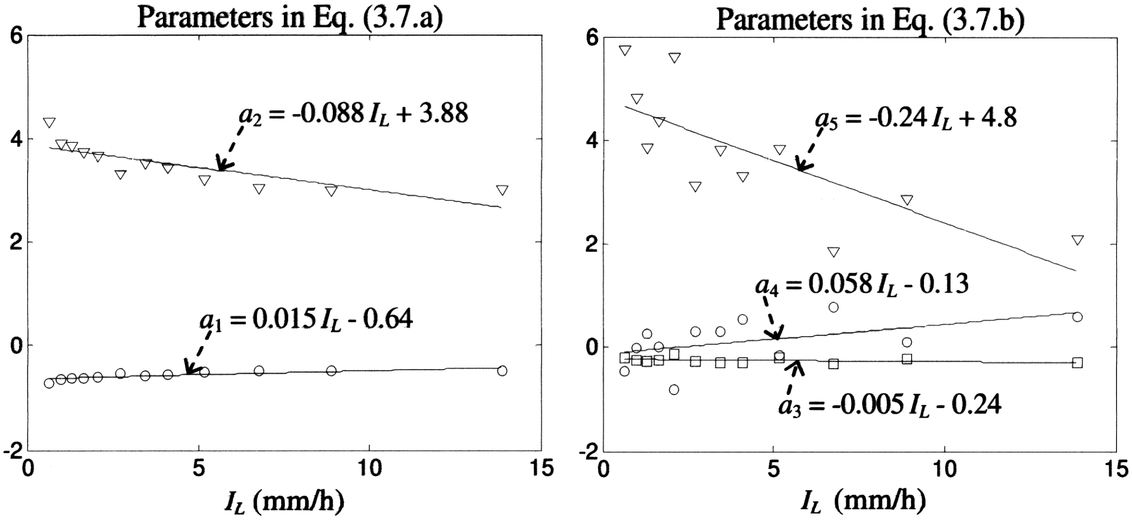

Figure 3.9: Dependence of the parameters a_1-a_5 in equation (3.7) on I_L. The solid lines are least squares fits.

The amplification factor $\gamma_{l,max}$ has values between 1 and L/l. The lower bound corresponds to a uniform distribution of rainfall inside L, whereas the upper bound is attained when all the rainfall in L is concentrated in a single l interval. We model $\gamma_{l,max}$ using a beta distribution with moments in equation (3.7). One may write this cumulative distribution as

$$F_{\gamma_{l,max}}(\gamma) = F_X\left(\frac{\gamma-1}{L/l-1}\right) \quad , \ \gamma \geq 1 \tag{3.8}$$

where F_X is the beta distribution in [0,1] with parameters

$$E[X] = \frac{E[\gamma_{l,max}]-1}{L/l-1} \quad , \ \mathrm{Var}[X] = \frac{\mathrm{Var}[\gamma_{l,max}]}{(L/l-1)^2} \tag{3.9}$$

Figure 3.10 compares the empirical distribution of $\gamma_{l,max}$ at spatial scales l = 96 and 6km for different large-scale average intensities I_L with theoretical distributions from equations (3.8) and (3.9). The moments $E[\gamma_{l,max}]$ and Var[$\gamma_{l,max}$] in equation (3.9) are calculated using equation (3.7) with parameters a_1-a_5 in Figure 3.9. Equally good fits are obtained for other window sizes l; see Appendix B.

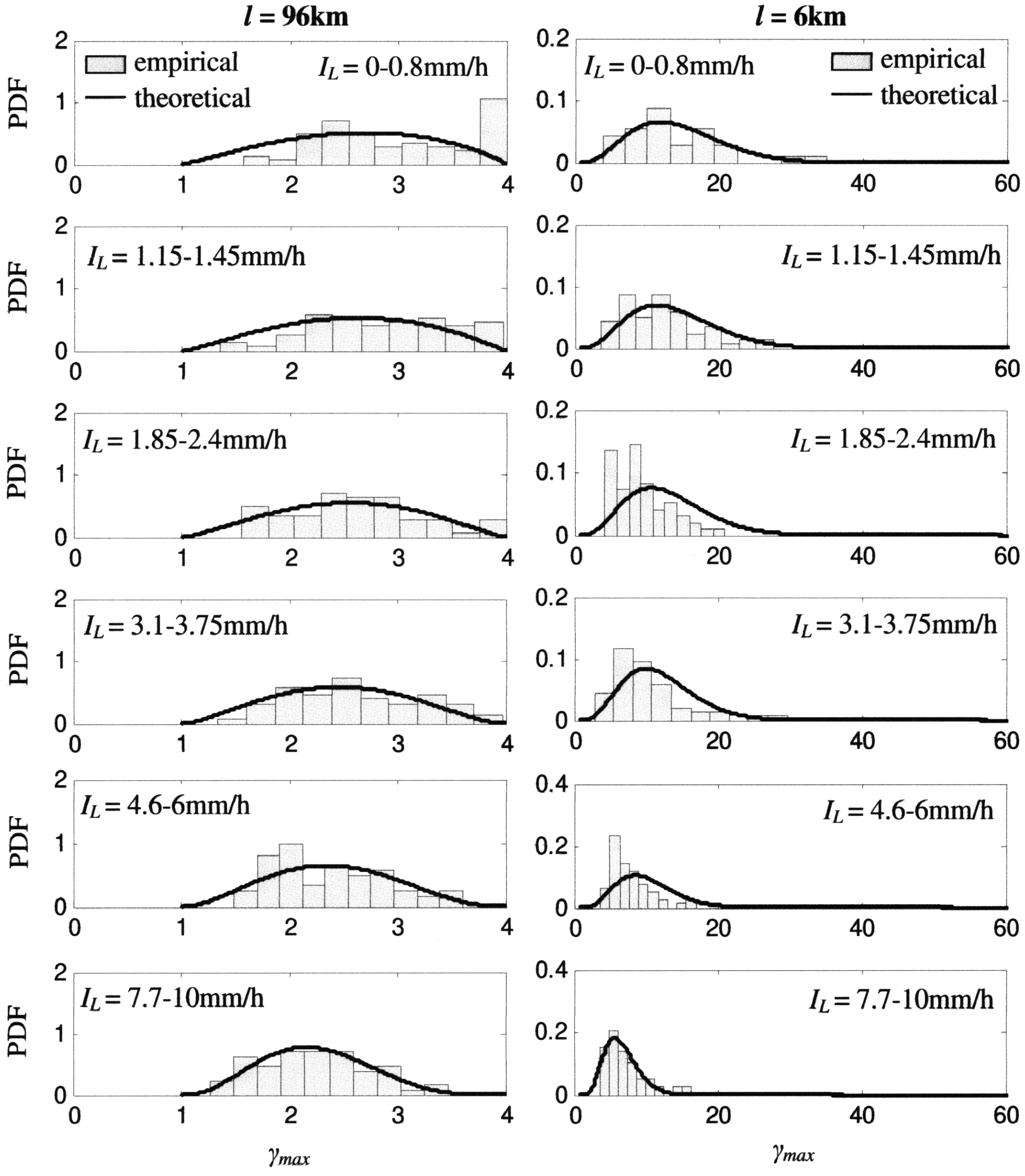

Figure 3.10: Comparison of histograms of $\gamma_{l,max}$ for l = 96 and 6 km and different large-scale intensities with theoretical distributions from equations (3.7) and (3.8). The intensity categories are the same as in the left column of Figure 3.8.

3.4 Validation of Maximum Rainfall Model and Sensitivity Analysis

For a tropical cyclone with parameters $\boldsymbol{\theta} = [V_{max}, R_{max}, V_t]$ and a given distance y from the storm center, one may use equation (3.2) and the distributions of β_L and $\gamma_{l,max}$ in Section 3.3 to obtain the distribution of the maximum rainfall intensity $I_{l,max}$ as

$$P[I_{l,max}(y,\boldsymbol{\theta}) \leq i] = \int_{0}^{\infty} f_{I_L|y,\boldsymbol{\theta}}(u)\, F_{\gamma_{l,max}|I_L=u}(i/u)\, du \tag{3.10}$$

where $f_{I_L|y,\boldsymbol{\theta}}$ is the probability density function of $I_L = I_{L,MSR}\,\beta_L$ given $(y,\boldsymbol{\theta})$ and $F_{\gamma_{l,max}|I_L}$ is the cumulative distribution function of $\gamma_{l,max}$ given I_L. To assess the validity of the theoretical probabilities generated by equation (3.10), we compare them with in-sample observed relative frequencies, as follows. For each of the 789 transects extracted from the PR data in Table 3.1,

1. We calculate the maximum intensity $I_{l,max}$ over segments of different length l;
2. We use (V_{max}, R_{max}, V_t) from Table 3.1 and the distance y of the transect from the TC center to obtain model estimates of the large-scale mean rainfall intensity $I_{L,MSR}(y,\boldsymbol{\theta})$ for L= 384km. All other MSR model parameters are fixed to the values in Section 3.3.1.
3. We use equation (3.10) and the parametric expressions in equations (3.5) and (3.7) and Figure 3.9 to find the distribution of $I_{l,max}$ and the probability P with which the observed value from step (1) is not exceeded.

If the model is correct, the probabilities P from step (3) should have uniform distribution between 0 and 1. Figure 3.11 shows histograms of P for different l. The fact that the histograms differ little from a uniform density validates the model in the sense that calculated exceedance probabilities are close to observed relative frequencies.

The distribution of $I_{l,max}$ in equation (3.10) depends critically on the amplification factor $\beta_{l,max}$ in equation (3.2). Figure 3.12 shows how the distribution of $\beta_{l,max}$ depends on l, V_{max}, and $y' = |y/R_{max}|$. The effect of the translation velocity V_t is modest and is not displayed. Also, for given V_{max} and $y' = |y/R_{max}|$, $\beta_{l,max}$ is insensitive to R_{max}. The dispersion of $\beta_{l,max}$ increases as l decreases. It also increases for smaller V_{max} and larger y'. The latter effects are related to the increased spatial variability of the rainfall intensity in regions of lower average precipitation.

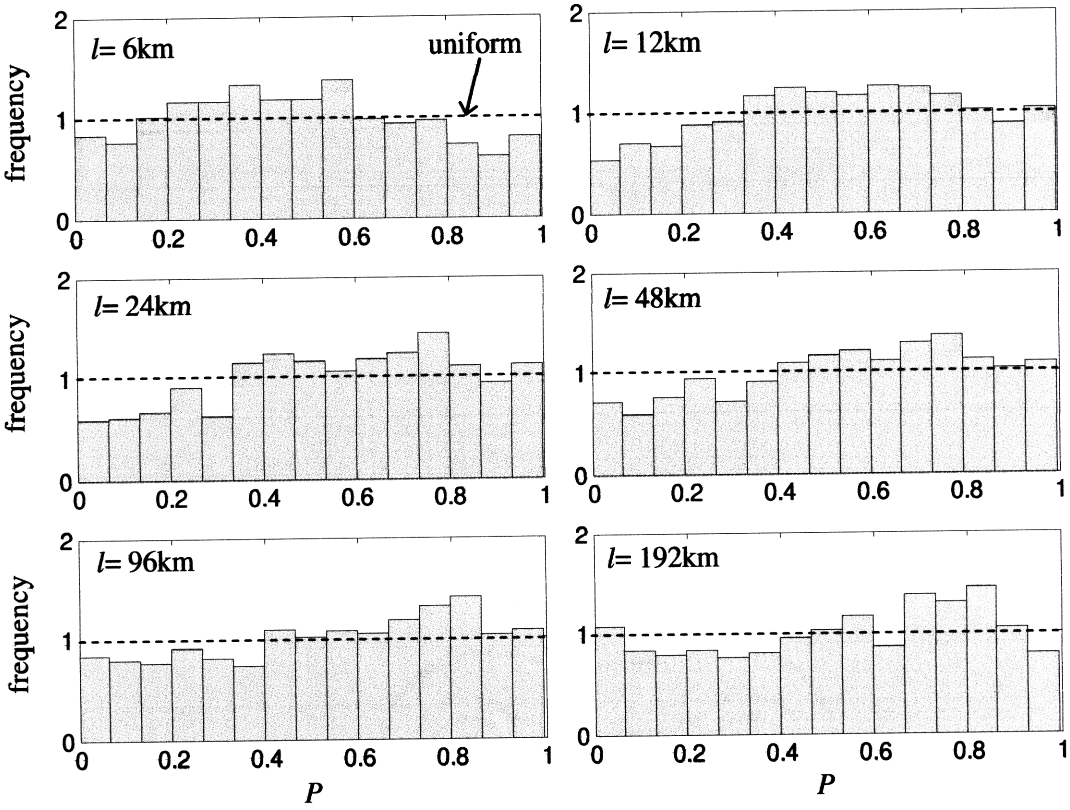

Figure 3.11: Histogram of the non-exceedance probability P in equation (3.10) for different spatial scales l. Each histogram is based on a sample of size 789.

3.5 Long-term Rainfall Risk for New Orleans

To assess rainfall risk at a given location A, one must find the rate $\lambda_{I_{D,max}} > i$ of tropical cyclones for which $I_{D,max}$, the maximum rainfall intensity at A for a given averaging duration D, exceeds different threshold levels i. This rate is given by

$$\lambda_{I_{D,max}} > i = \lambda \int_{\text{all } (y,\boldsymbol{\theta})} P[I_{D,max}(y,\boldsymbol{\theta}) > i]\, f_{y,\boldsymbol{\theta}}(y,\boldsymbol{\theta})\, dy\, d\boldsymbol{\theta} \tag{3.11}$$

where λ is the rate of TCs in the region, $P[I_{D,max}(y,\boldsymbol{\theta}) > i]$ is the probability that, for a storm with characteristics $\boldsymbol{\theta}$, $I_{D,max}$ at distance y from the storm center exceeds i, and $f_{y,\boldsymbol{\theta}}$ is the joint density of $(y,\boldsymbol{\theta})$. The joint density $f_{y,\boldsymbol{\theta}}$ and the rate λ are region-specific and define the TC recurrence model. Under Taylor's hypothesis, $P[I_{D,max}(y,\boldsymbol{\theta}) > i]$ is obtained by setting $l = DV_t$ in equation (3.10).

To exemplify, we use equation (3.11) and a recurrence model for an appropriate coastal region of the Gulf of Mexico to obtain intensity-duration-frequency (IDF) relationships for New

Orleans. We select this location because: 1) the site is close to the coast; hence our pre-landfall model should produce accurate results, 2) a number of studies have developed TC recurrence models for the Louisiana coast, and 3) one can compare the TC rainfall results with available IDF curves from continuous rainfall records in the region.

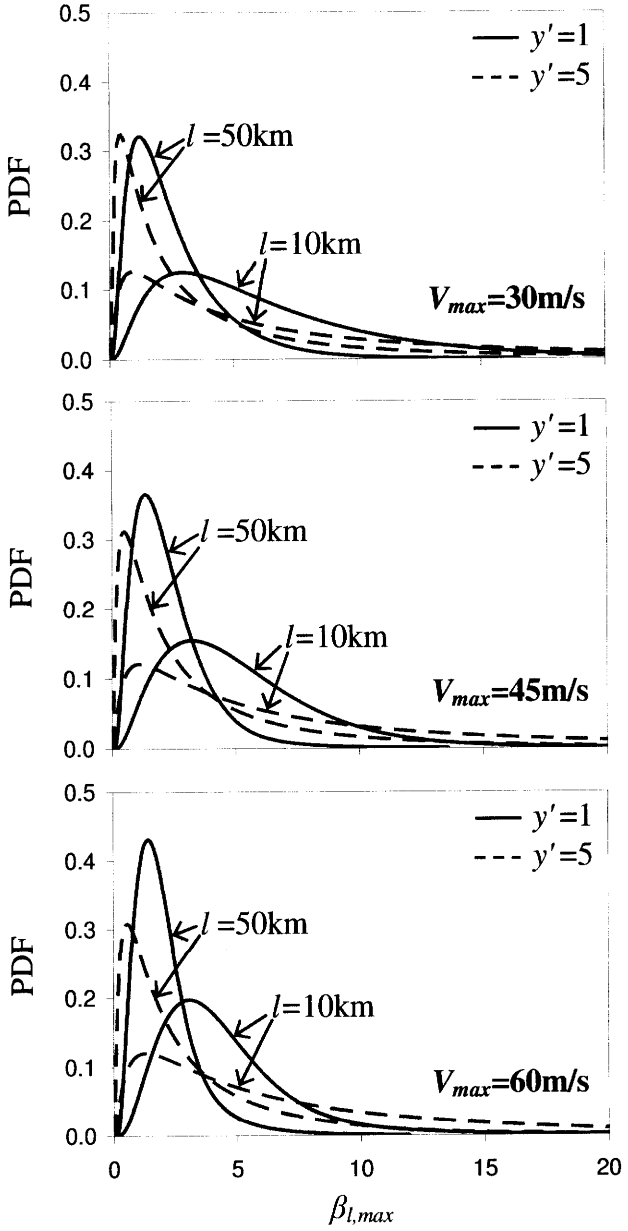

Figure 3.12: Comparison of the PDF of $\beta_{l,max}= I_{l,max}/I_{L,MSR}$ for different V_{max}, $y' = |y/R_{max}|$, and l.

3.5.1 TC recurrence model for the northern Gulf of Mexico

We start by specifying the distribution of the distance y between the center of the storm and the city of New Orleans (point A), which is located at approximately (90°W, 30°N). Then we consider the distribution of $\boldsymbol{\theta} = [V_{max}, R_{max}, V_t]$. The joint model for V_{max} and R_{max} is specified through the distribution of the maximum pressure deficit ΔP_{max} and the conditional distributions of $[V_{max}|\Delta P_{max}]$ and $[R_{max}|\Delta P_{max}]$. Finally we specify the TC rate λ. To keep the model simple, we approximate the coastline by a line segment with constant latitude 30°N and longitudinal range 85°-95°W (≈ 960km), centered at A.

Let z be the location (positive eastward) of landfall relative to A. Assuming a straight storm path, the closest distance of the storm center from the site is

$$y = -z\cos(\alpha) \tag{3.12}$$

where α is the azimuth of the storm track at landfall, positive clockwise. The distribution of y can be obtained numerically from equation (3.12) and the distributions of α and z, assumed here to be independent. For z we use a uniform distribution in the interval [85°W, 95°W]. The distribution of the angle α in the region is usually found to be normal or the mixture of two normal distributions, one for easterly storms and the other for westerly storms (Vickery and Twisdale, 1995; IPET, 2006, 2008). Here we model α using a single normal distribution with mean value $m_\alpha = -5.4^\circ$ and standard deviation $\sigma_\alpha = 34.9^\circ$. This distribution was obtained by IPET (2006) using NOAA's HURDAT data set (Jarvinen *et al.*, 1984) and found to describe well storms with central pressure deficit $\Delta P_{max} > 34$mb that make landfall in the longitudinal range 85°-95°W.

Several studies (Holland, 1980; Atkinson and Holiday, 1977; Willoughby and Rahn, 2004) have used theoretical arguments and pressure-wind observations to relate V_{max} to ΔP_{max}. The relationships are typically of the power-law type

$$V_{max} = c\,(\Delta P_{max})^g \tag{3.13}$$

where c and g are positive constants. Using flight level data from 23 hurricane seasons, Willoughby and Rahn (2004) found $c = 4.8$ and $g = 0.559$ for V_{max} in m/s and ΔP_{max} in mb. Based on these and other findings of Willoughby and Rahn (2004), we model $[V_{max}|\Delta P_{max}]$ as a lognormal variable with mean value $4.8(\Delta P_{max})^{0.559}$ and coefficient of variation 0.15.

Empirical evidence (Vickery and Twisdale, 1995; Vickery *et al.*, 2000; Willoughby and Rahn, 2004; Powell *et al.*, 2005; IPET, 2008) and theoretical arguments (Shen, 2006) show that R_{max} increases when the hurricane intensity ΔP_{max} decreases or the latitude φ increases. Here we assume that ($\ln R_{max} | \Delta P_{max}$) has the normal distribution proposed by Vickery *et al.* (2000), which for the region of New Orleans ($\varphi \approx 30^{o}$N) has parameters

$$\begin{aligned} m_{\ln R_{max} | \Delta P_{max}} &= 3.962 - 0.00567 \Delta P_{max} \\ \sigma_{\ln R_{max} | \Delta P_{max}} &= 0.313 \end{aligned} \tag{3.14}$$

where R_{max} is in km and ΔP_{max} is in mb.

The translational speed V_t has weak dependence on the intensity of the TC (Chen *et al.*, 2006; IPET, 2008) and is usually modeled as a lognormal variable with mean value around 6m/s and standard deviation around 2.5m/s; see Vickery and Twisdale (1995), Vickery *et al.* (2000), and Chen *et al.* (2006). The former two studies report a slight dependence of V_t on the approach angle α. To keep the TC recurrence model simple, we use for V_t a lognormal distribution with the above mean value and standard deviation and assume that V_t and α are independent.

Different studies have concluded that the pressure deficit ΔP_{max} has lognormal, Weibull or Gumbel distribution. The Weibull distribution gives better fits when all tropical cyclones are considered, whereas the lognormal distribution is more appropriate for storms in the hurricane intensity range; see Vickery and Twisdale (1995), Chouinard *et al.* (1997) and IPET (2006). The Gumbel distribution has been suggested by IPET (2008) for storms in the CAT35 range ($\Delta P_{max} >$ 58mb). While the Gumbel distribution is appropriate for the analysis of surges, winds and waves (for which the long-term risk is dominated by intense storms), significant rainfall is contributed by less intense slow-moving systems; see Section 3.5.2 below. For this reason we model ΔP_{max} using the lognormal distribution suggested by IPET (2006). This study shows that for TCs with $\Delta P_{max} > 34$mb that made landfall in the longitudinal range 85^{o}-95^{o}W, ΔP_{max} is accurately described by a shifted lognormal distribution with shift parameter 18mb, log-mean 3.15 and log-standard deviation 0.68.

Finally, we set $\lambda = 0.57$ events/yr, which is the rate found by IPET (2006) for TCs with $\Delta P_{max} > 34$mb making landfall between 85^{o}-95^{o}W along the Gulf of Mexico coast.

3.5.2 IDF curves for TC-rainfall and comparison with other storms

Next we use equation (3.11) with the recurrence model in Section 3.5.1 to estimate the intensity-duration-frequency (IDF) curves for New Orleans associated with tropical cyclones. The model explicitly accounts for variability in y, V_{max}, R_{max} and V_t. All other input parameters to the MSR model are fixed to the values used in Sections 3.3 and 3.4. The joint density of $\{y, V_{max}, R_{max}, V_t\}$

for a TC that makes landfall between longitudes 85°-95°W, $f_{y,\theta}$, is obtained by first calculating the joint density conditional on the pressure deficit ΔP_{max} under the assumption that the variables y, $[V_{max}|\Delta P_{max}]$, $[R_{max}|\Delta P_{max}]$ and V_t are independent and then averaging the conditional density with respect to ΔP_{max}.

Figure 3.13.a shows the calculated IDF curves as plots of rainfall intensity i against duration D for different return periods T.

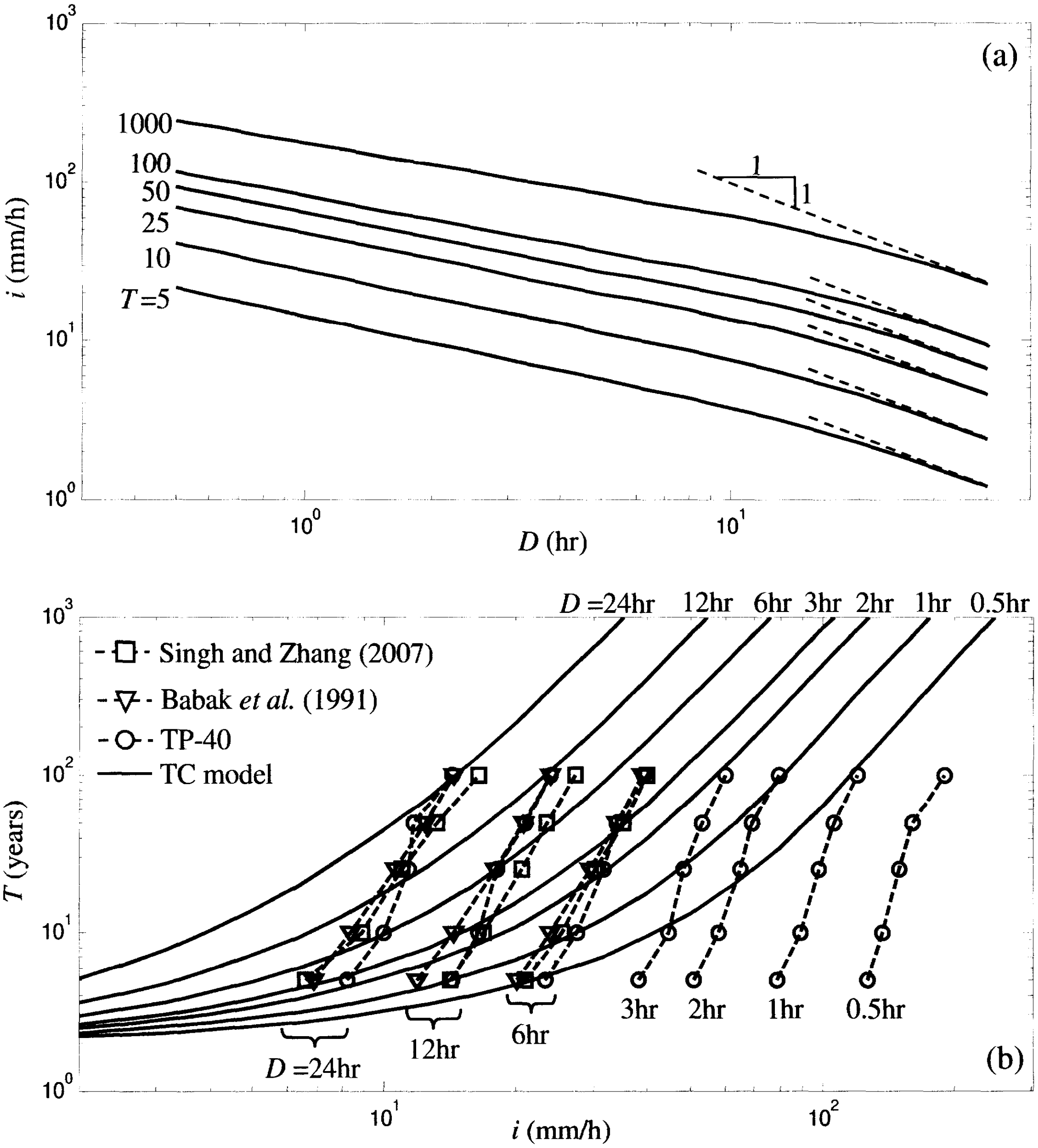

Figure 3.13: Theoretical IDF curves for New Orleans obtained from equation (3.11). (a) Maximum rainfall intensity i as a function of averaging duration D for different return periods T. (b) Comparison of the IDF values in (a) for different averaging durations D (solid lines) with intensities obtained from continuous rainfall records.

For durations below about 12 hours, the decay of i with D follows a power law $D^{-\gamma_D}$ where $\gamma_D \approx 0.55$. This exponent is slightly smaller than the values around 0.6-0.7 that are typical of extra-tropical rainfall (because the rainfall intensities associated with long durations in TCs tend to be high relative to extra-tropical events); see for example Langousis *et al.* (2007). For longer averaging durations, the exponent γ_D rapidly increases and is effectively 1 for $D > 24$ hours; see dashed lines in Figure 3.13.a. The reason is that the passage of a hurricane usually lasts less than 24 hours; hence for $D > 24$ the total rainfall depth is approximately constant and the average rainfall intensity depends on D like D^{-1}.

Figure 3.13.b shows the same results as plots of T against i for different averaging durations D. The curves are compared with values from TP-40 (Hersfield, 1961); Babak *et al.* (1991) and Singh and Zhang (2007) for return periods $T = 5$, 10, 25, 50 and 100yr. The latter values refer to generic rainfall in the New Orleans area and therefore include both TC and non-TC events. The rainfall values reported in TP-40 cover the whole duration range from 0.5-24hrs, whereas Babak *et al.* (1991) and Singh and Zhang (2007) give rainfall values only for $D = 6$, 12 and 24hr. It is clear from Figure 3.13.b that for $T > 100$yr also the dependence of the rainfall intensity on T is of the power-law type, say T^{γ_T} with $\gamma_T \approx 0.32$. This exponent is higher than the values around 0.20-0.25 that are typical of ordinary rainfall (Langousis *et al.*, 2007; Veneziano *et al.*, 2006b). The higher exponent in tropical cyclones is related to the large dispersion of the amplification factor $\beta_{l,max}$ (see example plots in Figure 3.12).

Another feature of the TC curves in Figure 3.13.b is the lower asymptote at $T = 1/\lambda = 1.75$yr. This lower bound is a consequence of the fact that the return period of any TC-induced rainfall intensity cannot be lower than the return period of the TCs themselves. The effect of this lower bound is that for short return periods, say $T < 10$yr, the precipitation intensities from tropical cyclones are far below those from ordinary rainfall (frontal events, mesoscale convective systems etc.), for which the recurrence rate is much higher. By contrast, for long durations ($D >$ 12hr) and long return periods ($T = 100$yr), the calculated TC intensities are close to the empirical intensities, indicating that tropical cyclones have a dominant effect on those extreme values. Given that the TC curves in Figure 3.13.b are flatter than those for overall rain, it is expected that tropical cyclones become even more dominant for longer return periods. For short durations (e.g. D on the order of 1hr), the contribution of tropical rainfall to the risk is negligible, irrespective of the return period.

It is also of interest to determine which tropical cyclones contribute the most to rainfalls in excess of the IDF values $i(D,T)$. Such TCs might for example be used as scenario events when designing for return period T. The main parameters to be considered are $\boldsymbol{\theta} = [V_{max}, R_{max}, V_t]$ and the distance y to the cyclone center. Their modal (most likely) values are obtained by maximizing the conditional probability density of $(y,\boldsymbol{\theta})$ given $I_{D,max} > i(D,T)$. This conditional density is given by

$$f_{y,\boldsymbol{\theta}|D,T}(y,\boldsymbol{\theta}) \propto f_{y,\boldsymbol{\theta}}(y,\boldsymbol{\theta})\, P[I_{D,max}(y,\boldsymbol{\theta}) > i(D,T)] \tag{3.15}$$

Figure 3.14 shows the modal values of V_{max}, R_{max} and V_t for different D and T. The most likely distance y always satisfies $y \approx R_{max}$. This makes sense because R_{max} is the distance at which the MSR model predicts maximum large-scale rainfall intensities.

Figure 3.14.a shows that the mode of V_{max} increases when either D or T increase. This makes physical sense since for any given D, higher rainfall intensities require more intense storms, and for any given T, intense precipitation over longer durations is associated with more intense systems. Figure 3.14.b shows that the mode of V_t decreases as T increases, meaning that more intense rainfall is generally produced by slower-moving systems. For durations smaller than 12 hours, the modal value of V_t is insensitive to D, whereas for longer durations V_t decreases faster with T. This faster decay is related to the fact that, for durations D on the order of one day or longer, extremely high rainfall intensities are produced by storms that take a time close to D to pass over the site. Therefore, for T large the translation speed V_t tends to be inversely proportional to D. Finally, Figure 3.14.c shows that the mode of R_{max} decreases when either D or T increase. This makes sense, since more intense storms tend to have smaller values of R_{max}; see Section 3.5.1.

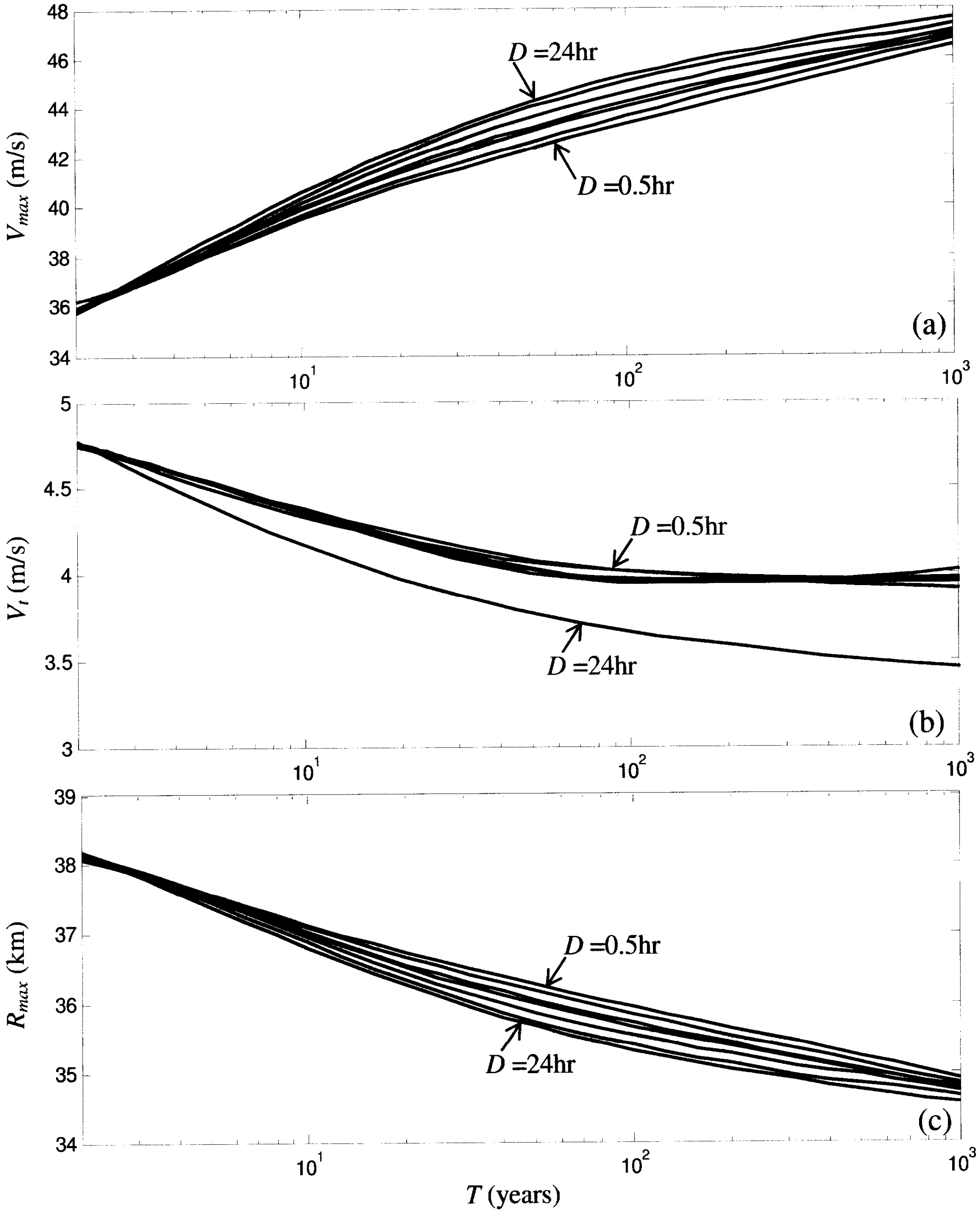

Figure 3.14: Modal values of (V_{max}, V_t, R_{max}) conditioned on exceeding the T-yr rainfall intensity for duration D = 0.5, 1, 3, 6, 12 and 24hr.

3.6 Conclusions

We have developed a methodology to assess the frequency of extreme rainfall intensities from tropical cyclones (TCs) in coastal areas. The mean rainfall field associated with a TC with maximum tangential wind speed V_{max}, radius of maximum winds R_{max}, and translation speed V_t is obtained using a physically-based ("MSR") model (Chapter 2), whereas rainfall variability at both large scales (from storm to storm) and small scales (due to rainbands and local convection within a single storm) is modeled statistically. The statistical component of the model is estimated using 38 precipitation radar (PR) frames from the TRMM mission; see Table 3.1. These frames cover a wide range of TC intensities V_{max} and vortex sizes R_{max}. To make the model easier to use in risk analysis, we developed approximate analytical expressions for the statistical parameters. We use Taylor's hypothesis to convert spatial rainfall intensity fluctuations to temporal fluctuations as the storm passes over a given geographical location A. The combined physical-statistical model predicts the maximum rainfall intensity at A during a period of duration D for a TC with characteristics (V_{max}, R_{max}, V_t) whose center passes at distance y from A. To illustrate the use of the model for long-term rainfall risk analysis, we formulated a recurrence model for tropical cyclones in the Gulf of Mexico that make landfall between longitudes 85°-95°W and used the rainfall and recurrence models to assess the rainfall risk for New Orleans. Our main findings are as follows.

The maximum rainfall $I_{l,max}$ in a spatial interval of length l depends on l, the distance y from the center of the TC, and the intensity V_{max} and size R_{max} of the vortex. We expressed $I_{l,max}$ as the product of the large-scale ($L \approx 400$ km) average rainfall intensity produced by the MSR model, $I_{L,MSR}$, and an amplification factor $\beta_{l,max}$ that includes both storm-to-storm variability and spatial fluctuations of rainfall intensity within a storm. The distribution of $\beta_{l,max}$ depends of course on l, but in addition depends significantly on the large-scale intensity $I_{L,MSR}$ and the normalized distance from the storm center, $y' = |y/R_{max}|$. Specifically, the dispersion of $\beta_{l,max}$ increases as l and $I_{L,MSR}$ decrease or $y' = |y/R_{max}|$ increases. These trends with $I_{L,MSR}$ and y' are linked to the fact that lower intensity storms and larger distances y' are associated with higher dry area fractions, more intermittent rainfall, and therefore an increased dispersion of the rainfall maxima.

Application of the model to TC rainfall risk for New Orleans has produced interesting insight into the importance of tropical cyclones relative to other rainfall-producing events. For short return periods T, the TC intensities are significantly below those from other storms, which have a much higher rate of occurrence. However, as the return period T increases, the TC estimates for long averaging durations (D around 12-24 hours) approach the values found from continuous rainfall records. This means that for long return periods, the long-duration TC rainfalls tend to dominate. In New Orleans, this happens for T around 100 years.

To determine how the most likely TC scenario varies with the averaging duration D and the return period T, we calculated the joint distribution of $\{V_{max}, R_{max}, V_t, y\}$ conditioned on exceeding the T-yr rainfall intensity for duration D. Then we plotted the modal values of V_{max}, R_{max}, and V_t against D and T; see Figure 3.14 (for y, the modal value is always close to R_{max}). The modal value of V_{max} increases when D or T increase, whereas the opposite is true for R_{max}. The mode of the translation velocity V_t is insensitive to D for $D < 24$hr, but decreases with increasing T and with increasing D for $D > 24$hr.

4. Conclusions

In this thesis we combined data analysis and physical modeling to develop a methodology for the frequency of extreme rainfall intensities caused by tropical cyclones (TCs) in coastal areas. The mean rainfall field associated with a TC with maximum tangential wind speed V_{max}, radius of maximum winds R_{max}, and translation speed V_t is obtained using a physically-based model (Chapters 1 and 2), whereas rainfall variability at both large scales (from storm to storm) and small scales (due to rainbands and local convection) is modeled statistically (Chapter 3).

The theoretical model of TC rainfall is based on the assumption that the vertical outflow of water vapor from the TC boundary layer (BL) is all converted into rainfall. This water vapor flux originates from the low-level convergence of the horizontal flow. Evaluation of the BL winds is based on Smith's (1968) axi-symmetric formulation, modified in Chapter 1 to account for storm motion. The resulting models of wind and rainfall are referred to as the modified-Smith (MS) BL model and the modified-Smith-for-rainfall (MSR) model, respectively. Our main findings from Chapters 1-3 are outlined below.

MS model for evaluation of the boundary layer winds

The MS scheme estimates the horizontal and vertical wind velocity fields inside the BL from a few TC characteristics: the maximum tangential wind speed V_{max}, the radius of maximum winds R_{max}, and Holland's B parameter, in addition to the storm translation velocity V_t, the surface drag coefficient C_D, and the vertical diffusion coefficient of the horizontal momentum K. The scheme is computationally very efficient and is stable also for large B values and fast-moving storms. Model results were compared to those from other studies (Shapiro 1983; Kepert 2001) and validated using the Fifth-Generation Pennsylvania State University/NCAR Mesoscale Model (MM5).

We find that Kepert's (2001) BL model significantly underestimates the radial and vertical fluxes, whereas Shapiro's (1983) slab-layer formulation produces radial and vertical winds that are a factor of about 2 higher than those produced by MM5. The velocity fields generated by the present model are consistent with MM5 and with tropical cyclone observations.

In a sensitivity analysis we used the MS model to study how the symmetric and asymmetric components of the wind field vary with the storm parameters mentioned above. In accordance with observations, we find that larger values of B and lower values of R_{max} produce horizontal and vertical wind profiles that are more picked near the radius of maximum winds. We also find that, when cyclones in the Northern (Southern) hemisphere move, the vertical and storm-relative radial winds intensify at the right-front (left-front) quadrant of the vortex, whereas the storm-relative tangential winds are more intense in the left-front (right-front) region. The asymmetry is higher for faster moving TCs and for higher surface drag coefficients C_D.

MSR model for evaluation of the mean rainfall field in TCs

The MSR model calculates the upward moisture flux that converts into rainfall from the vertical winds generated by the MS model and two additional parameters: the average temperature $\bar{T}$ and average saturation ratio $\bar{Q}$ inside the TC boundary layer. The rainfall field generated by the MSR model is not simply proportional to the vertical wind field at the top of the boundary layer produced by the MS model. This is because (1) the trajectory of moisted air parcels has an outward slant depending on distance from the TC center and (2) the ascending air parcels and descending rain drops are advected into a helical motion by the cyclonic circulation; therefore a parcel of air that leaves the TC boundary layer contributes rainfall to a range of azimuthal locations. The azimuthal redistribution is important only for radially asymmetric flows; i.e. when $V_t \neq 0$. The relation between vertical winds and surface rainfall has been verified through MM5 simulations. The MSR model accurately reproduces the rainrate estimates extracted from the precipitation radar (PR) data of the TRMM mission.

In a sensitivity analysis we found that the temperature $\bar{T}$, the saturation ratio $\bar{Q}$ and the vertical diffusion coefficient K have small effect on the calculated rainfall intensities. Consequently, setting those parameters to constant values (e.g. to $\bar{T} = 22^{o}C$, $\bar{Q} = 0.8$ and $K = 50m^2/s$, as was done in Sections 2.3-2.5) does not induce large errors. By contrast, the maximum tangential velocity V_{max} and the roughness of the surface boundary (expressed through C_D) have significant effects on rainfall intensity. The latter increases when either V_{max} or C_D increase. Lower values of R_{max} produce rain rates that are more picked and more concentrated near the TC center. The B parameter has a small effect on the peak rainfall intensity, but influences the rate at which rainfall decays with radial distance (higher values of B result in faster decay).

For a TC that moves in the Northern (Southern) hemisphere the effect of the translation velocity V_t is to intensify rainfall at the right (left) and right-front (left-front) of the storm.

Larger asymmetries are associated with higher velocities V_t. These findings are in accordance with empirical observations (Lonfat *et al.*, 2004). The effect of C_D is more complex: at the front of the storm, rainfall asymmetry is insensitive to C_D, whereas at the rear-right (rear-left) the rainfall asymmetry increases with decreasing C_D.

An important departure from previous studies is that we parameterize rainfall asymmetries in TCs in terms of storm motion not vertical wind shear; see Chapter 2. We have used MSR model simulations and empirical data on rainfall asymmetry (Chen *et al.*, 2006) to verify that the asymmetries produced by storm motion are close to those observed and often parameterized in terms of vertical wind shear; see Section 2.5. Since, in risk analysis, one may equivalently use shear or motion as conditioning parameter and, in addition, it is easier to include motion than shear when modeling rainfall (see Section 3.5), we have chosen to develop a motion-based rather than shear-based parameterization of rainfall asymmetry.

Stochastic fluctuation component and an application to rainfall risk for New Orleans

The MSR model should prove useful for climatologic studies, but for hazard analysis it has the major limitation of ignoring the small-scale rainfall variations associated with rainbands and local convection. These variations have an important effect on the distribution of $I_{D,max}$: the maximum of the average rainfall intensity over duration D at location A during the passage of a storm. We obtained the distribution of $I_{D,max}$ by adding a stochastic component to the MSR model predictions.

The combined physical-statistical model predicts the maximum rainfall intensity at A during a period of duration D for a TC with characteristics (V_{max}, R_{max}, V_t) whose center passes at distance y from A (the other parameters of the MSR model are set to $K = 50\text{m}^2/\text{s}$, $C_D = 0.002$, $\bar{T} = 22^\circ\text{C}$, $\bar{Q} = 0.8$ and $B = 1$). To illustrate the use of the model for long-term rainfall risk analysis, we formulated a recurrence model for tropical cyclones in the Gulf of Mexico. We then used the rainfall and recurrence models to assess the rainfall risk for New Orleans and compared our results with empirical IDF estimates for all rainstorms (TCs and non-TCs) in the region.

We found that for short return periods T, the TC intensities are significantly below those from other storms, which have a much higher rate of occurrence. However, as the return period T increases, the TC estimates for long averaging durations (D around 12-24 hours) approach the values found from continuous rainfall records. This means that for long return periods, the long-duration TC rainfalls tend to dominate. In New Orleans, this happens for T around 100 years.

We also determined how the most likely TC scenario varies with the averaging duration D and the return period T. We did so by plotting the modal values of V_{max}, R_{max}, and V_t conditioned on exceeding the T-yr rainfall intensity for duration D (for y, the modal value is always close to R_{max}, the location where the MSR model predicts maximum large-scale rainfall intensities). These modal values can for example be used as scenario events when designing for return period T.

The mode of V_t decreases as T increases. This means that more intense rainfall is generally produced by slower-moving systems. For durations smaller than 12 hours, the modal value of V_t is insensitive to D, whereas for longer durations V_t decreases faster with T. This faster decay is related to the fact that, for durations D on the order of one day or longer, extremely high rainfall intensities are produced by storms that take a time close to D to pass over the site.

The modal value of R_{max} decreases when D or T increase, whereas the opposite is true for V_{max}. Both findings make sense since intense storms tend to have smaller values of R_{max} (see Section 3.5.1) and for any given D, higher rainfall intensities require more intense storms, and for any given T, intense precipitation over longer durations is associated with more intense systems.

Future research directions

A rich parameterization and high computational efficiency make the proposed model attractive for rainfall risk applications in TC-prone areas, where one must assess tropical cyclone rainfall under many storm and environmental scenarios. This requirement effectively rules out the use of full-physics high-resolution numerical weather prediction models.

Although computationally efficient, the current version of the model requires numerical calculation of the large-scale rainfall intensity $I_{L,MSR}$ in equation (3.2) using the MS and MSR models. In Section 3.4 we found that when V_{max} and $y' = |y/R_{max}|$ are kept fixed, the sensitivity of $I_{L,MSR}$ to both V_t and R_{max} is low. Hence, one could significantly reduce the computational effort and make the model more user-friendly by parameterizing $I_{L,MSR}$ in terms of V_{max} and y'. This parameterization would be worth pursuing.

A limitation of the current framework is that it does not account for post-landfall conditions and therefore is applicable only to open-water or coastal sites. When extending the model to inland locations, one should investigate whether the statistics of the small scale rainfall variations in Chapter 3 remain valid over land. Based on findings of other studies on the effects of orography on the spatial variability of extra-tropical rainfall (Pathirana and Herath, 2002; Badas *et al.*, 2005; Deidda *et al.*, 2006), we anticipate that for sites not very far inland the statistical model for the rainfall fluctuations would not change. In this case, one can use a correction factor to multiply the theoretical $I_{L,MSR}$ rainrates to account for the effects of topography at inland locations. For example, Lonfat *et al.* (2007) use a simple formulation where this factor is proportional to the product of surface winds and the gradient of ground elevation.

It is possible to extend the current framework to deal with short term rainfall prediction. For this purpose one needs to start with real-time information on the storm and use some type of a TC-track model to calculate the distribution of the location y and the characteristics $\boldsymbol{\theta}$ of the storm at landfall. The joint distribution of $(y,\boldsymbol{\theta})$ can be used as a short-term recurrence model in equation 3.11 (for $\lambda = 1$) to assess rainfall risk at the site. In this case one should check the accuracy of the rainfall estimates produced by the suggested model relative to those calculated by simple translation and possibly intensification/deintensification of real-time radar rainfall estimates over the site. The latter method is usually referred to as tropical rainfall potential (TRaP) technique (e.g. Kidder *et al.*, 2005). We anticipate that for leads shorter than a day the TRaP technique should produce more accurate rainfall estimates.

Another possible research direction is to extend the current framework to maximum TC wind speeds. For example, one could use the MS model to predict the mean wind field in a TC with given characteristics $\boldsymbol{\theta}$ and analysis of surface wind observations to evaluate statistically the wind gust factor.

References

Abbs, D.J. (1999) A Numerical Modelling Study to Investigate the Assumptions Used in the Calculation of Probable Maximum Precipitation, *Water Resour. Res.*, **35**, 785–796.

Alpert, P. (1986) Mesoscale Indexing of the Distribution of Orographic Precipitation over High Mountains, *J. Clim. Appl. Meteor.*, **25**, 532-545.

Anthes, R. A. (1982) *Tropical Cyclones: Their Evolution, Structure, and Effects*, Meteorological Monographs Number 41, American Meteorological Society, Boston, MA,

Anthes, R.A. (1971) Iterative Solutions to the Steady-state Axisymetric Boundary Layer Equations under an Intense Pressure Gradient, *Mon Wea. Rev.*, **99**, 261-268.

Atkinson, G.D. and C.R. Holiday (1977) Tropical Cyclone Minimum Sea Level Pressure-maximum Sustained Wind Relationship for Western North Pacific, *Mon. Wea. Rev.*, **105**, 421-427.

Babak, N., V.P. Singh and F.X. Yu (1991) *LADOTD 24-hour rainfall frequency maps and IDF curves*, Louisiana Transportation Research Center, Baton Rouge, La.

Badas M.G., R. Deidda and E. Piga (2005) Orographic Influences in Rainfall Downscaling, *Adv. Geosci*, 2, 285-292.

Black, M.L., J.F. Gamache, F.D. Marks Jr., C.E. Samsury, and H.E. Willoughby (2002) Eastern Pacific Hurricanes Jimena of 1991 and Olivia of 1994: The Effect of Vertical Shear on Structure and Intensity, *Mon. Wea. Rev.*, **130**(9), 2291-2312.

Bode, L. and R.K. Smith (1975) A Parameterization of the Boundary Layer of a Tropical Cyclone. *Bound. Layer Meteor.*, **8**, 3-19.

Bolen, S.M. and V. Chandrasekar (2000) Quantitative Cross Validation of Space-Based and Ground-Based Radar Observations, *J. Appl. Meteor.*, **39**, 2071–2079.

Chapra, S.C. and R.P. Canale (2002) *Numerical Methods for Engineers*, 4th Edition, McGraw-Hill, New York, U.S.A.

Chen, S.S., J.F. Price, W. Zhao, M.A. Donelan, and E.J. Walsh (2007) The CBLAST-hurricane Program and the Next-generation Fully Coupled Atmosphere-wave-ocean Models for Hurricane Research and Prediction, *Bull. Amer. Meteor. Soc.*, **88**, 311-317.

Chen, S.S., M. Lonfat, J.A. Knaff, and F.D. Marks, Jr. (2006) Effects of Vertical Wind Shear and Storm Motion on Tropical Cyclone Rainfall Asymmetries Deduced from TRMM, *Mon. Wea. Rev.*, **134**, 3190-3208.

Chouinard, L.E., C. Liu and C.K. Cooper (1997) Model for Severity of Hurricanes in Gulf of Mexico, *J. of Waterway, Port, Coastal and Ocean Engineering*, **123**(3), 120-129.

Chow, S. (1971) A Study of the Wind Field in the Planetary Boundary Layer of a Moving Tropical Cyclone. M.S. Thesis, Dept. of Meteor. and Oceanogr., New York University, 59pp. [NOAA/NHRL Library, 1320 South Dixie Highway, Coral Gables, FL 33146].

Chow, V.T., D.R. Maidment and L.W. Mays (1988) *Applied Hydrology*, McGraw-Hill, New York.

Corbosiero, K.L., and J. Molinari (2002) The Effects of Vertical Wind Shear on the Distribution of Convection in Tropical Cyclones, *Mon. Wea. Rev.*, **130**, 2110–2123.

Corbosiero, K.L., and J. Molinari (2003) The Relationship between Storm Motion, Vertical Wind Shear, and Convective Asymmetries in Tropical Cyclones, *J. Atmos. Sci.*, **60**, 366–376.

Deidda, R., M. Grazia-Badas and E. Piga (2006) Space–time Multifractality of Remotely Sensed Rainfall Fields, *J. Hydrol.*, **322**, 2-13, doi:10.1016/j.jhydrol.2005.02.036.

Demuth, J., M. DeMaria and J.A. Knaff (2006) Improvement of Advanced Microwave Sounder Unit Tropical Cyclone Intensity and Size Estimation Algorithms, *J. Appl. Meteor.*, **45**, 1573-1581.

Donelan, M. A., B. K. Haus, N. Reul, W. J. Plant, M. Stiassnie, H. C. Graber, O. B. Brown and E. S. Saltzman (2004) On the Limiting Aerodynamic Roughness of the Ocean in Very Strong Winds. *Geophys. Res. Lett.*, **31**, L18306, doi:10.1029/2004GL019460.

Eliassen, A. and M. Lystad (1977) The Ekman Layer of a Circular Vortex: A numerical and Theoretical Study. *Geophys. Norv.*, **31**, 1-16.

Emanuel, K.A. (1986) An Air-sea Interaction Theory for Tropical Cyclones. Part I: Steady State Maintenance. *J. Atmos. Sci.*, **43**, 585-604.

Emanuel, K.A. (1989) Polar Lows as Artic Hurricanes. *Tellus*, **41A**, 1-17.

Fall, S., D. Niyogi, U.C. Mohanty, and A. Kumar (2007) Application of Weather Prediction Models for Hazard Mitigation Planning: A Case Study of Heavy off-Season Rains in Senegal, *Nat. Hazards*, **41**, 227–243, doi:10.1007/s11069-006-9033-x

Ferraro, R., P. Pellegrino, M. Turk, W. Chen, S. Qiu, R. Kuligowski, S. Kusselson, A. Irving, S. Kidder and J. Knaff (2005) The Tropical Rainfall Potential (TRaP) Technique. Part II: Validation, *Wea. Forecasting*, **20**, 465–475.

Frank, W.M. (1977) The Structure and Energetics of the Tropical Cyclone: I. Storm Structure. *Mon. Wea. Rev.*, **105**, 1119-1135.

Gebremichael, M., T.M. Over and W.F. Krajewski (2006) Comparison of the Scaling Properties of Rainfall Derived from Space- and Surface-based Radars. *J. of Hydrometeor.*, **7**, 1277-1294.

Goodyear, H.V. (1968) Frequency and Areal distributions of Tropical Storm Rainfall in the United States Coastal Region on the Gulf of Mexico, ESSA Tech. Rep. WB-7, Washington, DC, 48 pp. [Available from NOAA Miami Regional Library, Atlantic Oceanographic and Meteorological Laboratory (AOML), 4301 Rickenbacker Causeway Miami, FL 33149.]

Gray, W.M., E. Ruprecht, and R. Phelps (1975) Relative Humidity in Tropical Weather Systems. *Mon. Wea. Rev.*, **103**, 685-690.

Gupta, V.K. and E. Waymire (1993) A Statistical Analysis of Mesoscale Rainfall as a Random Cascade, *J. Appl. Meteorol.*, **32**(2), 251-267.

Haurwitz, B. (1935) On the Variation of Wind with Elevation under the Influence of Viscosity in Curved Air Currents. *Beitrage zur Geophysik*, **45**, p.243.

Hawkins, H.F. and D.T. Rubsam (1968) Hurricane Hilda, 1964. II. Structure and Budgets of the Hurricane on October 1, 1964. *Mon. Wea. Rev.*, **96**, 617-636.

Herbert, P.J., J.D. Jarrell, and M. Mayfield (1997) The Deadliest, Costliest, and Most Intense United States Hurricanes of this Century (and Other Frequently Requested Hurricane Facts), *NOAA Tech. Memo.*, NWS TPC-1, Miami, Florida.

Hershfield, D.M. (1961) Rainfall Frequency Atlas for the United States for Durations from 30 minutes to 24 hours and Return Periods from 1 to 100 years, *Technical Paper 40*, U.S. Weather Bureau, Washington, D.C.

Ho F.P., J.C. Su, K.L. Hanevich, R.J. Smith and F.P. Richards (1987) Hurricane Climatology fir the Atlantic and Gulf Coasts of the United States, NOAA Tech. Rep. NWS 38, completed under agreement EMW-84-E-1589 for FEMA, 194p.

Ho, F.P. and V.A. Myers (1975) Joint Probability Method of Tide Frequency Analysis Applied to Apalachicola Bay and St. George Sound, Florida, NOAA Tech. Rep. NWS 18, 43p.

Holland, G.J. (1980) An Analytic Model of the Wind and Pressure Profiles in Hurricanes, *Mon. Wea. Rev.*, **108**, 1212-1218.

Houze, R.A., S.S. Chen, and co-authors (2006) The Hurricane Rainband and Intensity Change Experiment (RAINEX): Observations and Modeling of Hurricanes Katrina, Ophelia, and Rita (2005), *Bull. Amer. Meteor. Soc*, **87**, 1503-1521.

Houze, R.A., S.S. Chen, B. Smull, W.-C. Lee, and M. Bell (2007) Hurricane Intensity and Eyewall Replacement, *Science*, **315**, 1235-1239.

Interagency Performance Evaluation Taskforce (I.P.E.T.) (2006) *Engineering and Operational Risk and Reliability Analysis*, Volume VIII, Technical Appendix J, 60% Progress Report, United States Army Corps of Engineers.

Interagency Performance Evaluation Taskforce (I.P.E.T.) (2008) *Engineering and Operational Risk and Reliability Analysis*, Volume VIII, Technical Appendix 8: Hazard Analysis, United States Army Corps of Engineers, https://ipet.wes.army.mil/

Jarvinen, B.R., C.J. Neumann and M.A.S. Davis (1984) A Tropical Cyclone Data Tape for the North Atlantic Basin 1886-1993: Contents, Limitations and Uses, *NOAA Tech. Memo. NWS-NHC-22*, U.S. Department of Commerce, Washington, D.C.

Jiang, H., P.G. Black, E.J. Zipser, F.D. Marks Jr., and E.W. Uhlhorn (2006) Validation of Rain Rate Estimation in Hurricanes from the Stepped Frequency Microwave Radiometer: Algorithm Correction and Error Analysis, *J. Atmo. Sci.*, **63**(1), 252-267.

Jorgensen, D.P. (1984a) Mesoscale and Convective-scale Characterisitcs of Mature Hurricanes. Part I: General Observations by Research Aircraft, *J. Atmo. Sci.*, **41**(8), 1268-1286.

Jorgensen, D.P. (1984b) Mesoscale and Convective-scale Characterisitcs of Mature Hurricanes. Part II: Inner Core Structure of Hurricane Allen (1980), *J. Atmo. Sci.*, **41**(8), 1287-1311.

Juneng, L., F.T. Tangang, C.J.C. Reason, S. Moten, and W.A.W. Hassan (2007) Simulation of Tropical Cyclone Vamei (2001) Using the PSU/NCAR MM5 Model, *Meteorol. Atmos. Phys.*, **97**, 273–290, doi: 10.1007/s00703-007-0259-2

Kepert, J. (2001) The Dynamics of Boundary Layer Jets within the Tropical Cyclone Core. Part I: Linear Theory. *J. Atmo. Sci*, **58**, 2469-2484.

Kepert, J. (2006a) Observed Boundary Layer Wind Structure and Balance in the Hurricane Core. Part I: Hurricane Georges, *J. Atmo. Sci*, **63**, 2169-2193.

Kepert, J. (2006b) Observed Boundary Layer Wind Structure and Balance in the Hurricane Core. Part II: Hurricane Mitch, *J. Atmo. Sci*, **63**, 2194-2211.

Kepert, J. and Y. Wang (2001) The Dynamics of Boundary Layer Jets within the Tropical Cyclone Core. Part II: Nonlinear Enhancement. *J. Atmos. Sci.*, **58**, 2485-2501.

Kidder, S.Q., S.J. Kusselson, J.A. Knaff, R.R. Ferraro, R.J. Kuligowski, and M. Turk (2005) The Tropical Rainfall Potential (TRaP) Technique. Part I, *Wea. Forecasting*, **20**, 456–464.

Koutsoyiannis, D., D. Kozonis and A. Manetas (1998) A Mathematical Framework for Studying Rainfall Intensity-Duration-Frequency Relationships, *J. Hydrol.,* **206**, 118-135.

Kummerow, C., W. Barnes, T. Kozu, J. Shiue and J. Simpson (1998) The Tropical Rainfall Measuring Mission (TRMM) Sensor Package. *J. Atmos. Oceanic Technol.*, **15**, 809–817.

Kundu, K.K. and I.M. Cohen (2004) *Fluid Mechanics.* 3rd Edition, Elsevier Academic Press.

La Seur, N.E. and H.F. Hawkins (1963) An Analysis of Hurricane Cleo (1958) Based on Data from Research Reconnaissance Aircraft. *Mon. Wea. Rev.*, **91**, 694-709.

Landsea, C.W. (2000) Climate Variability of Tropical Cyclones, In: *Storms*, Vol.1, Edited by: R. Pielke, Jr. and R. Pielke, Sr., Routledge, NY.

Langousis A, D. Veneziano, P. Furcolo, and C. Lepore (2007) Multifractal Rainfall Extremes: Theoretical Analysis and Practical Estimation, *Chaos Solitons and Fractals*, doi:10.1016/j.chaos.2007.06.004.

Langousis, A. and D. Veneziano (2007) Intensity-duration-frequency Curves from Scaling Representations of Rainfall, *Wat. Resour. Res.*, **43**, doi: 10.1029/2006WR005245.

Langousis, A. and D. Veneziano (2008) Theoretical Model of Rainfall in Tropical Cyclones for the Assessment of Long-term Risk, *J. Geophys. Res.*, doi:10.1029/2008JD010080.

Langousis, A. and D. Veneziano (2009) Long Term Rainfall Risk from Tropical Cyclones in Coastal Areas, *Wat. Resour. Res.*, (under review).

Langousis, A., D. Veneziano, and S. Chen (2008) Boundary Layer Model for Moving Tropical Cyclones, In: *Hurricanes and Climate Change*, Edited by: J. Elsner and T.H. Jagger, Springer.

Large, W. G. and S. Pond (1981) Open Ocean Momentum Flux Measurements in Moderate to Strong Winds, *J. Phys. Oceanogr.*, **11**, 324–336.

Lee, T.F., F.J. Turk, J. Hawkins and K. Richardson (2002) Interpretation of TRMM TMI Images of Tropical Cyclones, *Earth Interactions*, **6**, 1–17.

Leslie, L.M. and R.K. Smith (1970) The Surface Boundary Layer of a Hurricane- Part II. *Tellus*, **22**, 288-297.

Liao, L., R. Meneghini and T. Iguchi (2001) Comparisons of Rain Rate and Reflectivity Factor Derived from the TRMM Precipitation Radar and the WSR-88D over the Melbourne, Florida, Site. *J. Atmos. Oceanic Technol.,* **18**, 1959–1974.

Lonfat, M., F.D. Marks, Jr. and S.S. Chen (2004) Precipitation Distribution in Tropical Cyclones using the Tropical Rainfall Measuring Mission (TRMM) Microwave Imager: A Global Perspective, *Mon. Wea. Rev.*, **132**, 1645-1660.

Lonfat, M., R. Rogers, T. Marchok, and F.D. Marks Jr. (2007) A Parametric Model for Predicting Hurricane Rainfall, *Mon. Wea. Rev.*, **135**, 3086-3097.

Lovejoy, S. and D. Schertzer (1995) Multifractals and Rain, In: *New Uncertainty Concepts in Hydrology and Hydrological Modelling*, Edited by: Kundzewicz, A.W., Cambridge press.

Mack, L.M. (1962) The Laminar Boundary Layer on a Disk of Finite Radius in a Rotating Fluid. Calif. Instit. of Tech. Rep. No. 32-224.

Madsen, H., P.F. Rasmussen and D. Rosbjerg (1997) Comparison of Annual Maximum Series and Partial Duration Series Methods for Modeling Extreme Hydrologic Events 1. At-site Modeling, *Wat. Resour. Res.*, **33**(4), 747-757.

Magagi, R., and A.P Barros (2004) Estimation of Latent Heating of Rainfall During the Onset of the Indian Monsoon Using TRMM PR and Radiosonde data, *J. Appl. Meteor.*, **43**, 328-349.

Marks, F. D. Jr., L.K. Shay, and PDT-5 (1998) Landfalling Tropical Cyclones: Forecast Problems and Associated Research Opportunities, *Bull. Amer. Meteor. Soc.*, **79**, 305-323.

Marks, F.D. Jr. (1985) Evolution of the Structure of Precipitation in Hurricane Allen (1980), *Mon. Wea. Rev.*, **113**, 909-930.

Marks, F.D. Jr., and R.A. Houze Jr. (1984) Airborne Doppler Radar Observations in Hurricane Debby, *Bull. Amer. Meteor. Soc.*, **65**, 569-582.

Miller, B.I. (1965) A Simple Model of the Hurricane Inflow Layer. Nat. Hurr. Res. Proj. Rep. No. 75, 16pp.

Molinari, J., P.K. Moore, V.P. Idone, R.W. Henderson and A.B. Saljoughy (1994) Cloud-to-ground Lightning in Hurricane Andrew, *J. Geophys. Res.*, **99**, 16 665-16 676.

Myers, V.A. (1957) Maximum Hurricane Winds. *Bull. Amer. Meteor. Soc.*, **38**, 227-228.

Myers, V.A. (1975) Storm Tide Frequencies on the South Carolina Coast, NOAA Tech. Rep. NWS-16, 79p.

Myers, V.A., and W. Malkin (1961) Some Properties of Hurricane Wind Fields as Deducted from Trajectories. NHRP Rep. 49, 45pp. [NOAA/NHRL Library, 1320 South Dixie Highway, Coral Gables, FL 33146].

Ossiander, M. and E.C. Waymire (2000) Statistical Estimation for Multiplicative Cascades, *Ann. Statist.*, **28**, 1533-1560.

Ossiander, M. and E.C. Waymire (2002) On Estimation Theory for Multiplicative Cascades, *The Indian Journal of Statistics*, **64**, 323-343.

Over, T.M. and V.K. Gupta (1996) A Space-time Theory of Mesoscale Rainfal Using Random Cascades, *J. Geophys. Res.*, **101**(D21), 26,319- 26,331.

Palmen, E. (1958) Vertical Circulation and Release of Kinetic Energy During the Development of Hurricane Hazel into an Extratropical Storm, *Tellus*, **10**(1), 1-23.

Pathirana, A. and S. Herath (2002) Multifractal Modelling and Simulation of Rain Fields Exhibiting Spatial Heterogeneity, *Hydrol. Earth Syst. Sci.*, **6**(4), 659–708.

Pfost, R.L. (2000) Operational Tropical Cyclone Quantitative Precipitation Forecasting, *Natl. Wea. Dig.*, **24**, 61–66.

Powell, M., G. Soukup, S. Cocke, S. Gulati, N. Morisseau-Leroy, S. Hamid, N. Dorst and L. Axe, (2005) State of Florida Hurricane Loss Projection Model: Atmospheric Science Component, *J. Wind Engineering and Industrial Aerodynamics,* **93**, 651-674.

Powell, M.D. (1990) Boundary Layer Structure and Dynamics in outer Hurricane Rainbands. Part I: Mesoscale Rainfall and Kinematic Structure, *Mon. Wea. Rev.*, **118**, 891-917.

Powell, M.D., P.J. Vickery, and T.A. Reinhold (2003) Reduced Drag Coefficient for High Wind Speeds in Tropical Cyclones, *Nature*, **422**, 279–283.

Rappaport, E.N. (2000) Loss of Life in the United States Associated with Recent Atlantic Tropical Cyclones, *Bull. Amer. Meteor. Soc.*, **81**, 2065-2074.

Renno, N. and A. Ingersoll (1996) Natural Convection as a Heat Engine: A Theory for CAPE. *J. Atmo. Sci.*, **53**(4), 572-585.

Riehl, H., and J. Malkus (1961) Some Aspects of Hurricane Daisy (1958), *Tellus*, **13**, 181–213.

Rogers, R., S. Chen, J. Tenerelli, H. Willoughby (2003) A Numerical Study of the Impact of Vertical Wind Shear on the Distribution of Rainfall in Hurricane Bonnie, *Mon. Wea. Rev.*, **131**, 1577-1599.

Rogers, R.F., M.L. Black, S.S. Chen, and R.A. Black (2007) An Evaluation of Microphysics Fields from Mesoscale Model Simulations of Tropical Cyclones. Part I: Comparisons with Observations, *J. Atmos. Sci.*, **64**, 1811–1834.

Rogers, R.R., and M.K. Yau (1996) *A Short Course in Cloud Physics*, Third Edition, Butterwirth Heinemann, U.S.A.

Rosenthal, S.L. (1962) A Theoretical Analysis of the Field of Motion in the Hurricane Boundary Layer. Nat Hurr. Res. Proj. Rep., No. **56**, 12pp.

Schertzer, D. and S. Lovejoy (1987) Physical Modeling and Analysis of Rain and Clouds by Anisotropic Scaling of Multiplicative Processes, *J. Geophys. Res.*, **92**, 9,693-9,714.

Schlichting, H. (1960) *Boundary Layer Theory.* 2nd Edition, McGraw Hill, London, Great Britain.

Schloemer, R.W. (1954) Analysis and Synthesis of Hurricane Wind Patterns over Lake Okechobee, FL. Hydromet. Rep. 31, 49pp [Govt. Printing Office, No. C30.70:31].

Schmitt, F., S. Vannistem and A. Barbosa (1998) Modeling of Rainfall Time Series Using Two-state Renewal Processes and Multifractals, *J. Geophys. Res.*, **103** (D18), 23,181-23,193.

Scofield, R.A. and R.J. Kuligowski (2003) Status and Outlook of Operational Satellite Precipitation Algorithms for Extreme Precipitation Events, *Wea. Forecasting*, **18**, 1037–1051.

Shapiro, L.J. (1983) The Asymmetric Boundary Layer Flow under a Translating Hurricane. *J. Atmos. Sci.*, **40**, 1984-1998.

Shen, W. (2006) Does the Size of Hurricane Eye Matter with its Intensity? *Geophys. Res. Lett.*, **33**, L18813, doi:10.1029/2006GL027313.

Simpson, J., R.F. Adler, and G.R. North (1988) Proposed Tropical Rainfall Measuring Mission (TRMM) Satellite, *Bull. Amer. Meteor. Soc.*, **69**, 278-295.

Simpson, R.H., and H. Riehl (1981) *The Hurricane and Its Impact*, Louisiana State University Press, 398 pp.

Singh, V. P. (1992) *Elementary Hydrology*, Prentice-Hall, New Jersey, U.S.A.

Singh, V.P. and L. Zhang (2007) IDF Curves Using the Frank Archimedean Copula, *J. Hydrol. Eng*, 10.1061/(ASCE)1084-0699(2007)12:6(651).

Smith, R.K. (1968) The Surface Boundary Layer of a Hurricane. *Tellus*, **20**, 473-484.

Smith, R.K. (2003) A Simple Model of the Hurricane Boundary Layer. *Quart. J. Roy. Met. Soc.*, **129**, 1007-1027.

Taylor, G.I. (1921) Diffusion processes by continuous movements, *Proc. Lond. Math. Soc.*, **20**(2), 196–211.

Taylor, G.I. (1938) The spectrum of turbulence, *Proc. R. Soc. Lond.*, Ser. A, **164**, 476–90.

Tenerelli, J.E., and S.S. Chen (2001), High-resolution Simulation of Hurricane Floyd (1999) Using MM5 with a Vortex-following Mesh Refinement. *Preprints, 18th Conference on Weather Analysis and Forecasting/14th Conference on Numerical Weather Prediction,* 30 July-2 August 2001, Ft. Lauderdale, Florida, AMS, J54-J56.

Trenberth, K.E., C.A. Davis, and J. Fasullo (2007) The Water and Energy Budgets of Hurricanes: Case Dtudies of Ivan and Katrina, *J. Geophys. Res.*, doi:10.1029/2006JD008303.

Tuleya, R.E., M. DeMaria, and J.R. Kuligowski (2007) Evaluation of GFDL and Simple Statistical Model Rainfall Forecasts for U.S. Landfalling Tropical Storms, *Wea. Forecasting*, **22**, 56–70.

Veneziano D. and A. Langousis (2009) Fractal Methods in Hydrology, In: *Advances in Data-based Approaches for Hydrologic Modeling and Forecasting*, Edited by: B. Sivakumar, World Scientific (under review).

Veneziano, D. and A. Langousis (2005a) The Areal Reduction Factor a Multifractal Analysis, *Wat. Resour. Res.*, **41**, doi:10.1029/2004WR003765.

Veneziano, D. and A. Langousis (2005b) The Maximum of Multifractal Cascades: Exact Distribution and Approximations, *Fractals*, **13**(4), 311-324.

Veneziano, D. and P. Furcolo (2003) Marginal Distribution of Stationary Multifractal Measures and their Haar Wavelet Coefficients, *Fractals,* **11**(3), 253-270.

Veneziano, D., A. Langousis and P. Furcolo (2006b) Multifractality and Rainfall Extremes: A Review, *Wat. Resour. Res.*, **42**, W06D15, doi:10.1029/2005WR004716.

Veneziano, D., C. Lepore, A. Langousis, and P. Furcolo (2007), Marginal Methods of Intensity-duration-frequency Estimation in Scaling and Non-scaling Rainfall, *Wat. Resour. Res.*, **43**, W10418, doi:10.1029/2007WR006040.

Veneziano, D., P. Furcolo and V. Iacobellis (2006a) Imperfect Scaling of Time and Space-Time Rainfall, *J. Hydrol.*, **322**(1-4), 105-119.

Vicente, G.A., R.A. Scofield and W.P. Menzel (1998) The Operational GOES Infrared Rainfall Estimation Technique, *Bull. Amer. Meteor. Soc.*, **79**, 1883–1898.

Vickery, P.J. and L.A. Twisdale (1995) Prediction of Hurricane Wind Speeds in the United States, *J. of Structural Engineering*, **121**(11), 1691-1699.

Vickery, P.J., P.F. Skerlj and L.A. Twisdale (2000) Simulation of Hurricane Risk in the U.S. Using Empirical Track Model, *J. of Structural Engineering*, **126**(10), 1222-1237.

Viltard, N., C. Burlaud, and C. Kummerow (2006) Rain Retrieval form TMI Brightness Temperature Measurements Using a TRMM PR – Based Data Base, *J. Applied Meteor. and Climat.*, **45**, 455-466.

Weisman, M.L., and J.B. Klemp (1986) Characteristics of Isolated Convective Storms, In: *Mesoscale Meteorology and Forecasting*, Edited by: Ray P.S., *Amer. Meteor. Soc.*, Boston, U.S.A.

Weiss, L.L. (1964) Ratio of True to Fixed-interval Maximum Rainfall, *J. Hydraul. Div.*, **90**(HY-1): 77-82.

Willoughby, H.E. (1990) Gradient Balance in Tropical Cyclones. *J. Atmos. Sci.*, **47**, 265-274.

Willoughby, H.E. (1991) Reply. *J. Atmos. Sci.*, **48**, 1209-1212.

Willoughby, H.E. and M.E. Rahn (2004) Parametric Representation of the Primary Hurricane Vortex. Part I: Observations and Evaluation of the Holland (1980) Model. *Mon. Wea. Rev.*, **132**, 3033-3048.

Willoughby, H.E., J.A. Clos, M.G. Shoreibah (1982) Concentric Eye Walls, Secondary Wind Maxima, and the Evolution of the Hurricane Vortex, *J. Atmo. Sci.*, **39**, 395-411.

Wilson, P.S., and R. Toumi (2005) A Fundamental Probability Distribution for Heavy Rainfall, *Geophys. Res. Lett.*, **32**, L14812, doi:10.1029/2005GL022465.

Wolff, D.B., D.A. Marks, E. Amitai, D.S. Silberstein, B.L. Fisher, A. Tokay, J. Wang and J.L. Pippitt (2005) Ground Validation for the Tropical Rainfall Measuring Mission (TRMM), *J. Atmos. Oceanic Technol.*, **22**, 365–380.

Young, B.C. and B.M. McEnroe (2003) Sampling Adjustment Factors for Rainfall Recorded at Fixed Time Intervals, Technical Notes, *J. Hydrol. Eng.*, **8**(5), 294-296.

Appendix A: Analytical Expressions for the Parameters in Equation (1.15)

Let $I_1=\int_0^\infty f^2\,d\eta$, $I_2=\int_0^\infty (1-g^2)\,d\eta$, $I_3=\int_0^\infty (1-g)\,d\eta$, $I_4=\int_0^\infty fg\,d\eta$, $I_5=\int_0^\infty f\,d\eta$ $I_6=\int_0^\infty (g^2-g)\,d\eta$ and $I_7=\int_0^\infty (1-g)^2\,d\eta$

where f and g are the functions given in equation (1.11). Then

$$\left.\frac{\partial f}{\partial \eta}\right|_{\eta=0}=a_2-a_1,\quad \left.\frac{\partial g}{\partial \eta}\right|_{\eta=0}=a_1-a_2$$
$$I_1=\frac{1}{8}(a_1^2+2a_1a_2+3a_2^2),\quad I_2=(a_1+a_2)-\frac{1}{8}(3a_1^2+2a_1a_2+a_2^2)$$
$$I_3=\frac{a_1+a_2}{2},\quad I_4=\frac{1}{8}(a_1^2+4a_1a_2+a_2^2)-\frac{a_1+a_2}{2} \tag{A.1}$$
$$I_5=-\frac{a_1+a_2}{2},\quad I_6=\frac{1}{8}(3a_1^2+2a_1a_2+a_2^2)-\frac{a_1+a_2}{2}$$
$$I_7=\frac{1}{8}(3a_1^2+2a_1a_2+a_2^2)$$

where a_1 and a_2 are calculated from equation (1.12). Under equation (A.1), the parameters A_1-A_{20} in equation (1.15) are given by

$$A_1=E^2[v_t^2\cos^2\theta\, I_7+(v_t\sin\theta-v_{gr})^2I_1+(I_5-I_4)(v_t^2\sin 2\theta-2v_tv_{gr}\cos\theta)] \tag{A.2}$$

$$A_2=E[(v_t^2\cos 2\theta+v_tv_{gr}\sin\theta)I_5+(½\,v_t^2\sin 2\theta-v_tv_{gr}\cos\theta)I_1+(v_{gr}^2-2v_tv_{gr}\sin\theta-v_t^2\cos 2\theta)I_4+ v_tv_{gr}I_6\cos\theta-½\,I_7v_t^2\sin 2\theta] \tag{A.3}$$

$$A_3=-v_t^2I_1\cos^2\theta+v_t^2I_5\sin 2\theta+(2v_tv_{gr}\cos\theta-v_t^2\sin 2\theta)I_4-v_t^2I_7\sin^2\theta+v_{gr}^2I_2+2v_tv_{gr}I_6\sin\theta \tag{A.4}$$

$$A_4=v_t^2I_1\cos^2\theta-v_t^2I_5\sin 2\theta+(v_t^2\sin 2\theta-2v_tv_{gr}\cos\theta)I_4+v_t^2I_7\sin^2\theta-2v_tv_{gr}I_6\sin\theta \tag{A.5}$$

$$A_5=v_tI_5\cos\theta+(v_{gr}-v_t\sin\theta)I_3 \tag{A.6}$$

$$A_6=E\left[v_t\cos\theta\left.\frac{\partial g}{\partial \eta}\right|_{\eta=0}+(v_{gr}-v_t\sin\theta)\left.\frac{\partial f}{\partial \eta}\right|_{\eta=0}\right] \tag{A.7}$$

$$A_7=E[(v_{gr}-v_t\sin\theta)I_5-v_tI_3\cos\theta],\quad A_8=-v_t\cos\theta\, I_5+v_tI_3\sin\theta \tag{A.8}$$

$$A_9=-v_t\cos\theta\left.\frac{\partial f}{\partial \eta}\right|_{\eta=0}+(v_{gr}-v_t\sin\theta)\left.\frac{\partial g}{\partial \eta}\right|_{\eta=0} \tag{A.9}$$

$$A_{10} = 2E[v_t^2 I_7 \cos^2\theta + I_1(v_{gr} - v_t \sin\theta)^2 + (v_t^2 \sin 2\theta - 2v_t v_{gr} \cos\theta)(I_5 - I_4)] \tag{A.10}$$

$$A_{11} = E^2\Bigg[v_t^2 \cos^2\theta \frac{\partial I_7}{\partial r} - 2I_1(v_t \sin\theta - v_{gr}) \frac{\partial v_{gr}}{\partial r} + (v_{gr} - v_t \sin\theta)^2 \frac{\partial I_1}{\partial r} - 2v_t(I_5 - I_4)\frac{\partial v_{gr}}{\partial r} \cos\theta + (v_t^2 \sin 2\theta - 2v_t v_{gr} \cos\theta) \frac{\partial (I_5 - I_4)}{\partial r} \Bigg] \tag{A.11}$$

$$A_{12} = (v_t^2 \cos 2\theta + v_t v_{gr} \sin\theta) I_5 + (\tfrac{1}{2} v_t^2 \sin 2\theta - v_t v_{gr} \cos\theta) I_1 + (v_{gr}^2 - 2v_t v_{gr} \sin\theta - v_t^2 \cos 2\theta) I_4 + v_t v_{gr} I_6 \cos\theta - \tfrac{1}{2} v_t^2 I_7 \sin 2\theta \tag{A.12}$$

$$A_{13} = E\Bigg[(-2v_t^2 \sin 2\theta + v_t v_{gr} \cos\theta) I_5 + (v_t^2 \cos 2\theta + v_t v_{gr} \sin\theta) \left(\frac{\partial I_5}{\partial\theta} + I_1 \right) + (\tfrac{1}{2} v_t^2 \sin 2\theta - v_t v_{gr} \cos\theta) \frac{\partial I_1}{\partial\theta} + (2v_t^2 \sin 2\theta - 2v_t v_{gr} \cos\theta) I_4 + (v_{gr}^2 - 2v_t v_{gr} \sin\theta - v_t^2 \cos 2\theta) \frac{\partial I_4}{\partial\theta} - v_t v_{gr} I_6 \sin\theta + v_t v_{gr} \cos\theta \frac{\partial I_6}{\partial\theta} - v_t^2 I_7 \cos 2\theta - \tfrac{1}{2} v_t^2 \sin 2\theta \frac{\partial I_7}{\partial\theta} \Bigg] \tag{A.13}$$

$$A_{14} = E\Bigg[v_t \sin\theta\, I_5 \frac{\partial v_{gr}}{\partial r} + (v_t^2 \cos 2\theta + v_t v_{gr} \sin\theta) \frac{\partial I_5}{\partial r} - v_t \frac{\partial v_{gr}}{\partial r} I_1 \cos\theta + (\tfrac{1}{2} v_t^2 \sin 2\theta - v_t v_{gr} \cos\theta) \frac{\partial I_1}{\partial r} + 2I_4(v_{gr} - v_t \sin\theta) \frac{\partial v_{gr}}{\partial r} + I_6 v_t \cos\theta \frac{\partial v_{gr}}{\partial r} + (v_{gr}^2 - 2v_t v_{gr} \sin\theta - v_t^2 \cos 2\theta) \frac{\partial I_4}{\partial r} + v_t v_{gr} \cos\theta \frac{\partial I_6}{\partial r} - \tfrac{1}{2} v_t^2 \sin 2\theta \frac{\partial I_7}{\partial r} \Bigg] \tag{A.14}$$

$$A_{15} = -v_t^2 I_1 \sin 2\theta + v_t^2 \cos^2\theta \frac{\partial I_1}{\partial\theta} - 2v_t^2 I_5 \cos 2\theta - v_t^2 \sin 2\theta \frac{\partial I_5}{\partial\theta} + (2v_t^2 \cos 2\theta + 2v_t v_{gr} \sin\theta) I_4 + (v_t^2 \sin 2\theta - 2v_t v_{gr} \cos\theta) \frac{\partial I_4}{\partial\theta} + v_t^2 I_7 \sin 2\theta + v_t^2 \sin^2\theta \frac{\partial I_7}{\partial\theta} - 2v_t v_{gr} I_6 \cos\theta - 2v_t v_{gr} \sin\theta \frac{\partial I_6}{\partial\theta} \tag{A.15}$$

$$A_{16} = (v_{gr} - v_t \sin\theta) I_5 - v_t I_3 \cos\theta \tag{A.16}$$

$$A_{17} = E\left[I_5 \frac{\partial v_{gr}}{\partial r} + (v_{gr} - v_t \sin\theta) \frac{\partial I_5}{\partial r} - v_t \cos\theta \frac{\partial I_3}{\partial r} \right] \tag{A.17}$$

$$A_{18} = v_t I_5 \sin\theta - v_t \cos\theta \frac{\partial I_5}{\partial\theta} + v_t I_3 \cos\theta + v_t \sin\theta \frac{\partial I_3}{\partial\theta} \tag{A.18}$$

$$A_{19} = v_{gr}^{\,2} I_6, \; A_{20} = v_{gr} \frac{\partial I_6}{\partial \theta} \tag{A.19}$$

In equations (A.2)-(A.19), the derivatives $\frac{\partial I_j}{\partial r}$ and $\frac{\partial I_j}{\partial \theta}$ for $j = 1,..,7$ can be calculated analytically using the chain rule

$$\frac{\partial I_j}{\partial s} = \frac{\partial I_j}{\partial a_1}\frac{\partial a_1}{\partial s} + \frac{\partial I_j}{\partial a_2}\frac{\partial a_2}{\partial s}, \quad j=1,..,7 \tag{A.20}$$

where s is either r or θ and $\frac{\partial a_1}{\partial s}$ and $\frac{\partial a_2}{\partial s}$ can be analytically derived from equations (1.12) and (1.13).

Appendix B: Alternative Methods to Calculate the Distribution of the Amplification Factor $\gamma_{l,max}$

In Section 3.3.2 we used data on $\gamma_{l,max}$ to fit a theoretical distribution model for the amplification factor. Alternatively, one can evaluate the distribution of $\gamma_{l,max}$ by studying the maximum of the moving average process $I_l(x)$ illustrated in Figure 3.2.

Here we develop two alternative approaches for the distribution of $\gamma_{l,max}$ starting from the ratio γ_l, defined as

$$\gamma_l = \frac{I_l}{I_L} \ , \ l \leq L \tag{B.1}$$

where I_l is obtained by continuously averaging the PR rainrate along a cross section C (see Figure 3.1) using a window of length l and $I_L = I_{l=L}$.

The distribution of $\gamma_{l,max}$ is calculated from the distribution of γ_l under the assumption of independence and then corrected for dependence and continuous sampling; see Sections B.1 and B.2. Since we calculate the distribution of the maximum amplification factor $\gamma_{l,max}$ starting from a marginal distribution (i.e. the distribution of γ_l), we refer to those approaches as the "marginal approaches". The approach in Section 3.3.2 is referred to as the "maxima approach". Section B.3 compares results on the total amplification factor $\beta_{l,max}$ in equation (3.2), as well as calculated IDF values for New Orleans using the three approaches for $\gamma_{l,max}$.

B.1 Marginal Approach Using a Modified-beta Distribution Model

We start by calculating the empirical moments of the ratio γ_l in equation (B.1) using the frames in Table 3.1.

Figure B.1 shows plots of $\ln E[(\gamma_l)^q]$ against $\ln l$ for $q = 0, 1, 2, 3$, for the same categories of the large-scale intensity I_L as in Figure 3.8. One sees that the variability of the rainfall field, expressed here through $\ln E[(\gamma_l)^q]$ for $q > 1$, increases with decreasing spatial scale l and large-scale rainfall intensity I_L. This is in accordance to what we found in Section 3.3.2 when we studied the moments of the amplification factor $\gamma_{l,max}$. An additional observation one makes from Figure B.1 is that an important contributor to the increased variability at low I_L regions is the intermittency of the rainfall process.

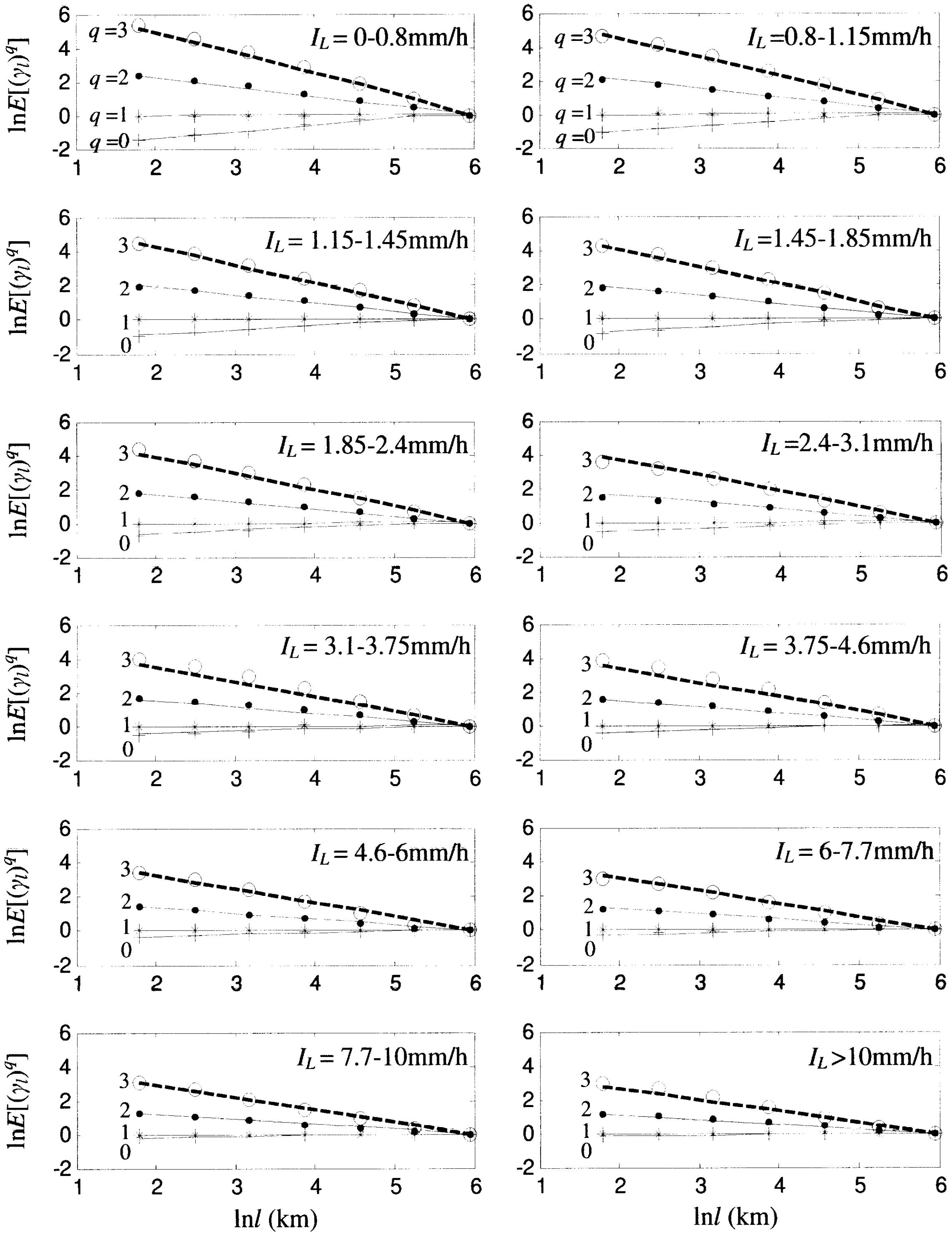

Figure B.1: Plots of $\ln E[(\gamma_l)^q]$ against $\ln l$ for $q = 0, 1, 2, 3$, for the same categories of I_L as in Figure 3.8. The markers indicate empirical moment values, whereas the solid lines correspond to the parametric fits in equation (B.2). The solid dashed lines correspond to the theoretical third moments calculated from the distribution in equation (B.9); see text for details.

The latter is expressed through the probability $P_0 = 1 - E[(\gamma_l)^0]$ that an interval of size l is dry. One sees that P_0 increases with decreasing I_L. Since lower values of I_L are associated with larger distances y from the storm center, one concludes that the outer TC environment is more lacunar and exhibits more cellular structure and higher small-scale variability relative to the inner region. This is in accordance with the findings of other studies on the spatial variability of TC rainfall; see e.g. Molinari *et al.* (1994) and Lonfat *et al.* (2004).

For each intensity category I_L, we use the method of least squares to fit linear expressions to the logs of the 0th, 1st and 2nd initial moments of γ_l:

$$\ln E[(\gamma_l)^q] = \begin{cases} b_q \ln\left(\frac{c_q}{l}\right) & , \; l \le c_q \\ 0 & , \; l > c_q \end{cases} \tag{B.2}$$

where l is in km and b_q and c_q (q = 0, 1, 2) are parameters. The intercept of the log-linear expressions is equation (B.2), c_q, is set to 220km for $q = 0$ and to 384km for $q = 1$ and 2. The former value of c_q is the average of the 0th moment intercepts from all I_L categories, whereas the latter corresponds to the maximum scale L used in the analysis.

Figure B.2 shows how the parameters b_q (q = 0, 1, 2) in equation (B.2) vary with the large-scale intensity I_L. The solid lines in Figure B.2 are smooth least-squares estimates of b_q (q = 0, 1, 2).

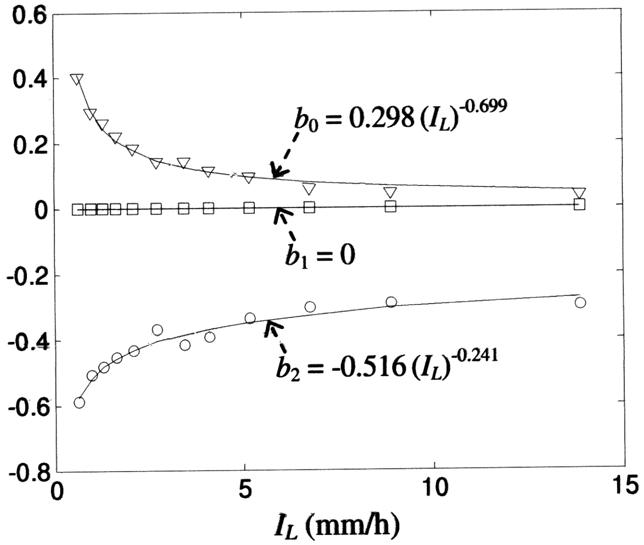

Figure B.2: Plots of the parameters b_0-b_2 in equation (B.2) against I_L. Solid lines are smooth least-squares estimates.

B.1.1 Distribution of γ_l

The distribution of γ_l has unit mean (see Figure B.1), it is bounded between 0 and L/l and has concentrated masses at zero: $P[\gamma_l = 0] = P_0 = 1 - E[(\gamma_l)^0]$ and at L/l: $P[\gamma_l = L/l]$. $\gamma_l = 0$ corresponds to the case of no rainfall inside an interval of size l, whereas $\gamma_l = L/l$ to the case when all rainfall volume is concentrated inside one l interval. By assuming independence between different l intervals, one obtains an estimate of the probability mass at L/l: $P[\gamma_l = L/l] = (P_0)^{L/l-1}$. In this case, the mean value m_c and variance σ_c^2 of the conditional variable $(\gamma_l|\gamma_l \neq 0, L/l)$ are calculated to be:

$$\begin{aligned} m_c &= 1 + \frac{P_0 - (L/l-1)(P_0)^{L/l-1}}{1 - P_0 - (P_0)^{L/l-1}} \\ \sigma_c^2 &= \frac{E[(\gamma_l)^2] - 1 + (m_c-1)^2 - P_0\, m_c^2 - (L/l - m_c)^2 (P_0)^{L/l-1}}{1 - P_0 - (P_0)^{L/l-1}} \end{aligned} \qquad \text{(B.3)}$$

where P_0 and $E[(\gamma_l)^2]$ can be obtained from equation (B.2) and the parametric expressions in Figure B.2, as functions of the spatial scale l and the large-scale rainfall intensity I_L.

We approximate the conditional distribution of $(\gamma_l|\gamma_l \neq 0, L/l)$ by using a beta distribution. In this case the cumulative distribution function (CDF) of γ_l is given by

$$F_{\gamma_l}(\gamma) = \begin{cases} P_0 & , \ \gamma = 0 \\ P_0 + (1 - P_0 - P_0^{L/l-1}) F_X\left(\frac{l\gamma}{L}\right) & , \ 0 < \gamma < L/l \\ 1 & , \ \gamma \geq L/l \end{cases} \qquad \text{(B.4)}$$

where F_X is a standard beta distribution in [0,1] with mean value $m_X = m_c\, l/L$ and variance $\sigma_X^2 = (\sigma_c\, l/L)^2$.

Figure B.3 compares the empirical CDF of γ at different spatial scales l with those obtained theoretically by fitting the distribution model in equation (B.4) to the 0th, 1st and 2nd initial moments obtained from equation (B.2). Comparison is done for the lowest (I_L= 0-0.8mm/h) and highest (I_L>10mm/h) intensity categories in Figure B.1.

The distribution model in equation (B.4) produces good analytical fits to the empirical distribution of γ. Equally good fits have been obtained for all other intensity categories and spatial scales l. This is evident from Figure B.1, where we show the theoretical third moment of the distribution in equation (B.4) (thick dashed lines) when fitted to the 0th, 1st and 2nd initial moments obtained from equation (B.2). The fact that the theoretical and empirical 3rd initial moments are close shows that the distribution in equation (B.4) produces good analytical fits to the distribution of γ_l.

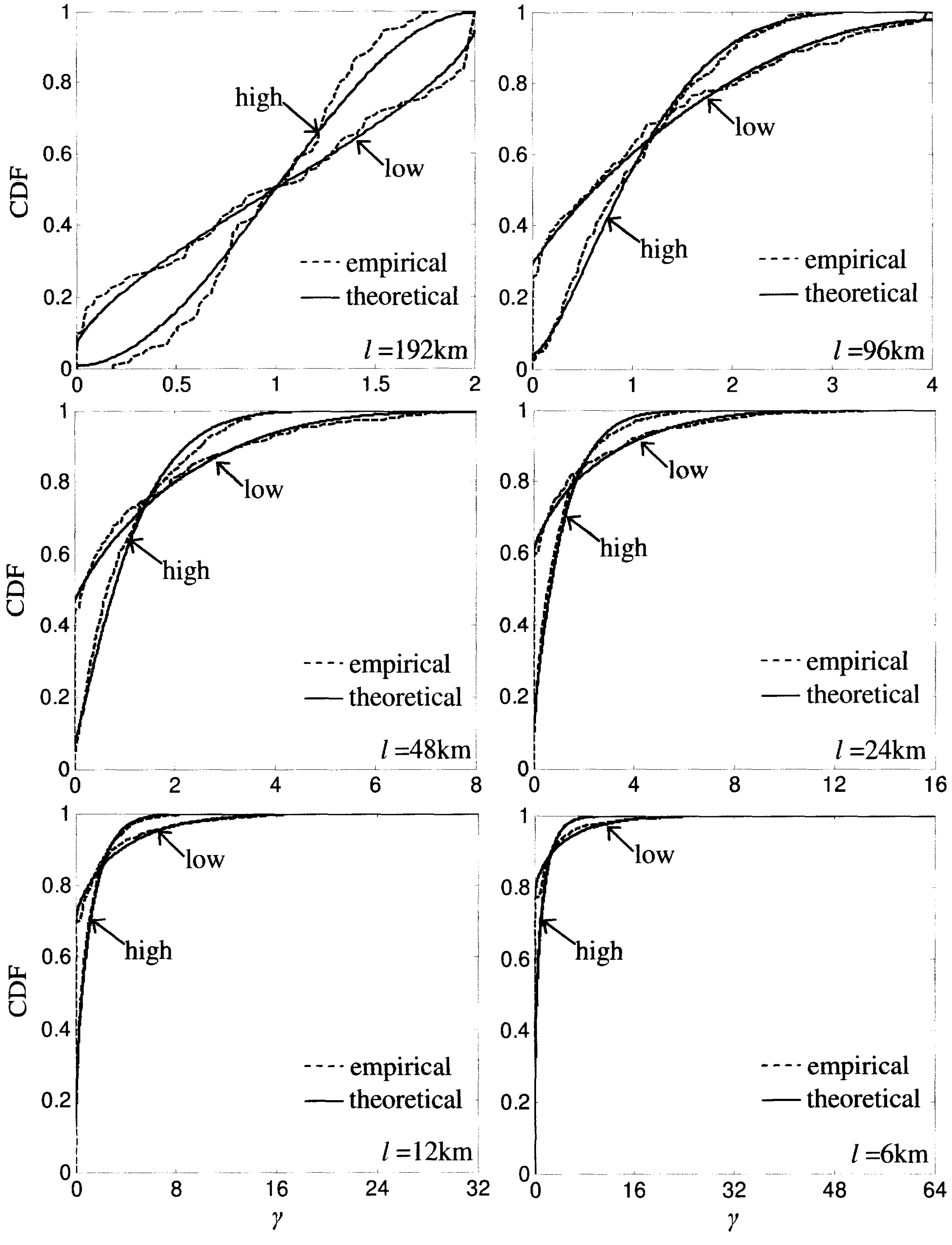

Figure B.3: Comparison between the empirical and theoretical CDFs of the ratios γ_l at different spatial scales l. Comparison is done for the lowest (I_L = 0-0.8mm/h) and highest (I_L>10mm/h) intensity categories in Figure B.1.

B.1.2 Distribution of $\gamma_{l,max}$

With corrections to be made latter, we approximate $\gamma_{l,max}$ in equation (3.6) by $\gamma_{l,max,ind}$, the maximum of L/l independent copies of γ_l. In this case

$$F_{\gamma_{l,max,ind}}(\gamma) = [F_{\gamma_l}(\gamma)]^{L/l} \quad , \quad \gamma \geq 0 \tag{B.5}$$

$\gamma_{l,max,ind}$ is biased relative to $\gamma_{l,max}$ in two respects. The first is that, by definition [equation (B.1)], the variables $\gamma_{l,i}$ for $i = 1, \ldots, L/l$ are dependent and average to 1:

$$\frac{l}{L}\sum_{i=1}^{L/l} \gamma_{l,i} = \frac{l}{L}\sum_{i=1}^{L/l} \frac{I_{l,i}}{I_L} = 1 \tag{B.6}$$

The second source of bias is that $\gamma_{l,max}$ in equation (3.6) is the maximum amplification factor obtained by continuously scanning each cross section of length L using an averaging window of size l, whereas equation (B.5) considers non-overlapping intervals.

To quantify the two sources of bias, Figures B.4 and B.5 show the empirical distribution of $\gamma_{l,max}$ at spatial scale l =192km obtained: as the maximum of two non-overlapping intervals of size l=192km (Figure B.4), and by continuously scanning each cross section of length L =384km using an averaging window of size l=192km (Figure B.5). Results are shown for the 12 intensity categories in Figure B.1.

The dotted lines in Figures B.4 and B.5 denote the theoretical PDF of $\gamma_{l,max,ind}$ under independence [equation (B.5)], whereas the solid blue lines show the exact PDF of the maximum of two dependent random variables $\gamma_{L/2}$ with marginal distribution given by equation (B.4) that satisfy $\gamma_{L/2}(1) + \gamma_{L/2}(2) = 2$. For the latter, one obtains

$$F_{\max\{\gamma_{L/2}(1),\, \gamma_{L/2}(2)\}}(z) = \begin{cases} 0 & , \; z < 1 \\ 2F_{\gamma_{L/2}}(z) - 1 & , \; z \geq 1 \end{cases} \tag{B.7}$$

One sees that $\gamma_{l,max,ind}$ fails to reproduce the distribution of $\gamma_{l,max}$ in both cases of non-overlaping intervals (Figure B.4) and continuous sampling (Figure B.5). Note in particular that the effect of dependence causes the distribution of $\gamma_{l,max}$ to have a lower bound at 1 (this corresponds to a uniform rainfall inside L), whereas $\gamma_{l,max,ind}$ is bounded at 0. The exact theoretical distribution in equation (B.7) resembles well the empirical distribution $\gamma_{l,max}$ for the case of non-overlaping intervals (see Figure B.4), but underestimates the maxima under continuous sampling (see Figure B.5).

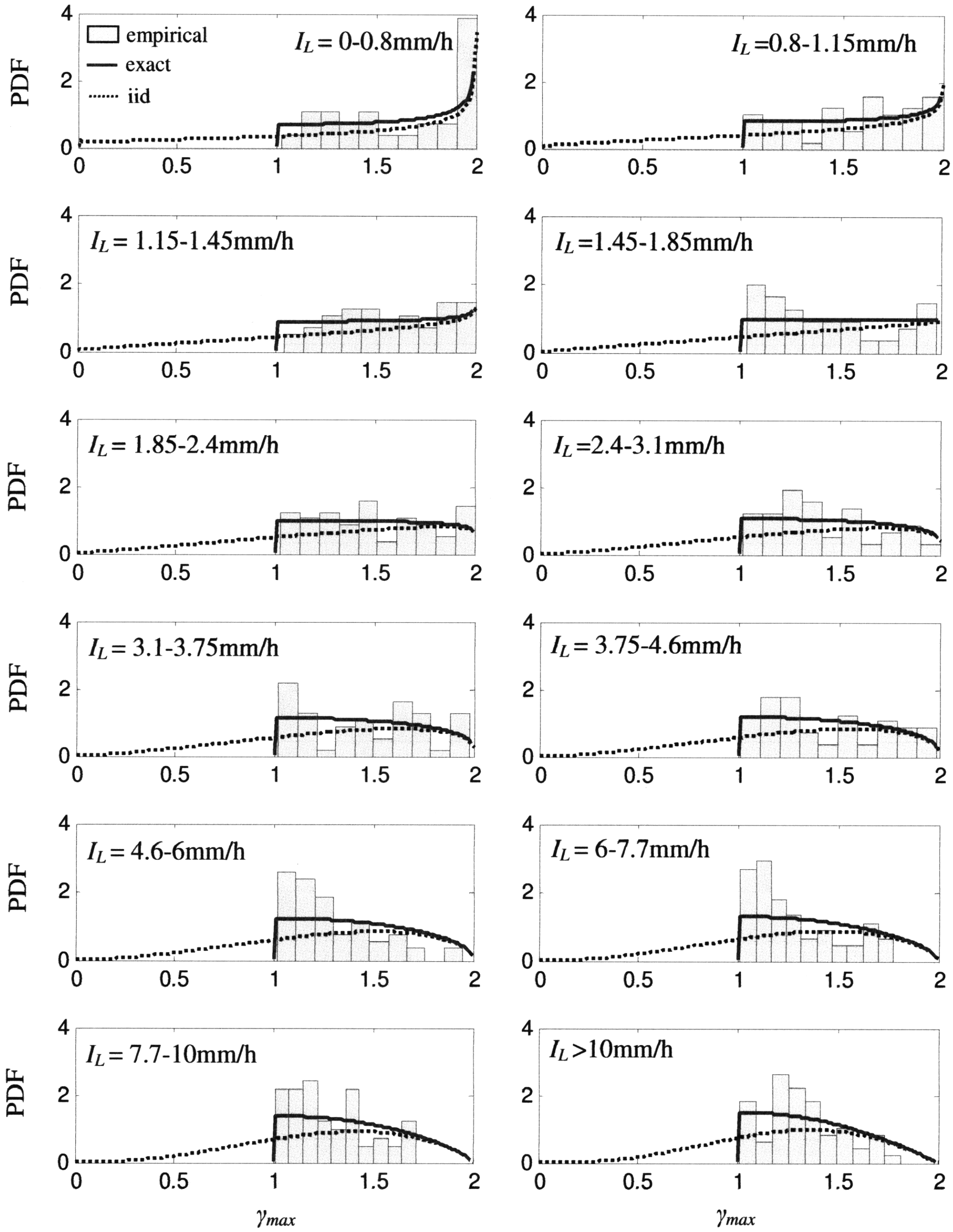

Figure B.4: Comparison of the empirical distribution of $\gamma_{l,max}$ obtained for the case of two non-overlaping intervals of size l =192km, and those calculated theoretically under independence [dotted lines; equation (B.5)] and including dependence [solid blue lines; equation (B.7)]. Comparison is done for the intensity categories in Figure B.1.

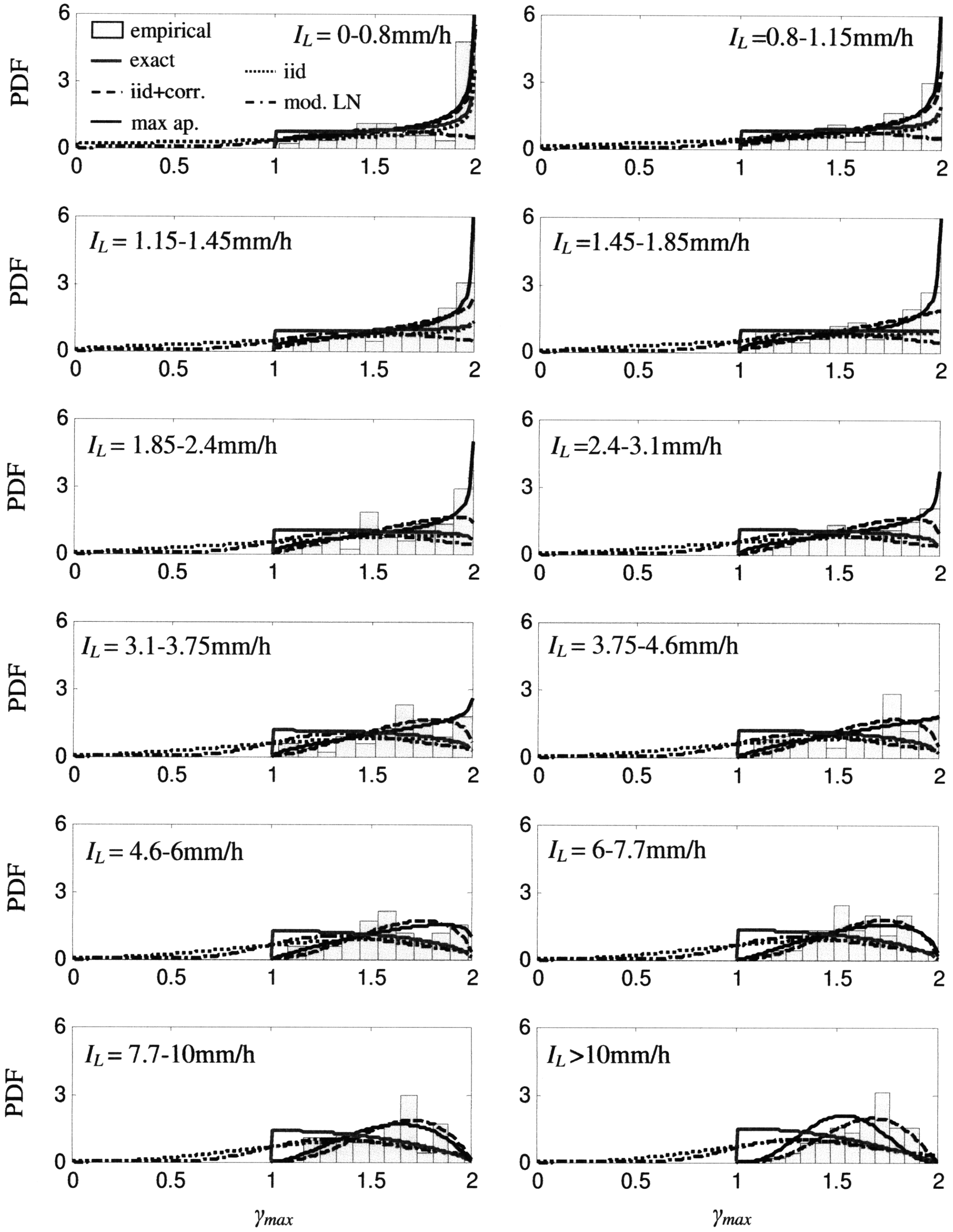

Figure B.5: Comparison of the empirical distribution of $\gamma_{l,max}$ obtained for the case of continuous sampling using a sliding window of size l =192km, and those calculated theoretically under independence [dotted lines; equation (B.5)], including dependence [solid blue lines; equation (B.7)], using the linear correction in equation (B.9) (dashed lines), using the maxima approach described in Section 3.3.2 [solid black lines; equation (3.8)] and using the marginal approach with a modified lognormal (LN) distribution described in Section B.2 (dashed-dotted lines). Comparison is done for the intensity categories in Figure B.1.

To correct the distribution of $\gamma_{l,max,ind}$ for the effects of dependence and continuous sampling, we use a linear transformation to rescale the CDF in equation (B.5) so it is bounded between 1 and L/l. Specifically we take

$$\gamma_{l,max,corr}=1+\frac{L/l-1}{L/l}\,\gamma_{l,max,ind} \tag{B.8}$$

The distribution of $\gamma_{l,max,corr}$ is given by

$$F_{\gamma_{l,max,corr}}(\gamma)\approx\begin{cases}\left[F_{\gamma_l}\left(\dfrac{(\gamma-1)L}{L-l}\right)\right]^{L/l} & ,\ \gamma\geq 1 \text{ and } l<L\\ F_{\gamma_l}(\gamma) & ,\ \gamma\geq 0 \text{ and } l=L\end{cases} \tag{B.9}$$

For γ >>1 and L/l large (say >10) the models in equations (B.5) and (B.9) produce similar results.

The dashed lines in Figure B.5 show the probability density function of $\gamma_{l,max,corr}$ calculated from equation (B.9) for the case of l =192km, whereas the solid black lines show the distribution of $\gamma_{l,max}$ using the maxima approach with a beta distribution model described in Section 3.3.2. Figures B.6 -B.8 make similar comparisons for l=96, 48 and 6km. One sees that the theoretical model of equation (B.9) reproduces well the empirical PDF of $\gamma_{l,max}$ for different spatial scales l and large-scale average intensities I_L and produces results close to those obtained using the maxima approach in Section 3.3.2.

Figure B.9 compares theoretically calculated exceedance probabilities of rainfall maxima at different spatial scales l to observed relative frequencies. It was generated using the procedure in Section 3.4 with $\gamma_{l,max}$ calculated from equations (B.9) and (B.4) and the parametric expressions in equation (B.2) and Figure B.2. The fact that all histograms are nearly uniform validates the model in the sense that observed relative frequencies are close to theoretically calculated probabilities.

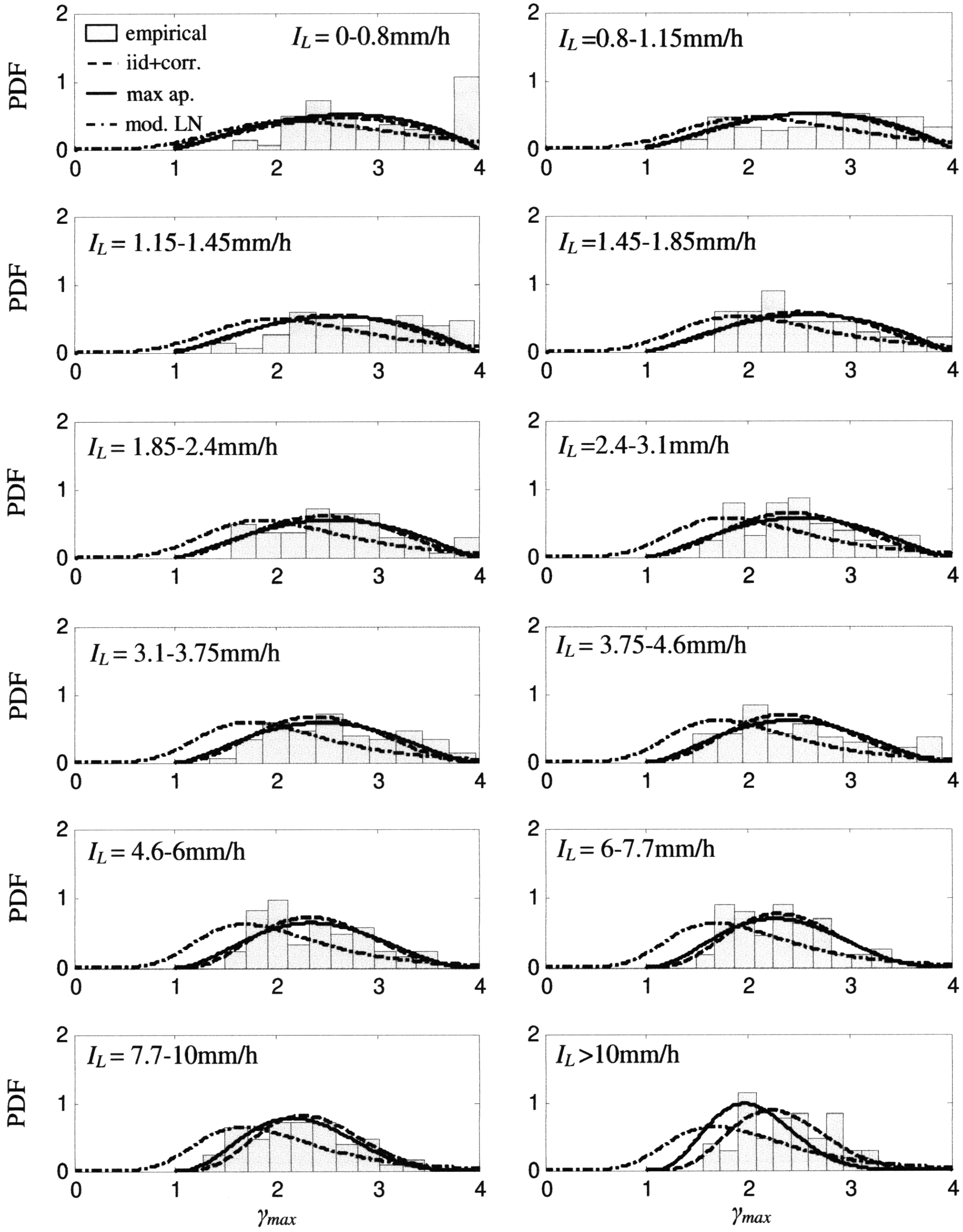

Figure B.6: Comparison of the empirical distribution of $\gamma_{l,max}$ obtained for the case of continuous sampling using a sliding window of size $l = 96$km, and those calculated theoretically using the linear correction in equation (B.9) (dashed lines), using the maxima approach described in Section 3.3.2 [solid lines; equation (3.8)] and using the marginal approach with a modified lognormal (LN) distribution described in Section B.2 (dashed-dotted lines). Comparison is done for the intensity categories in Figure B.1.

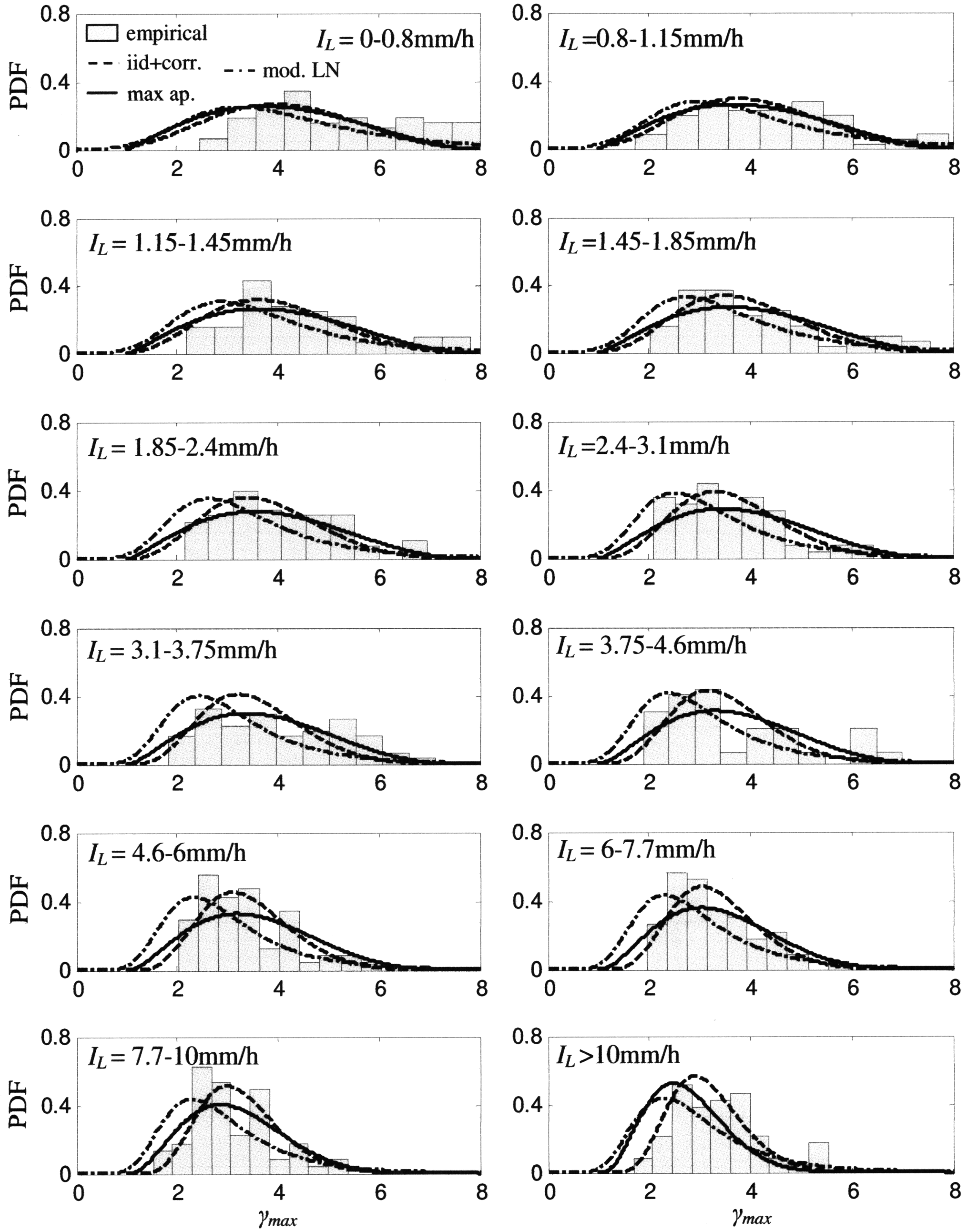

Figure B.7: Same as Figure B.6 but for l = 48km

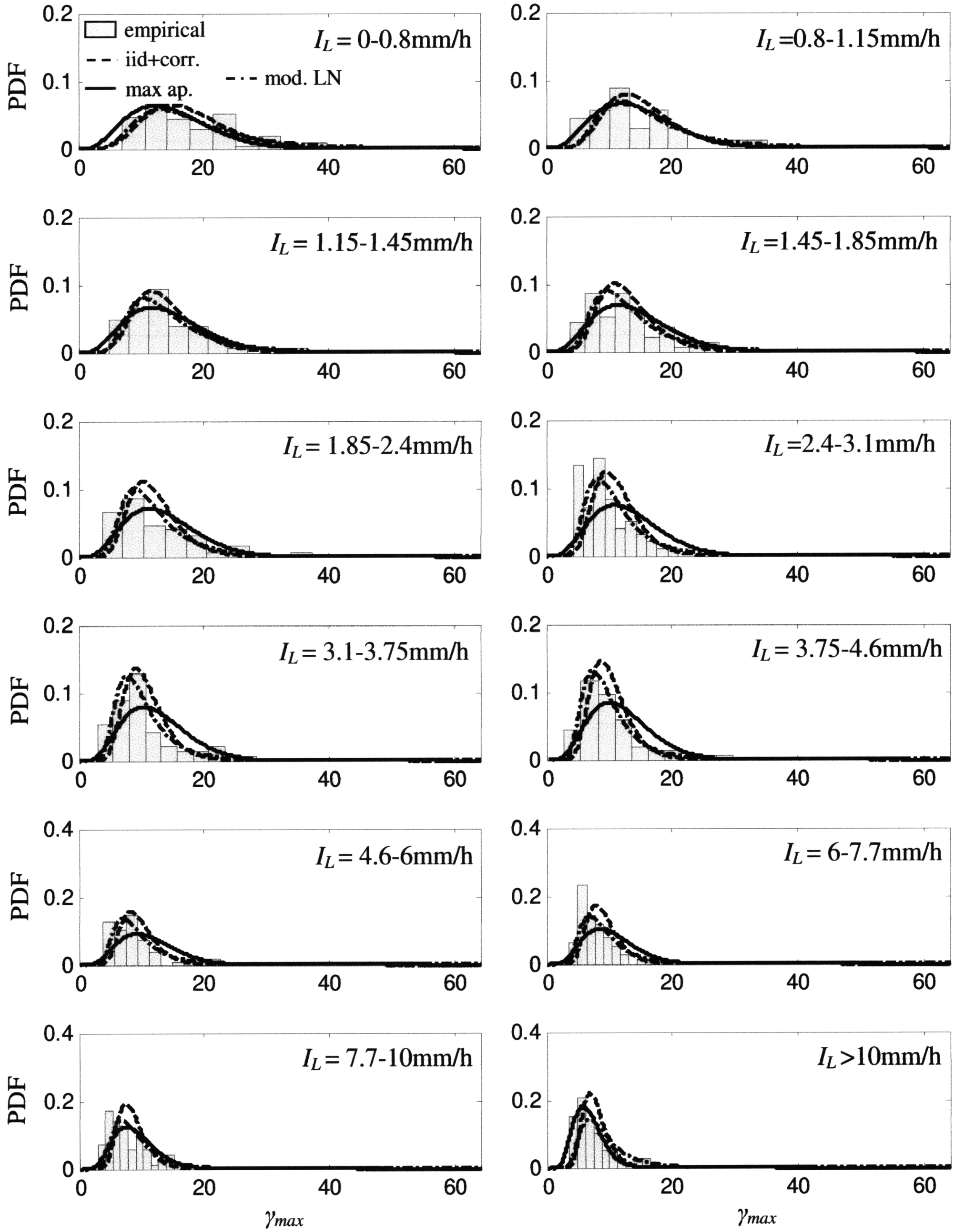

Figure B.8: Same as Figure B.6 but for l = 6km.

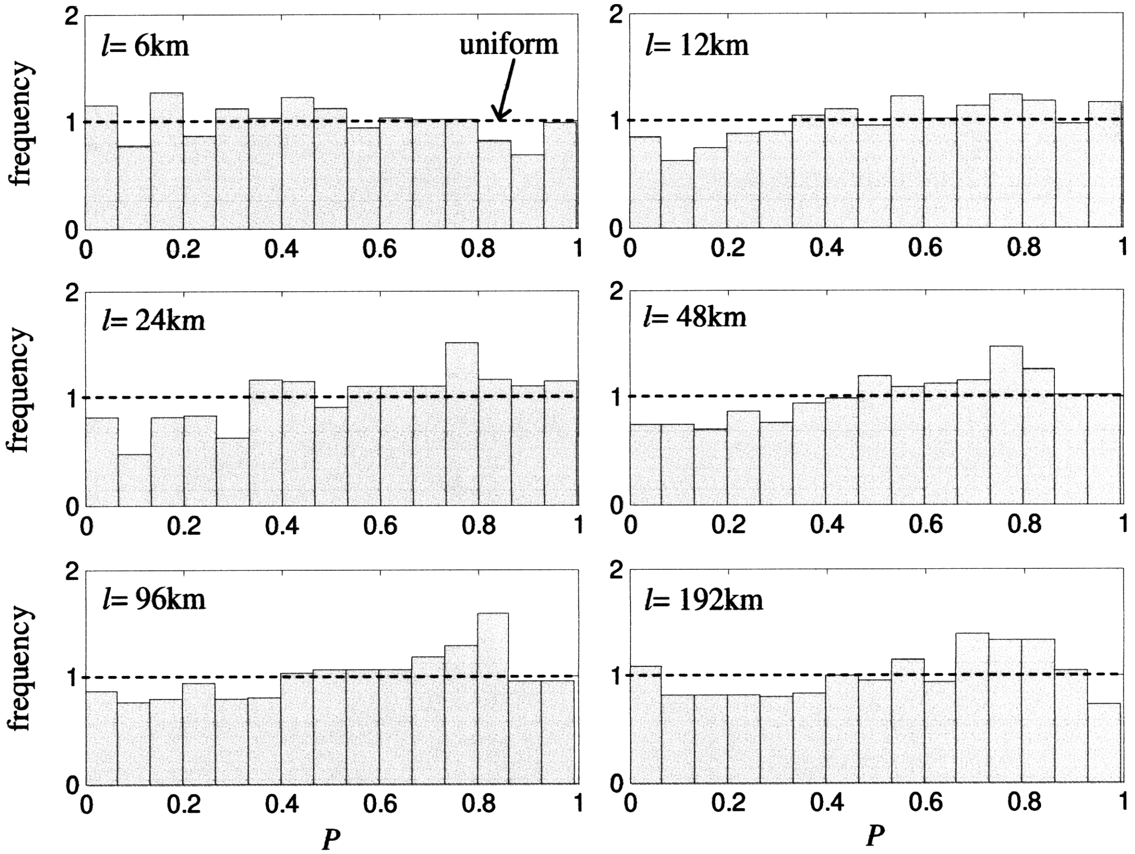

Figure B.9: Histogram of the non-exceedance probability P in equation (3.10) for different spatial scales l. $\gamma_{l,max}$ is calculated from equations (B.9) and (B.4) and the parametric expressions in equation (B.2) and Figure B.2. Each histogram is based on a sample of size 789.

B.2 A Simpler Marginal Approach Using a Modified-lognormal Distribution Model

Figure B.1 shows that, for all categories of the large-scale intensity I_L, the moments of γ_l vary with scale l in an approximately log-linear way. This observation allows one to simplify the marginal model developed in Section B.1 using concepts from the theory of multifractal cascades. To do so, we employ standard probability techniques with a minimum of multifractal formalism. This makes the approach more transparent than using multifractal concepts like dressed and bare densities, singularities and their fractal dimensions; although the latter tools are more elegant and general. For more details on multifractal measures and models, the reader is referred to Schertzer and Lovejoy (1987), Gupta and Waymire (1993), Lovejoy and Schertzer (1995), Veneziano and Langousis (2005a,b, 2009), Langousis and Veneziano (2007) and Langousis *et al.* (2007).

Define random variable S_l such that

$$E[(S_l)^q]=\left(\frac{L}{l}\right)^{K(q)} \tag{B.10}$$

Up to a maximum scale L (in our case L=384km), the moments of S_l vary with l in a log-linear way with slope $K(q)$ that depends on the moment order q.

In what follows we model S_l using a modified lognormal (LN) distribution with unit mean. In particular, S_l has a probability mass P_0 at 0: $P[S_l=0]=P_0=1-(L/l)^{-C_b}$ and $(S_l|S_l>0)$ has lognormal distribution with log-mean $m_{LN}=(C_b-C_{LN})\ln(L/l)$ and log-variance $\sigma_{LN}^2=2C_{LN}\ln(L/l)$ where C_b and C_{LN} are parameters. C_b controls the lacunarity of the rainfall field (i.e. duration of wet and dry periods), whereas C_{LN} controls the amplitude of the fluctuations when it rains. In this case the log-log slope of the moments, $K(q)$, is given by

$$K(q)=C_b(q-1)+C_{LN}(q^2-q) \tag{B.11}$$

We call this distribution of S_l a modified lognormal (LN) distribution with cumulative distribution function (CDF)

$$F_{S_l}(s)=\begin{cases} P_0+(1-P_0)\Phi\left(\frac{\ln s-m_{LN}}{\sigma_{LN}}\right) & , \ s>0 \\ P_0 & , \ s=0 \end{cases} \tag{B.12}$$

where Φ is the standard normal CDF. The distribution in equation (B.12) has been extensively used in the past for developing scaling representations of rainfall using the notion of multiplicative cascades; see e.g. Over and Gupta (1996); Schmitt *et al.* (1998); Langousis and Veneziano (2007), Langousis *et al.* (2007) and Veneziano *et al.* (2007).

An important difference between the distribution of S_l in equation (B.12) and that of γ_l in equation (B.4) is that the former does not have an upper bound, whereas the latter is upper bounded at L/l. In the multifractal literature this difference is referred to as the effect of "dressing" (see e.g. Schertzer and Lovejoy, 1987; Veneziano and Furcolo, 2003; Langousis and Veneziano, 2007), which is an alternative way of saying that random variable γ_l accounts for rainfall variability at scales smaller than l whereas S_l does not. Since random variable S_l does not have an upper bound, one expects equation (B.12) to produce better fits to the empirical ratios γ_l as the resolution L/l increases; see also discussion on Figures B.5 - B.8 below.

We allow the parameters C_b and C_{LN} of the modified lognormal distribution in equation (B.12) to depend on the large-scale rainfall intensity I_L. In particular, for each intensity category

I_L in Figure B.1, we use the method of least squares to fit equation (B.10) to the 2nd and 3rd initial moments of γ_l. The obtained slopes $K(2)$ and $K(3)$ and equation (B.11) are then used to calculate the parameters C_b and C_{LN}:

$$C_b = 3K(2)\text{-}K(3)\ ,\ C_{LN} = \frac{K(3)\text{-}2K(2)}{2} \tag{B.13}$$

We select to fit the 2nd and 3rd empirical moments for two reasons. The first reason is that a number of studies (Veneziano *et al.*, 2006b, 2007; Langousis and Veneziano, 2007; Langousis *et al.*, 2007) have shown that when modeling extremes of point rainfall, it is important to focus on moment orders larger than 2. The other reason is that the empirical moments of order larger than 3.5-4 tend to underestimate the true moments due to sample limitations (Ossiander and Waymire, 2000, 2002; Veneziano *et al.*, 2006b). Note, however, that similar findings on the variation of C_b and C_{LN} with I_L (see below) where obtained also when fitting the 0th and 2nd moments of the empirical data.

Figure B.10 shows how the parameters of the modified lognormal model vary with the large-scale rainfall intensity I_L. The solid lines are smooth least-squares estimates. C_b decreases exponentially with I_L. This is in accordance with the observed increase of the fraction of dry regions with increasing distance from the center of the storm; see Section B.1. C_{LN} is approximately constant equal to 0.08. Values of C_{LN} around 0.1 have also been reported by studies on extra-tropical rainfall; see e.g. Langousis and Veneziano (2007) and Veneziano *et al.* (2007).

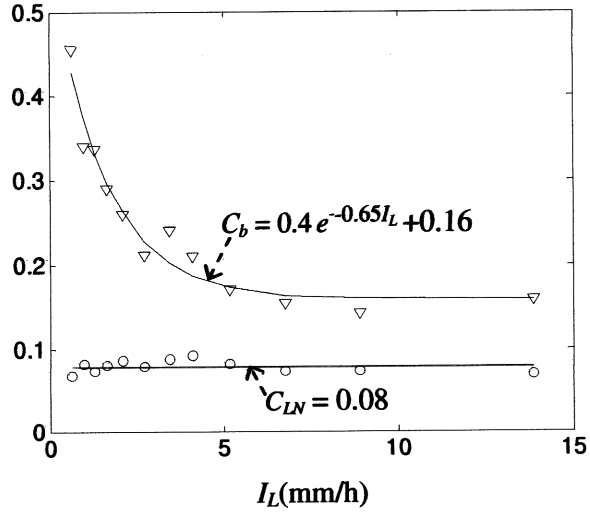

Figure B.10: Plots of the parameters C_b and C_{LN} against I_L. The solid lines are least-squares fits.

B.2.1 Distribution of $\gamma_{l,max}$

From equation (B.12) one can derive the CDF of $\gamma_{l,max,ind}$, the maximum of L/l independent copies of S_l. One obtains

$$F_{\gamma_{l,max,ind}}(\gamma)=\begin{cases}\left[P_0+(1-P_0)\Phi\left(\dfrac{\ln\gamma-m_{LN}}{\sigma_{LN}}\right)\right]^{L/l} & ,\ \gamma>0\\ P_0^{\,L/l} & ,\ \gamma=0\end{cases} \qquad (B.14)$$

where m_{LN} = $(C_b\text{-}C_{LN})$ $\ln(L/l)$ and σ_{LN}^2= $2C_{LN}$ $\ln(L/l)$ can be obtained from Figure B.10 as functions of I_L.

As discussed in the previous section, $\gamma_{l,max,ind}$ is biased relative to $\gamma_{l,max}$ by the assumption that maximum rainfall occurs in one of the non-overlapping intervals of size l. In the case considered here, the maxima distribution in equation (B.14) is obtained from a modified lognormal marginal distribution, for which the classical way to eliminate this source of bias is to multiply $\gamma_{l,max,ind}$ by a continuity correction factor $\delta\approx$ 1.13-1.15; see Hershfield (1961), Weiss (1964), Young and McEnroe (2003) and Veneziano *et al.* (2007). After corrected for continuity, equation (B.14) becomes

$$F_{\gamma_{l,max,corr}}(\gamma)=\begin{cases}\left[P_0+(1-P_0)\Phi\left(\dfrac{\ln(\gamma/\delta)-m_{LN}}{\sigma_{LN}}\right)\right]^{L/l} & ,\ \gamma>0\\ P_0^{\,L/l} & ,\ \gamma=0\end{cases} \qquad (B.15)$$

The dashed dotted lines in Figures B.5 - B.8 show the probability density function of $\gamma_{l,max,corr}$ calculated from equation (B.15) for l =192, 96, 48 and 6km. One sees that the probability model in equation (B.15) produces results close to those obtained from equation (B.9) only for spatial scales $l \leq$48km or, equivalently, resolutions $L/l \geq 4$. This makes sense since the variable $\gamma_{l,max,corr}$ in equation (B.15) does not include dependencies between rainfall amounts inside different l intervals and, in addition, it does not account for rainfall variability at scales smaller than l. The first source of bias causes the distribution in equation (B.15) to have a lower bound at zero, whereas the second source of bias results in a distribution that does not have an upper bound. Note that the distribution model in equation (B.9) accounts for these two effects and, hence, it is bounded in the range [1, L/l]. For high resolutions L/l (say L/l >4) the models in equations (B.9) and (B.15) should produce similar results; see Figures B.7 and B.8.

Similar to Figure B.9, Figure B.11 compares theoretically calculated exceedance probabilities of rainfall maxima to observed relative frequencies. Here $\gamma_{l,max}$ is calculated from equation (B.15) and the parametric expressions in Figure B.10. One sees that for spatial scales $l \geq 24$km the modified log-normal model for $\gamma_{l,max}$ performs slightly worse relative to the modified beta model in Section B.1 (see Figure B.9) and the maxima approach with a beta distribution in Section 3.3.2; see Figure 3.11. This reduced performance of the model is due to the two sources of bias discussed above.

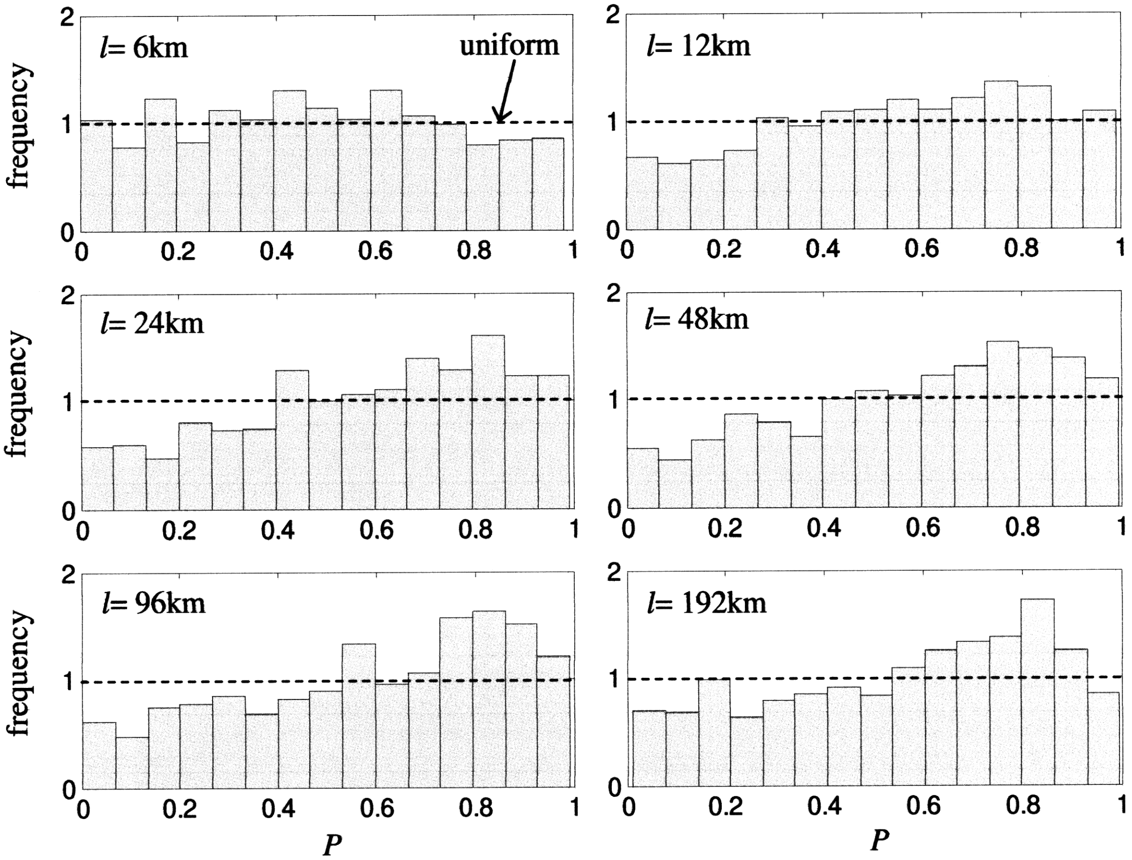

Figure B.11: Histogram of the non-exceedance probability P in equation (3.10) for different spatial scales l. $\gamma_{l,max}$ is calculated from equation (B.15) and the parametric expressions in Figure B.10. Each histogram is based on a sample of size 789.

B.3 Results from Different Approaches

Similar to Figure 3.12, Figure B.12 shows how the distribution of the total amplification factor $\beta_{l,max} = I_{l,max}/I_{L,MSR}$ depends on l, V_{max}, and $y' = |y/R_{max}|$. Results are shown for the three approaches developed in Sections 3.3.2, B.1 and B.2 to evaluate the distribution of the amplification factor $\gamma_{l,max}$. One sees that the maxima approach using a beta distribution (MB, dashed dotted lines), the marginal approach using a modified beta distribution (MMB, solid lines) and the marginal approach using a modified lognormal distribution (MML, dashed lines) produce similar results. Small differences can be noted, but this is due to the fact that the approaches are different and not derived one from another. However, these differences are small and negligible for practical applications; see Figure B.13 below.

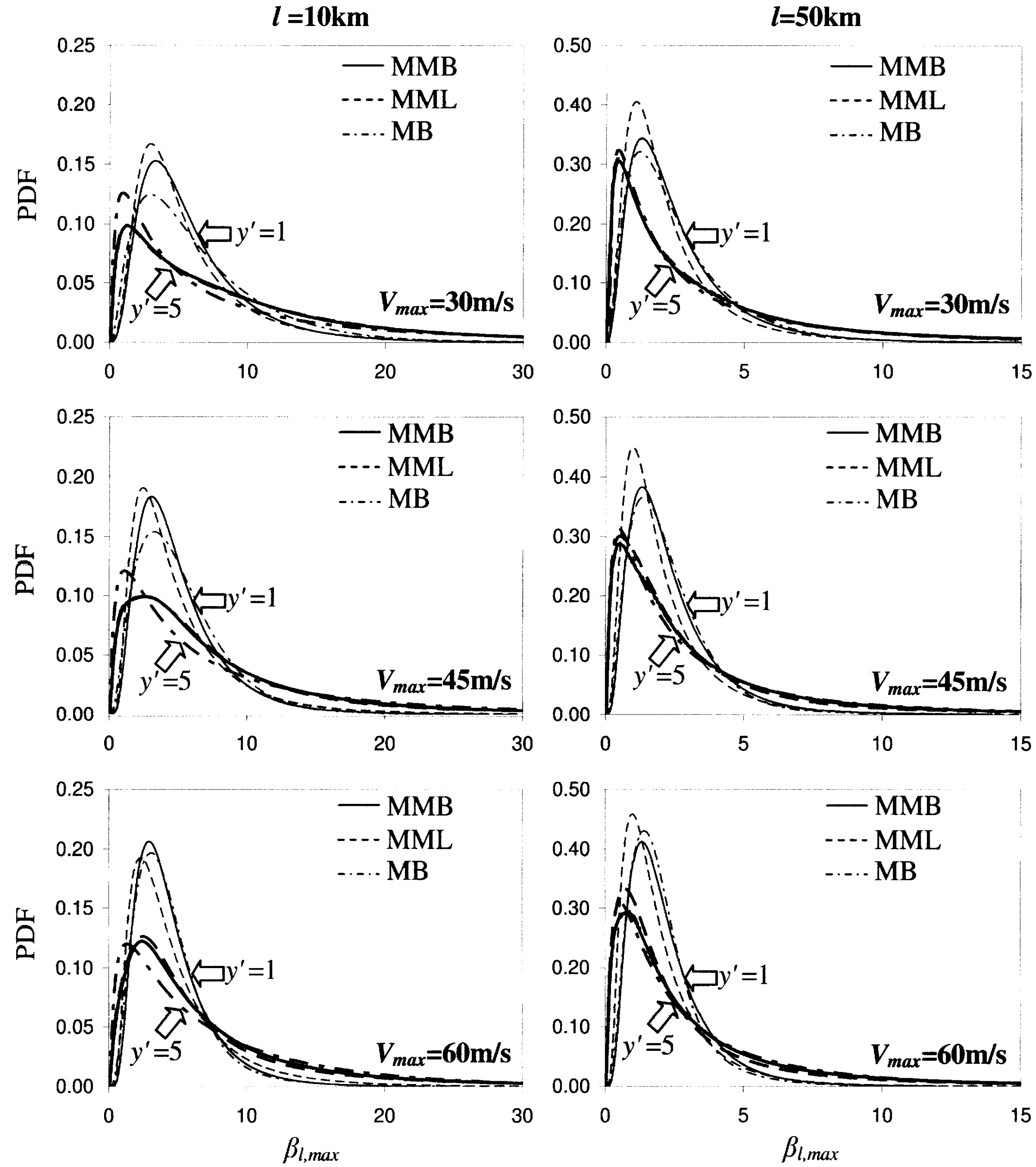

Figure B.12: Comparison of the theoretical probability density functions (PDFs) of the total amplification factor $\beta_{l,max} = I_{l,max}/I_{L,MSR}$ using the maxima approach with a beta distribution [MB (Section 3.3.2), dashed dotted lines], the marginal approach with a modified beta distribution [MMB (Section B.1), solid lines] and the marginal approach with a modified lognormal distribution [MML (Section B.2), dashed lines]. Results are shown for two different length scales l=10, 50km, different storm intensities V_{max}= 30, 45 and 60m/s and different normalized distances $y' = |y/R_{max}|$ from the center of the storm: y'=1 (thin lines) and y' =5 (thick lines).

Figure B.13 shows calculated IDF curves for New Orleans as plots of rainfall intensity i against return period T for different durations D. Results are shown for the three different approaches to evaluate the distribution of the amplification factor $\gamma_{l,max}$. All other model components (i.e. recurrence model and distribution of β_L) are the same as those used in Section 3.5. One sees that the IDF curves produced by the three approaches are similar.

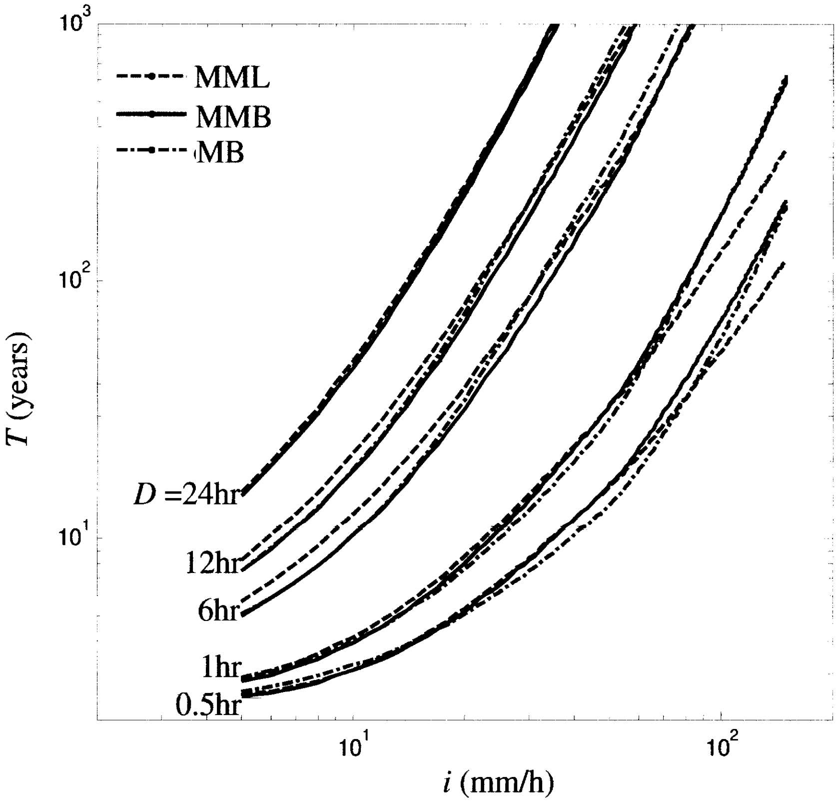

Figure B.13: Theoretical IDF curves for the region New Orleans obtained from equation (3.11) for $\lambda = 0.57$ events/yr using the maxima approach with a beta distribution [MB (Section 3.3.2), dashed dotted lines], the marginal approach with a modified beta distribution [MMB (Section B.1), solid lines] and the marginal approach with a modified lognormal distribution [MML (Section B.2), dashed lines]. Results are shown for averaging durations D = 0.5, 1, 6, 12 and 24 hours.